



저작자표시-비영리-변경금지 2.0 대한민국

이용자는 아래의 조건을 따르는 경우에 한하여 자유롭게

- 이 저작물을 복제, 배포, 전송, 전시, 공연 및 방송할 수 있습니다.

다음과 같은 조건을 따라야 합니다:



저작자표시. 귀하는 원저작자를 표시하여야 합니다.



비영리. 귀하는 이 저작물을 영리 목적으로 이용할 수 없습니다.



변경금지. 귀하는 이 저작물을 개작, 변형 또는 가공할 수 없습니다.

- 귀하는, 이 저작물의 재이용이나 배포의 경우, 이 저작물에 적용된 이용허락조건을 명확하게 나타내어야 합니다.
- 저작권자로부터 별도의 허가를 받으면 이러한 조건들은 적용되지 않습니다.

저작권법에 따른 이용자의 권리는 위의 내용에 의하여 영향을 받지 않습니다.

이것은 [이용허락규약\(Legal Code\)](#)을 이해하기 쉽게 요약한 것입니다.

[Disclaimer](#)

Ph.D. DISSERTATION

**The Long-term Stability of SiN_x Thin Film
Encapsulation Layers and Their Effects on the
Optical Property of Organic Light Emitting
Diode**

by

Min Ho Oh

February 2017

**Department of Materials Science and Engineering
College of Engineering
Seoul National University**

The Long-term Stability of SiN_x Thin Film Encapsulation Layers and Their Effects on the Optical Property of Organic Light Emitting Diode

Advisor : Prof. Hyeong Joon Kim

By

Min Ho Oh

**A thesis submitted to the Graduate Faculty of Seoul National University in partial fulfillment of the requirements for the Degree of Doctor of Philosophy
Department of Materials Science and Engineering**

February 2017

Approved by

Chairman of Advisory Committee : Cheol Seong Hwang

Vice-chairman of Advisory Committee : Hyeong Joon Kim

Advisory Committee : Seong Hyeon Hong

Advisory Committee : Sung Hwan Moon

Advisory Committee : Jae Yeong Heo

Abstract

The Long-term Stability of SiN_x Thin Film Encapsulation Layers and Their Effects on the Optical Property on Organic Light Emitting Diode

Min Ho Oh

Department of Materials Science and Engineering

College of Engineering

Seoul National University

The most widely used barrier for thin film encapsulation for OLEDs is the silicon nitride (SiN_x) deposited at low temperature of 85 °C by plasma enhanced chemical vapor deposition (PECVD).

In first study, we investigated the oxidation of SiN_x barrier films in the 85 °C/85% RH condition and the effect of the optical property of barrier on the reflectance, absorption, and transmittance of multilayer.

The SiN_x films for the oxidation test were prepared with changing the NH₃ and the H₂ gas ratio during deposition process. For the as-deposited thin films, the refractive index with increasing NH₃/total gas flow rate decreased from 1.93 to 1.81 and the film density reduced from 1.996 to 1.895. On the other hand, with increasing H₂ gas ratio, the refractive index increased from 1.80 to 1.90 and the film

density increased from 1.852 to 1.922.

We estimated the changes in physical properties and chemical bonding structures of the SiN_x films with the storing time in the condition of 85°C and 85% RH.

Both the stress and the refractive index of all samples decreased with a duration time in the $85^\circ\text{C}/85\%\text{RH}$ chamber. Those values changed largely with a larger NH_3 or a less H_2 gas flow rate during the deposition process. The initial stress with increasing NH_3 gas flow rate increased slightly from -153MPa to -163MPa, while the stress with increasing H_2 gas flow rate increased from -102MPa to -213MPa. The stresses with NH_3 gas flow rate decreased with oxidation test and the variation increased with a larger NH_3 gas. The other hand, the stresses of films with H_2 gas flow rate also decreased with oxidation time. But the variation was decreased with a higher H_2 gas flow rate. The stresses of $R_{\text{H}_2}=0$ and 0.48 were changed from -102MPa and -123MPa to nearly +100MPa, respectively, indicating a change from a compressive stress to a tensile. With $R_{\text{NH}_3}=0.073$ and 0.122, the refractive index decreased to 1.44 after 240hr, which is similar to the value of SiO_x thin film. The [N-H] peak intensities of as-deposited films were enhanced with increasing NH_3 gas flow rate, while the intensities after oxidation were more decreased in the films with a larger [N-H] peak. The [Si-H] peak position of as-deposited films with a larger NH_3 gas ratio shifted to a longer wavenumber, indicating N-rich SiN_x film. The [Si-H] peak intensities increased with increasing H_2 gas ratio, while [N-H] peaks decreased. FTIR spectra indicated that the [Si-N] or [N-H] bonds react with H_2O to form a thermodynamically more stable [Si-O] and/or [Si-OH] bond. The higher binding energy component of N1s spectrum (XPS) of as-deposited films with a higher NH_3 gas ratio corresponds to more [N-H] bonds. The [Si-H] and [N-H] bondings are crucial to the oxidation process. But the oxidation did not depend on

[Si-H] because [Si-H] bonding ratio was similar or slightly decreased with increasing NH₃ gas ratio. By comparing [Si-H] bonding (FT-IR) and N1s spectrum (XPS) of the films before and after the oxidation represented that the [N-H] groups were a main reactive sites, not the [Si-H].

The surface roughness by AFM increased from 0.88 to 1.20. The SiN_x films with increasing NH₃ flow rate were well oxidized. Cross-section transmission electron microscopy showed that the oxidation reaction occurred layer-by layer from the film surface and the defect and/or void was the center of oxidation.

The WVTR of 0.5um-thick film with R_{NH3}=0.073 was 5*10⁻⁵g/m²-day, resulting in the diffusion coefficient of 9.645*10⁻¹⁵cm²/s. After 240hrs in the 85°C/85%RH chamber, the oxidation thickness measured AES data was about 84.8nm and the one calculated from the Deal-Grove model was 76.2nm, being predicted 110nm after 500hrs.

Secondly, the effect of thin film encapsulation structure on the device optical properties was studied. The transmittance of multilayered-thin film is affected by the interface reflectance and absorption. In this study, the effect of reflection and absorption was examined separately. The transmittance according to the refractive index and extinction coefficient of barriers showed that the light intensity was decreased when the extinction coefficient was 10⁻³ or more. The reflection variation according to the first barrier thickness represented a larger variation and a short period when the thickness was less than 1um. The buffer layer formed between barriers had little effect on the reflectance at a thickness of 2um or more.

The effect of thin film encapsulation layer on the optical properties was investigated by inserting the light controlling layer between cathode and the first barrier, consisting of a high-/low- refraction layer. This layer showed the maximum

reflectance near the total thickness of about 200nm. The range of high-/low-refraction layer thickness which the reflectance became maximum was 70~100nm/70~120nm for blue, 70~120nm/70~150nm for green, and 70~150nm/50~150nm for red. The reflectance represented maximum value when the total thickness of light controlling layer was about 190nm and the high-/low-refraction layer thickness was between 70~100nm and 120~90nm, respectively. We demonstrated that the maximum efficiency was obtained when the high and low refraction layer thickness were 70nm and 120nm, respectively.

Finally, the optical property of the top barrier layer was investigated when the uppermost barrier was oxidized. If the buffer thickness was greater than 2 μ m, the effect of the top barrier oxidation thickness on the optical properties was very small. However, when the buffer thickness was 1 μ m and the barrier was 100nm, only about 30nm oxidation of the top barrier thickness induced the reflectance.

In order to develop a flexible display, the thickness of thin film barrier is becoming thinner. Most research is focused on the barrier performance. However if the barrier is oxidized, the film composition, the bonding structure, and the film stress may be changed so that the optical characteristics and the mechanical stresses of device may be affected. This means that the barrier studies are needed in terms of performance and chemical and mechanical stability.

Keywords : Plasma Enhanced Chemical Vapor Deposition (PECVD), Silicon Nitride, Barrier, Oxidation, Optical Property

Student ID : 2011-30189

Table of Contents

Abstract	i
Table of contents	v
List of Tables	vii
List of Figures	viii
1. Introduction	1
1.1 Overview	1
2. Literature Review	6
2.1 Encapsulation technology	6
2.2 Water vapor transmission rate	10
2.3 Thin film encapsulation	17
2.4 The property of silicon nitride thin films	31
2.5 Working principles of OLEDs	41
3. Experiments and Analyses	50
3.1 Film preparation	50
3.2 Oxidation of SiN _x barriers	50
3.3 Simulation of SiN _x barriers	50
3.4 Film characterization	51
4. Results and Discussions	53
4.1 Oxidation of SiN _x barriers	53

4.1.1 Introduction.....	53
4.1.2 The property of as-deposited SiN _x film	55
4.1.3 The acceleration test of SiN _x thin film barriers	62
4.1.4. Summary	95
4.2 The effect of TFE (thin film encapsulation) structure on the optical property of OLEDs	97
4.2.1 Introduction	97
4.2.2 Microcavity and Fabry-Perot cavity	98
4.2.3 The effect of TFE on the optical property of OLEDs	111
4.2.4. Summary	131
5. Conclusions	133
Bibliography	134
한글 초록	143

List of Tables

Table. 2.1. Previous experiments of the barrier performance with as-deposited films.

Table. 2.2. The key parameters and requirements for thin film encapsulation.

Table. 4.1. The effect of NH_3 gas flow rate on the physical properties of as deposited SiN_x barrier films.

Table. 4.2. The effect of H_2 gas flow rate on the physical properties of as-deposited SiN_x barrier films.

Table. 4.3. Film stress and refractive index of SiN_x films with NH_3 and H_2 /total gas flow rate after acceleration test for 240hr in the condition of $85^\circ\text{C}/85\%\text{RH}$.

Table. 4.4. Infrared vibrations observed in the sample before and after the reliability test at the condition of 85°C and $85\% \text{RH}$.

Table. 4.5. The morphology and roughness changes measured by AFM before and after duration in the humidity chamber.

Table. 4.6. Literature survey on the oxidation of SiN_x films.

Table. 4.7. Effects of refractive index of thin films with absorption on the reflectance, absorption, and transmittance.

List of Figures

- Fig. 1.1. The trend of display application.
- Fig. 1.2. The schematic diagram (a) and the classification (b) of OLED.
- Fig. 1.3. The degradation mechanism of OLED.
- Fig. 2.1. Different types of defects damaged by water vapor and oxygen, dark spot and shrinkage, respectively.
- Fig. 2.2. The mechanism of OLED degradation due to water vapor and oxygen.
- Fig. 2.3. WVTR requirements for various display devices.
- Fig. 2.4. Comparison of water vapor transmission rate.
- Fig. 2.5. The measurement methods of WVTR ; (a) MOCON system, (b) HTO method, (c) Ca-test.
- Fig. 2.6. The trends in development of encapsulation technologies.
- Fig. 2.7. The schematic diagram of inorganic/organic thin film encapsulation, leading to an increase of penetration pathway of moistures and outgases.
- Fig. 2.8. Cross-sectional structure model of the condensation of adsorbed $\text{Si}(\text{NH}_2)_3$ toward an [Si-N] network with the evolution of NH_3 gas.
- Fig. 2.9. Schematics of the behaviors of hydrogen in tensile (left) and compressive (right) films.
- Fig. 2.10. Schematics of multi-layer OLED structure and optical ray diagram of light propagation via various modes.
- Fig. 4.1. Effects of NH_3 gas flow rate on the refractive index, WVTR, film stress and density of as-deposited SiN_x barriers.
- Fig. 4.2. Effects of H_2 gas flow rate on the refractive index, WVTR, film stress and density of as-deposited SiN_x barriers.

- Fig. 4.4. The changes of film stress and refractive index with a storing time in the 85 °C and 85% RH chamber. For fig. (a) & (b), NH₃/total gas flow rate : ■ 0.034, ● 0.057, ▲ 0.073, ▼ 0.122 ; For (c) & (d), H₂/total gas flow rate : ■ 0.48, ● 0.58, ▲ 0.65, ▼ 0.69.
- Fig. 4.4. The FT-IR spectra of as-deposited SiN_x films with NH₃ and H₂ gas flow rate. NH₃/total gas flow rate — 0.034, — 0.057, — 0.073, — 0.122 ; H₂/total gas flow rate — 0.48, — 0.58, — 0.65, — 0.69.
- Fig. 4.5. The FT-IR spectra of SiN_x films after the acceleration tests at the condition of 85 °C and 85% RH chamber for 240hrs. . NH₃/total gas flow rate — 0.034, — 0.057, — 0.073, — 0.122 ; H₂/total gas flow rate — 0.48, — 0.58, — 0.65, — 0.69.
- Fig. 4.6. Binding energy of Si2p by XPS before and after oxidizing in the humidity chamber for 240hrs. NH₃/total gas flow rate = 0.034.
- Fig. 4.7. Binding energy of Si2p by XPS after oxidizing in the humidity chamber for 240hrs.
- Fig. 4.8. Comparison of [Si-H] and [N-H] bonding peak position (FT-IR) of SiN_x films with NH₃/total gas flow rate before and after oxidation.
- Fig. 4.9. Comparison of [Si-H] and [N-H] bonding peak position (FT-IR) of SiN_x films with H₂/total gas flow rate before and after oxidation.
- Fig. 4.10. N1s spectra (XPS) of as-deposited SiN_x films.
- Fig. 4.11. The changes in morphology and surface roughness as a function of the amounts of NH₃ and H₂ addition to the reactant gases, before and after storing in the humidity chamber.
- Fig. 4.12. The cross-section images of SiN_x films by TEM; (a) & (b) as-deposited film and (c) & (d) after storing in the condition of 85 °C and 85% RH

for 240hrs. (a) & (c) are top images of the films and (b) & (d) bottom images of the films.

- Fig. 4.13. Relationship between the [Si-O-Si] and [Si-H] mode absorption coefficient with time.
- Fig. 4.14. The influence of thin film stress on the curvature of the deposition substrate.
- Fig. 4.15. The composition profiles of SiN_x films by Auger Electron Spectroscopy as a function of NH₃ gas flow rates. The etch rate was 5.3nm/min.
- Fig. 4.16. OLEDs with different device configuration.
- Fig. 4.17. Reflection and transmission of light ray in optical thin film.
- Fig. 4.18. The effect of the TFE structure on the optical property of TOLEDs.
- Fig. 4.19. The optical transmittance and luminance with varying the structure of thin film encapsulation.
- Fig. 4.20. Multi-layered TFE structure with barrier and buffer layers for the optical study.
- Fig. 4.21. The relationship between refractive index, extinction coefficient and transmission of silicon nitride thin films deposited at 85 °C by PECVD.
- Fig. 4.22. The relationship between optical constants : refractive index vs. extinction coefficient vs. transmittance.
- Fig. 4.23. Effects of barrier thickness on the reflectance. The extinction coefficient of each layer was assumed to be zero.
- Fig. 4.24. Effect of buffer layer thickness on the reflectance. The refractive index and the barrier thickness were 2.0 and 1000nm, respectively.
- Fig. 4.25. Effects of light-controlling layer thickness on the reflectance. The refractive index of each layer was 2.0 and 1.45, respectively.

- Fig. 4.26. Effects of light-controlling layer thickness on the reflectance.
- Fig. 4.27. Effects of thickness with high and low refractive index on the relative efficiency. The reference was a glass-encapsulated OLED.
- Fig.4.28. (a) Relationships between refractive index, extinction coefficient, and transmittance (b) effect of refractive index of films with absorption on the efficiency.
- Fig. 4. 29. Effects of refractive index of thin films with absorption on the reflectance. (a) Blue, (b) Green, (c) Red.
- Fig. 4.30. Effects of the oxidized barrier thickness on the reflectance. (a) buffer = 4 μ m, barrier = 1 μ m ; (b) buffer = 1 μ m, barrier = 1 μ m ; (c) buffer =1 μ m, barrier = 10nm.

1. Introduction

1.1. Overview

In recent years, OLED (Organic Light Emitting Diodes) are rapidly upcoming devices for display and lighting applications. OLED have been emerged promising display devices due to expectations for vivid color, low cost, low power consumption. It has expanded into the areas of TV, transparent display, as well as mobile display (Fig. 1.1). Recently, products employing bended forms, which are made of polymer substrate and thin film encapsulation, have started to appear in the mobile market. OLEDs consisted of polymer film substrates and thin film encapsulation instead of glass has received attention as materials that can realize thin, flexible, unbreakable, and rollable display.

OLED is consisted of anode, cathode and organic emitting layer between them, in which the holes injected from anode and the electrons injected from cathode combine, and then emitting a light. The organic layers in OLED consisted of thin films, such as hole injection layer, hole transport layer, emitting layer, electron transport layer, electron injection layer. The OLEDs can be classified into bottom and top emission. It is called 'bottom emission' when the light emits through the TFE glass and 'top emission' when the light emits through the cover glass (Fig. 1.2).

However, the potential industrial application of OLEDs to large area panel full-color displays and the flexible organic electronic displays has been limited by a short operation lifetime due to the degradation and short lifetime. Major degradation mechanisms have been suggested due to metal delamination, recrystallization of organic materials, reactions in metal and organic interfaces, metal migration, molecule-specific degradation, oxidation by water and oxygen, and so on (Fig. 1.3)

[1-5].

The major degradation mechanism of OLEDs is,

- (i) metal delamination
- (ii) recrystallization of organic materials
- (iii) reactions in metal and organic interfaces
- (iv) metal migration
- (v) molecule-specific degradation
- (vi) oxidation by water and oxygen - local oxidation of cathode

Especially, the organic material and cathode metal constituting of OLED can be damaged when exposed to water and oxygen. The damage by water and oxygen is critical to OLEDs, because the user can recognize the defects and the abnormal phenomena.

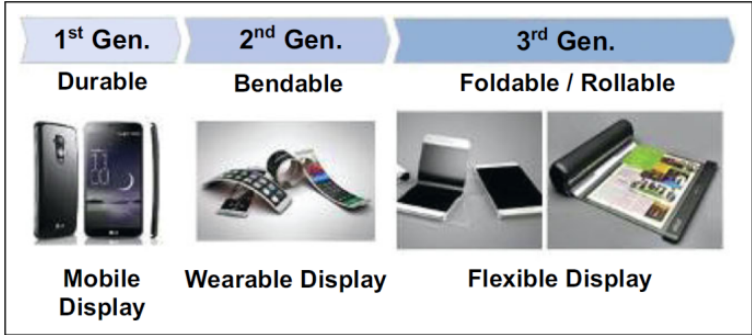


Fig. 1.1 The trend of display application [’15 SID].

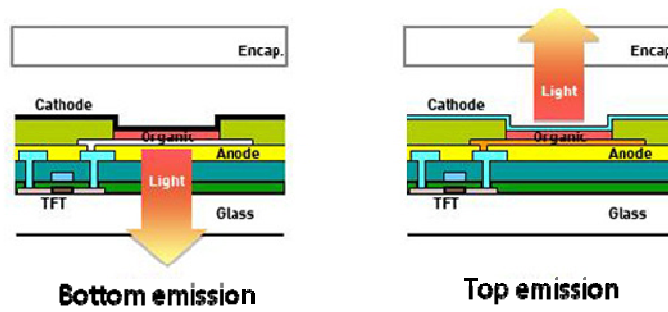
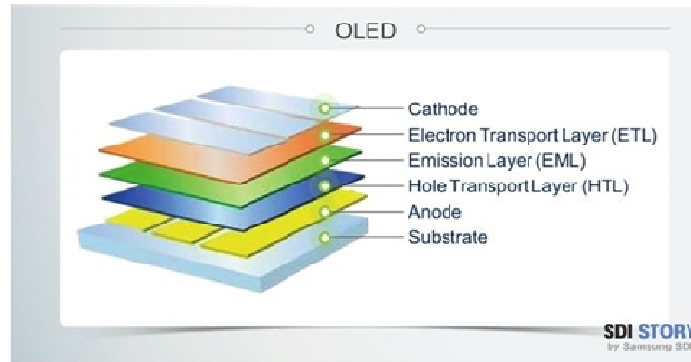


Fig. 1.2. The schematic diagram (a) and the classification (b) of OLED.

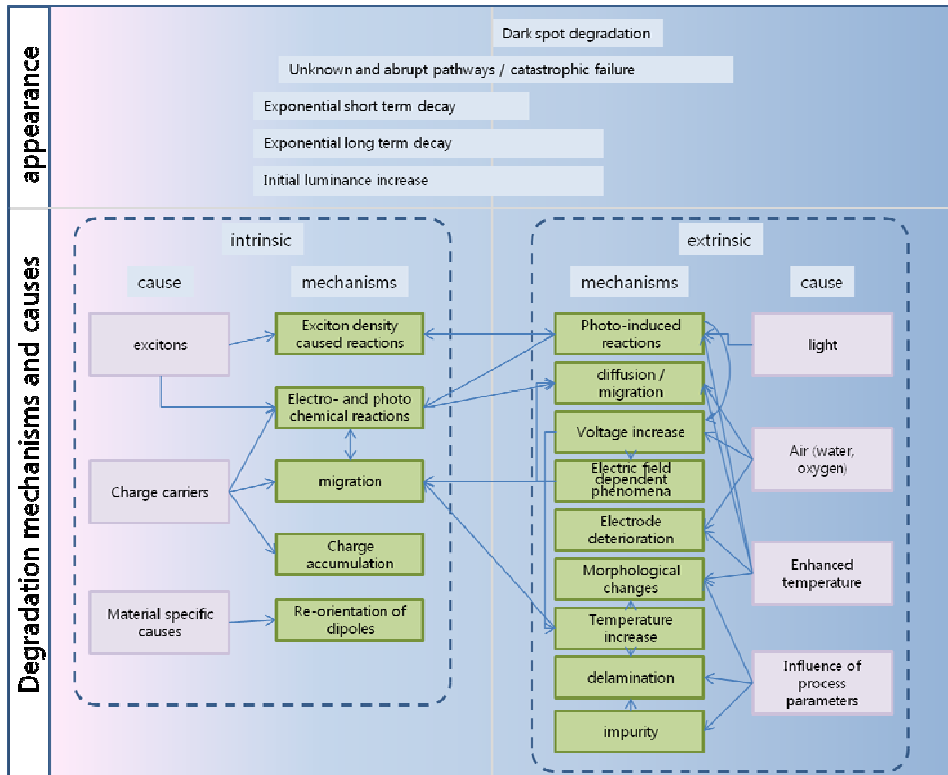


Fig. 1.3. The degradation mechanisms of OLED [6].

2. Literature Review

2.1 Encapsulation technology

There are two types of failure mode, which are dark spot and shrinkage, respectively. The dark spot is a non-emitting area in the active area due to the damages, while it is called 'shrinkage' when the size of active area is reduced from the edge due to the lateral permeation (Fig. 2.1)

The degradation of OLEDs has been reported in literature by various researchers. The degradation of small molecule organic materials, migration of ionic species, electrochemical reactions at the electrode/organic interface, dark spot growth, and the effect of water vapor and oxygen have been reported. In general, dark particles deposited during the fabrication led to the formation of pinholes in the cathode. Water vapor passes through the pinholes and diffuses into the cathode/organic interface, producing hydrogen gas by reacting with the cathode. Under the pressure of the gas, the bubbles formed. Through the bubbles, water can be transport much faster than by diffusion. Finally, the bubbles burst and give rise to additional entry ports for water vapor (Fig. 2.2) [1].

The most commonly used encapsulation method employs UV-cured epoxy seal as a perimeter seal together with a strong desiccant inside the device. The encapsulation method is achieved by glass and metal lid. The epoxy adhesive is introduced around the edge of the device using a syringe. A clean metal or glass lids covers at the top of the devices. An inert nitrogen gas is filled in the sealed volume. All processes have to be proceeded in the environment, in which the content of water and oxygen is controlled below 10ppm. In addition, desiccant materials such

as Ca and barium were used to absorb water vapor diffusing from the epoxy adhesive and removing any existing water.

However, this method is inadequate for the top emitting OLED because the emitted light is cutoff by opaque getter which resides on the cover glass. Moreover, a narrow perimeter of the desiccant is insufficient to eliminate the moisture completely from a sealed OLED device.

The second method is to attach two glasses with inorganic sealing materials. There is a requirement for new encapsulation technology for a top emitting device, which is an inorganic frit seal, instead of epoxy sealant, as a sealing material. The inorganic frit material is coated on the perimeter of cover glass. The inorganic frit material is melted by laser irradiation after sealed with the backplane. The water vapor and oxygen cannot penetrate through the inorganic frit seal.

In the first method, moisture and oxygen permeate through the sealant and the getter materials in enclosure adsorb them so that OLED elements are not affected. The second method, in comparison, can obtain higher durability because water vapor and oxygen cannot penetrate into the inorganic sealing materials. Glass can be used to form curved devices with large curvature radius, but has limits in the use in bendable/flexible devices.

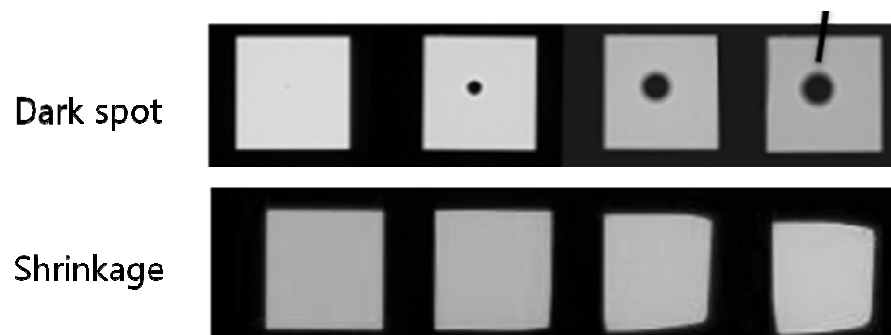


Fig. 2.1 Different types of defects damaged by water vapor and oxygen, dark spot and shrinkage, respectively

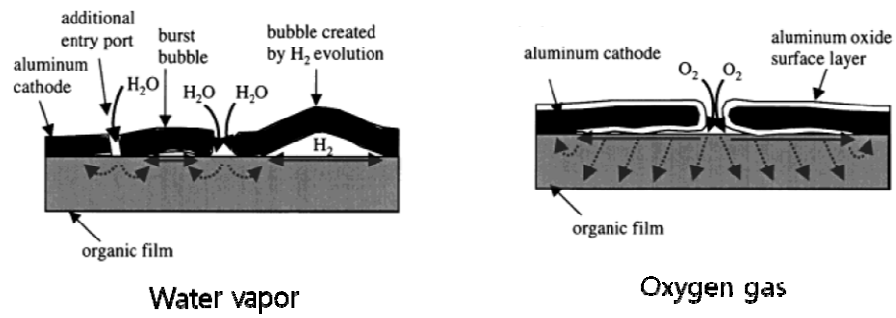


Fig. 2.2 The mechanisms of OLED degradation due to water vapor and oxygen [1].

2.2 Water Vapor Transmission Rate

The purpose of permeation barrier is to keep the organic electronics from the exposure to the water vapor and oxygen. Therefore, it is necessary to control the permeation rate through the barrier film. The permeation rates of oxygen and water vapor across the barrier layers are characterized in terms of the oxygen transmission rate (OTR) and the water vapor transmission rate (WVTR).

There is a wide range of permeation barrier requirements for different devices and applications (Fig. 2.3). For the normal food packaging technologies, the encapsulation barrier requirements are not as stringent as the electronics devices and a single polymer film is sufficient to provide the required efficient packaging. Generally, devices such as OLEDs that use chemically reactive electrodes have the highest sensitivity to moisture, and degradation is observed at the organic layer / electrode interface. WVTR is defined as the amount of water molecules diffusing through a unit area of the barrier film per unit time under conditions of the test and expressed as $\text{g/m}^2\text{-day}$. OTR is defined as the volume of oxygen diffusing through a unit area of the barrier film per unit time under conditions of the test and expressed as $\text{cm}^3/\text{m}^2\text{-day}$. The thin film encapsulation refers to the barrier layers that can protect the OLED from moisture and oxygen. Therefore, the devices require protective layers with extremely low water vapor and oxygen permeability. Thin film encapsulation requires water vapor transmission rate (WVTR) and oxygen transmission rate (OTR) lower than $1 \times 10^{-6} \text{ g/m}^2\text{-day}$ and $1 \times 10^{-5} \text{ cm}^3(\text{STP})/\text{m}^2\text{-day}$, respectively [7].

The level of transmission rate corresponds to the amounts passing through the soccer field over a month (Fig. 2.4).

Typically commercial systems are useful for the measurement of thin films.

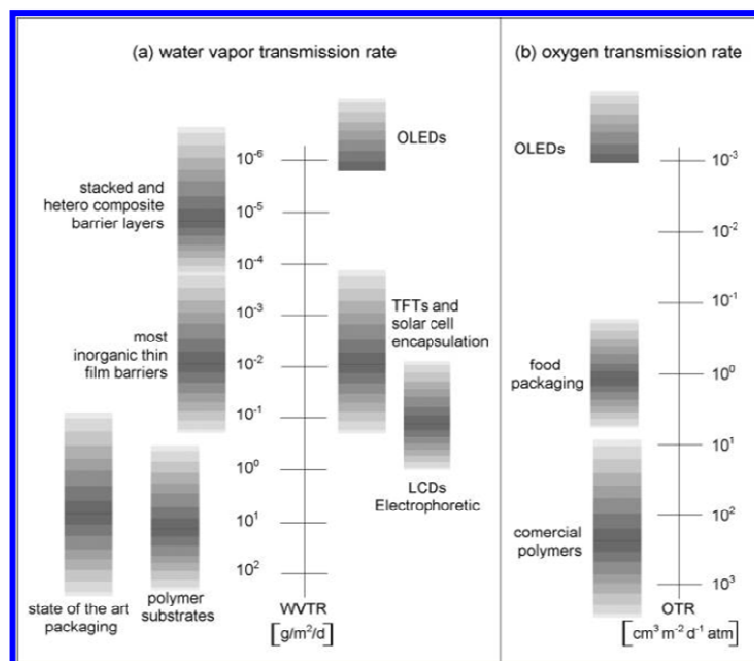
Permeation of oxygen and water vapor was measured with standard devices from MOCON (Fig. 2.5 (a)) [MOCON Inc.] The permeated species are detected by a coulometric sensor. Typically commercial systems are useful for the measurement of thin films. Permeation of oxygen and water vapor was measured with standard devices from MOCON (Fig. 2.5 (a)) [MOCON Inc.] The permeated species are detected by a coulometric sensor. However, the commercially available systems do not meet the sensitivity requirements for the low permeation rates needed for OLEDs, which are limited to a sensitivity in the order of 10^{-5} g/m²-day for water vapor. The effective transmission rates for H₂O through barrier films using the Ca test are as low as the order of 10^{-7} g/m²-day. The Ca test has the advantage of discriminating between bulk permeation and defect-based permeation, which can be observed as spots on the Ca film. However, it does not discriminate between oxygen and water permeation.

HTO (hydrogen-tritium-oxygen) tracer method (Fig. 2.5 (b)) [8]. HTO is the source of tritium that can diffuse through the films either as molecular HTO or possibly as tritium atoms. However, this method needed further study because of the fact that the absorption of HTO can be affected by the water vapor from the outside atmosphere. Also, the test was dangerous, because of the radioactivity of the radioactive tracer and unavailability in some experimental situations.

To measure reliable water permeation, the other method is known as the tritium transmission rate measurement, using the radioactive

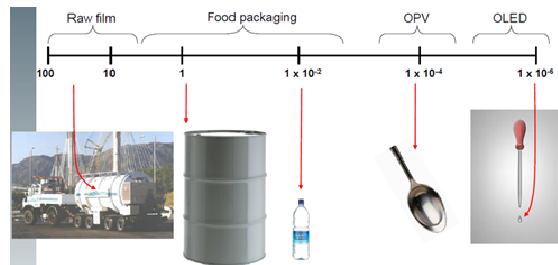
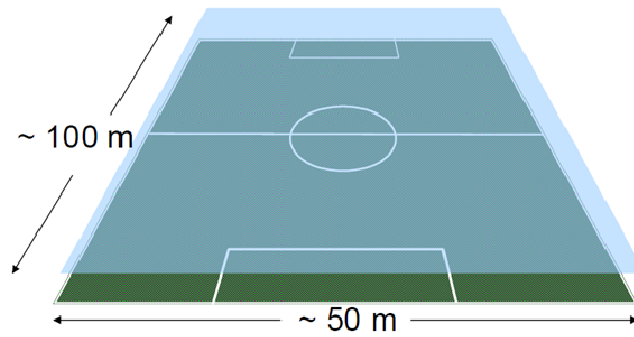
Another approach is known as the Ca test (Fig. 2.5 (c)). The Ca corrosion test is a widely known method for measuring ultra-low permeation rate barrier films. Calcium is a conducting and opaque metal which becomes non-conducting and transparent after oxidation. It rapidly oxidizes in air due to the highly negative

Gibbs free energy of formation of Ca oxides making it very sensitive for detecting the presence of oxygen and water vapor. Since the oxide is a dielectric and transparent, both of them are possible to monitor the consumption of Ca by either measuring the change in electrical conductance or in optical transparency. Hence, the measurement of Ca conductance or transparency changes versus time provides an indirect method to determine the oxidation and corrosion rates of Ca [9].



Chem. Rev., 115, 8448–8503, 2015

Fig. 2.3 WVTR requirements for various display devices.



The amount of passing through the soccer field over a month.

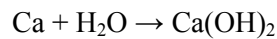
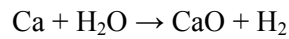
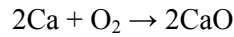
Source : MOCON Inc.

Fig. 2.4 Comparison of water vapor transmission rate.

The permeation rate through the film can be calculated by the following equation.

$$P = -n \frac{M(\text{H}_2\text{O})}{M(\text{Ca})} \delta \rho \frac{l}{b} \frac{d(1/R)}{dt}$$

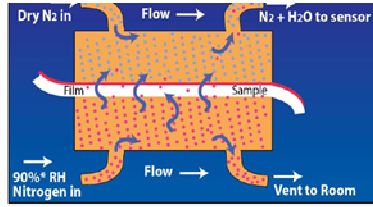
Where δ is the density of Ca, l and b are length and width, respectively, of Ca layer, and ρ is the resistivity, indicating that the permeate rate is proportion to differential of the conductance curve $1/R$ versus measurement time t . Ca react with water following reaction.



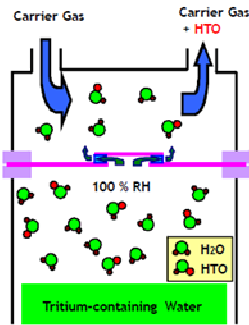
The effective WVTR can be determined by monitoring the time rate of change of the electrical conductance of Ca.

$$\text{WVTR} \left[\frac{\text{g}}{\text{m}^2/\text{day}} \right] = -n \delta_{\text{Ca}} \rho_{\text{Ca}} \frac{d(G)}{dt} \frac{l}{w} \frac{M(\text{H}_2\text{O})}{M(\text{Ca})} \frac{\text{Area}(\text{Ca})}{\text{Area}(\text{Window})}$$

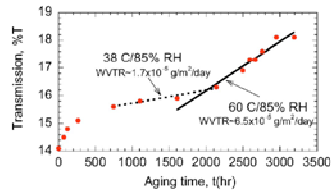
This method are highly sensitte, because the oxidation can be monitored by measuring the resistivity of Ca compounds as well as tracking the transparency.



(a) MOCON : $\sim 1 \times 10^{-4} \text{g/m}^2\text{-day}$



(b) HTO (Tritiated Water) : $1 \times 10^{-6} \text{g/m}^2\text{-day}$



(a)



(b)

Appl. Phys. Lett. 89 031915 2006

(3) Ca-test : $1 \times 10^{-7} \text{g/m}^2\text{-day}$

Fig. 2.5 The measurement methods of WVTR (a) MOCON system, (b) HTO method, (c) Ca-test.

2.3 Thin Film Encapsulation

Fig. 2.6 shows the trends in developments of encapsulation technologies. Two methods for rigid OLED are used to seal the substrate and the cover glass.

The most commonly used encapsulation method employs UV-cured epoxy seal as a perimeter seal together with a strong desiccant inside the device. The getter materials can adsorb water and oxygen. The getter is necessary because the epoxy seal is not a good moisture barrier. However, this method is inadequate for the top emitting OLED because the emitted light is cutoff by opaque getter which resides on the cover glass. Moreover, a narrow perimeter of the desiccant is insufficient to eliminate the moisture completely from a sealed OLED device.

The second method is to attach two glasses with inorganic sealing materials. There is a requirement for new encapsulation technology for a top emitting device, which is an inorganic frit seal, instead of epoxy sealant, as a sealing material. The inorganic frit material is coated on the perimeter of cover glass. The inorganic frit material is melted by laser irradiation after sealed with the backplane. The water vapor and oxygen cannot penetrate through the inorganic frit seal.

In the first method, moisture and oxygen permeate through the sealant and the getter materials in enclosure adsorb them so that OLED elements are not affected. The second method, in comparison, can obtain higher durability because water vapor and oxygen cannot penetrate into the inorganic sealing materials. Glass can be used to form curved devices with large curvature radius, but has limits in the use in bendable/flexible devices.

However, these typical encapsulation techniques with rigid materials have some problems in application in flexible devices. Moreover, flexible encapsulation

approaches such as ultra-thin film glass, barrier-coated flexible lids, and vacuum-deposited thin films are more effective. Accordingly, high performance thin film encapsulation technology should be developed to realize long-time driving OLED display.

Different methods are applied in manufacturing thin films. Chemical vapor deposition (CVD) as well as atomic layer deposition and molecular layer deposition (ALD/MLD) are most frequently used methods.

Actually, a lot of studies on the barrier performance have been reported (Table. 2.1). Many researchers have focused on the improvement of the barrier performance. Therefore, there are many reports for evaluating the WVTR and the OTR measured by the above-mentioned methods. As seen in this table, we can find that there are large differences between the WVTR values with tools for the same materials. This means that we have to refer to the transmission rate for estimating the barrier performance because these are dependent on the test methods.

Several chemical vapor deposition methods such as atmospheric pressure chemical vapor deposition (APCVD), plasma enhanced chemical vapor deposition (PECVD), and low pressure chemical vapor deposition (LPCVD) have been developed to deposit thin films (especially SiN_x films) as the encapsulation layer. APCVD has a lot of advantages such as good step coverage, uniformity, and relative low cost. However, this process works at high temperature. So, the PECVD was adopted to lower the deposition temperature. PECVD is a type of deposition technology, allowing industrial-scale deposition of good quality insulating films such as silicon nitride and silicon oxide with good adhesion. The most important advantages of PECVD are that it can be performed at low deposition temperatures, especially under 100°C . The deposition temperature of OLEDs is limited below

100°C.

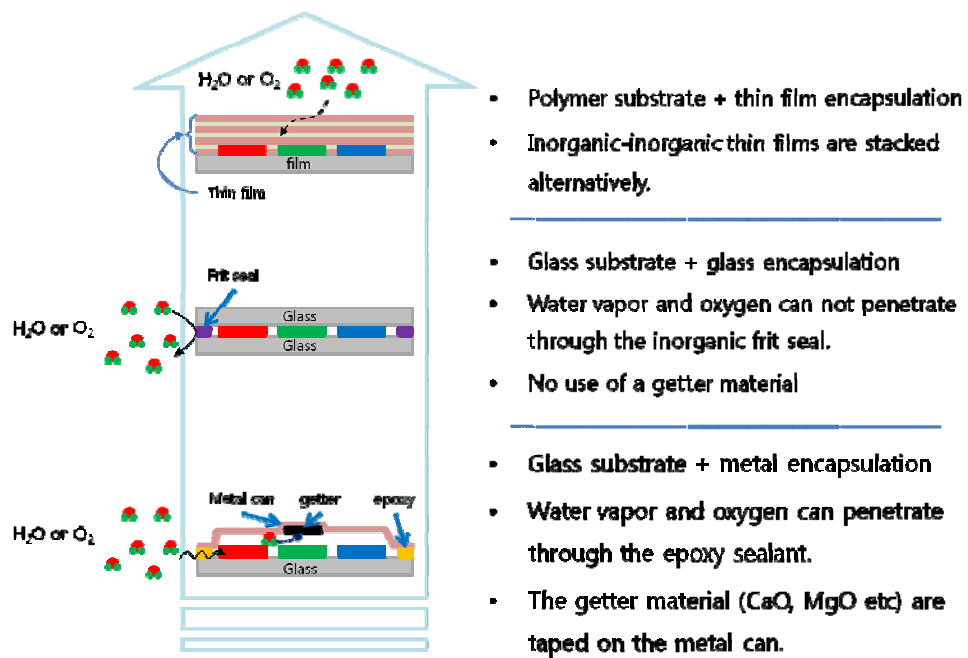
The performance of barrier layers can be measured by WVTR, wet etch rate, and defect density [10-14]. Most studies on thin film encapsulation focused on improving initial barrier performance and evaluating the reliability. Therefore, the relationship between stress, refractive index, and composition of the barrier properties were the main issues [15-18]. Research on thin film encapsulation has mainly progressed in two directions:

One is lowering the water vapor permeability by developing new materials, and the other is optimizing the thin film structure by stacking inorganic and organic layers alternatively to increase the diffusion path [19-23].

Thin film barriers are mostly inorganic materials such as; AlO_x , AlO_xN_y deposited by sputtering [24-26] AlO_x by atomic layer deposition (ALD) [27-32], and SiN_x or SiO_x by plasma enhanced chemical vapor deposition (PECVD) [33, 34].

ALD has the advantage of allowing the deposition of very dense films at low temperature ($< 100^\circ\text{C}$), and thus appears to be a promising technique suitable for preparing encapsulation layers on top of organic electronics devices. S.W. Seo et al. reported nano-laminated composite films comprised of alternating layers different materials by ALD at 80°C . The Al_2O_3 layer acted as a better moisture barrier than ZrO_2 at the same thickness. The time of 130hrs at 85°C and 85% RH corresponds to the average WVTR of about $1.1 \times 10^{-4} \text{ g/m}^2\text{day}$ at ambient condition. The time to complete oxidation of the Ca layer increased with increasing number of interfaces [35]. Nanolaminate films can also be grown by combining Al_2O_3 ALD and alucone MLD and excellent diffusion barrier properties can be achieved with nanolaminate films [36].

Another research showed that the alternating nanolayer structure suppresses the



- Polymer substrate + thin film encapsulation
- Inorganic-inorganic thin films are stacked alternatively.

- Glass substrate + glass encapsulation
- Water vapor and oxygen can not penetrate through the inorganic frit seal.
- No use of a getter material

- Glass substrate + metal encapsulation
- Water vapor and oxygen can penetrate through the epoxy sealant.
- The getter material (CaO, MgO etc) are taped on the metal can.

Fig. 2.6 The trends in development of encapsulation technologies.

year	layer	materials	process	WVTR/OTR	method	source
2002	inorganic	Al ₂ O ₃ /ZrO ₂	ALD	1.1×10 ⁻⁴	electrical Ca-test	<i>Org. Electron.</i> 13 2436
2004	inorganic	SiO ₂	PECVD	0.31	MOCON	<i>Thin Solids Films</i> 468 105
2004	inorganic/organic	SiN _x /Parylene	PECVD	0.15	MOCON	<i>J. Vac. Sci. & Technol. A</i> 22
2005	inorganic	SiN _x /AlO _x	PECVD/ALD	0.058	MOCON	<i>Elec. Solid-State Letters</i> 8 H21
2005	inorganic	parylene/SiN _x /AlO _x	PECVD/ALD	6.2×10 ⁻²	MOCON	<i>Appl. Phys. Lett.</i> 90 013502
2005	inorganic/organic	SiN _x /SiC _x H _y	PECVD	5.9×10 ⁻⁶	Ca-test	<i>J. Vac. Sci. & Tech. A</i> 23 971
2006	inorganic	AlO _x	ALD	1.7×10 ⁻⁵	optical Ca-test	<i>Appl. Phys. Lett.</i> 89 031915
2006	inorganic	AlO _x	ALD	1×10 ⁻³	HTO test	<i>Appl. Phys. Lett.</i> 88 051907
2006	inorganic	AlO _x	PEALD	5×10 ⁻³	optical Ca-test	<i>Appl. Phys. Lett.</i> 89 081915
2006	inorganic	SiO _x /SiN _x	PECVD	3.12×10 ⁻⁶	optical Ca-test	<i>J. Electro. Soc.</i> 153 F244
2006	inorganic/organic	parylene/SiO _x	evaporation	0.05	MOCON	<i>J. Jpn. Appl. Phys.</i> 45 L827
2007	inorganic	SiN _x	PECVD	5×10 ⁻³	MOCON	<i>Appl. Phys. Lett.</i> 90 013502
2009	inorganic	AlO _x /ZrO ₂	ALD	4.7×10 ⁻⁴	electrical Ca-test	<i>Adv. Mater.</i> 21 1845
2009	inorganic	AlO _x /SiN _x	ALD/PECVD	< 10 ⁻⁵	optical Ca-test	<i>J. Appl. Phys.</i> 106 023533
2010	Inorganic	SiN _x /AlO _x	PECVD/Sputtering	1×10 ⁻³	MOCON	<i>Thin Solid Films</i> 518 3075
2010	Inorganic	AlO _x /ZrO ₂	PEALD	3.2×10 ⁻⁴	electrical Ca-test	<i>Appl. Phys. Lett.</i> 96 243308
2012	Inorganic	AlO _x /SiN _x	PEALD/PECVD	2×10 ⁻⁶	optical Ca-test	<i>J. Vac. Sci. Technol. A</i> 30 01A131
2012	Inorganic	AlO _x :N	PEALD	< 10 ⁻⁵	optical Ca-test	<i>Org. Electron.</i> 13 2436
2012	Inorganic/organic	AlO _x /alucone	ALD/MLD	1×10 ⁻⁴	MOCON	<i>Appl. Phys. Lett.</i> 101 234103
2013	Inorganic	AlO _x	PALD	2.6×10 ⁻⁴	electrical Ca-test	<i>J. Appl. Phys.</i> 114 173511
2013	Inorganic	AlO _x	ALD	4×10 ⁻⁴	Ca-test	<i>J. Vac. Sci. Technol. A</i> 31 061507
2013	Inorganic/organic	AlO _x /PP	ALD/PECVD	3.1×10 ⁻⁴	Ca-test	<i>Appl. Phys. Lett.</i> 102 161908
2015	Inorganic/organic	AlO _x /TiO ₂ /Al alkoxide	ALD/MLD	1×10 ⁻³	Ca-test	<i>J. Vac. Sci. Technol. A</i> 33 01A119

Table. 2.1 Previous experiments of the barrier performance with as-deposited films.

formation of both microscopic voids and nanocrystals. They reported the ultra low permeation rate of 4.7×10^{-5} g/m²-day for water and 1.6×10^{-2} cm³/m²-day for oxygen (70°C/70% RH), using the 130nm thick nanolaminates prepared by repeated deposition of AlO_x/ZrO_x [37-39].

The combination of ALD deposited AlO_x with another inorganic film, PECVD deposited SiN_x, or polymeric organic film, parylene, resulted in better barrier properties. The intrinsic WVTR values of barriers consisted of the AlO_x (PEALD) and SiN_x (PECVD) was in the 10^{-6} g/m²-day range [40] and in the range of 5×10^{-5} g/m²-day, which was calculated by means of the Ca test. [41].

While the WVTR of SiN_x/SiO_x multilayer structure was in the range of 5.8×10^{-2} g/m²-day when measured by MOCON instrument [42].

The WVTR of films consisting of SiO_x (PECVD) and AlO_x (sputtering) was investigated [43]. The SiO_x/SiN_x stacks by PECVD as the barrier structure instead of the organic/inorganic multilayered structure on the PC substrate were investigated to prevent adhesion problems that may occur between the organic and inorganic interfaces. The achieved WVTR value for the optimum barrier structure reduces 3.12×10^{-6} g/m²-day and keeps below 3.54×10^{-5} g/m²-day after the cyclic bending (SiN_x + 6 SiO_x/SiN_x pairs) [44, 45].

The ALD deposited AlO_x thin film for the barrier and the parylene film for the buffer layer enhanced the lifetime although the barrier thickness is reduced [46].

PECVD at low temperature is the most favorable tool, considering its scale-up capability and processing time. D. S. Wu et al. investigated the properties of SiO₂ films by PECVD as a barrier. They suggested that the WVTR increased with the RF power level, resulting from the higher residual stress and increased defects. They insisted that the film formed at higher RF power may also be more hydrophilic due

to the rougher surface and this enhanced the penetration of water. They suggested that the gas and water vapor transport in barrier films

- (1) unhindered transport through ‘macrodefects’ ($> 1\text{nm}$)
- (2) hindered transport through ‘nanodefects’
- (3) hindered transport through the amorphous lattice (interstice $< 0.3\text{nm}$) [47]

There are literatures on the effects of SiH_4/NH_3 gas ratio and discharge frequency on WVTR [48], the relationship between deposition temperature and power on the mechanical properties and Si-N composition ratio [49, 50], the relationship between deposition temperature and film stress [51] and film defects [52, 53]. However, most papers concentrated on the barrier properties and the improvement of WVTR of as-deposited film. Since the main purpose of thin film encapsulation is to prevent the OLED from being damaged by moisture and oxygen, detailed study on long-term stability of barriers in severe high temperature and high humidity conditions are needed.

Inorganic/organic hybrid encapsulation film is known to be superior compared to single inorganic layer in the barrier performance in OLEDs, mainly of two reasons (Fig. 2.7).

- (1) the organic layer in nanolaminates functions as a type of resistive interlayer that appears to lengthen the diffusion path for water permeation
- (ii) nanolaminates inhibit the propagation of the defects through the multilayer structure.

Both these characteristics are beneficial as they improve the associated WVTR values [54].

The lifetime of OLED encapsulated with multilayer is much longer than that with single layer [55-57]. The inorganic oxide layers (AlO_x) act as diffusion barriers to water and oxygen while the polymer layers decouple defects in the oxide, resulting in the half lifetime of the encapsulated display was 200hrs [58]. The composite barrier consisted of alternating layers of polyacrylate films deposited by flash evaporation and then cured by UV light and an inorganic oxide showed the WVTR of $4 \times 10^{-6} \text{ g/m}^2\text{-day}$ [59].

The multilayers are usually prepared with using two or more deposition process because they are consisted of different inorganic and/or organic materials. However, combining the different deposition techniques makes the deposition system more complex and the development of an integrated system difficult for deposition of organic/inorganic multilayered coatings. A graded ultrahigh barrier (UHB) coating using PECVD can stop defects from propagating through the coating thickness. The coating consists of a graded single hybrid layer made up of inorganic and organic materials. The inorganic process utilizes a combination of silane, ammonia, and oxygen gases to create a materials composition ranging between silicon nitride and silicon oxide. While the organic process includes a combination of organosilicon precursor and Ar gases to create a Si-containing organic material [60].

P. Mandlik et al. suggested a multilayer thin film encapsulation deposited with single process of low temperature PECVD. They used just one precursor to deposit a barrier and a buffer layer, which is hexamethyldisiloxane (HMDSO) [61]. S.M. Park et al. investigated that the deposition characteristics of SiOCH and plasma-polymerized methylcyclohexane (pp-MCH) thin films and pp-MC/ SiOCH /p-MCH

multilayer structures in a PECVD chamber at low temperature [62]. With these studies, the buffer layers are formed with the plasma polymerization of PECVD. The very thin organic or hybrid layer can be prepared by the process of plasma polymerization.

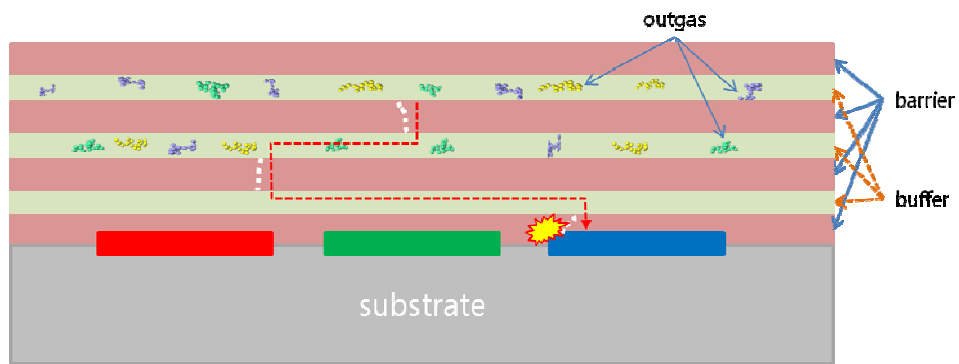


Fig. 2.7. The schematic diagram of inorganic/organic thin film encapsulation, leading to a increase of peneration pathway of moistures and outgases.

There are a few reports about polymer encapsulation using coating process. Cytop™ which an extremely hydrophobic perfluorinated polymer, appears promising as a potential candidate for one of the two alternating layers in printable organic/inorganic multilayer encapsulation. The polymer barriers resulted in improvement of half-life compared to with a device without an encapsulation polymer, but the half lifetime was just 6hrs [63]. Non-hydrolytic sol-gel derived siloxane based organic-inorganic hybrid materials (hybrimers), wherein inorganic networks such as siloxane bonds can form by a simple condensation reaction without water, have been studied for a polymer encapsulation. The WVTR for this polymer, measured by Ca-test, was in the of 10^{-2} g/m²-day [54].

G. L. Graff et al. suggested the method to predict the permeability of gases in single and multilayer thin-film barrier stacks. Additionally, they proposed design criteria for ultra-barrier films.

(1) Permeation through thin film barriers is controlled by defects. Therefore, the defect size and spatial density in the thin films are the critical parameters to determine the barrier performance of both single and multilayer barriers.

(2) The long diffusion path created by sandwiching thin polymer layers between inorganic barriers induces a large increase in lag times but a much less significant decrease in steady-state flux. The increased lag time is responsible for the improvement in barrier performance

(3) The long lifetime of OLED using multilayer barriers is possible due to lag time, not equilibrium diffusion effects.

(4) Lowering the diffusivity and solubility of the polymer interlayers will improve barrier performance. The property of polymer layer can be controlled by

the polymer selection (hydrophobic or organic/inorganic copolymer), physical modification ion bombardment or crosslinking), or chemical modification (reactive etch or plasma surface treatment).

(5) The permeation can be reduced by thinning the polymer interlayers, but this must be accomplished without compromising the smoothing properties (asperity/debris coverage) of the polymer [64].

There are key parameters for an effective encapsulation of OLEDs (Table 2.2). First of all, the WVTR and the OTR must be obtained. The water vapor transmission rate of 10^{-6} g/m²-day and an oxygen transmission rate below 10^{-5} cm³(STP)/m²-day have to be achieved to avoid degradation of OLEDs. The organic materials consisting of OLEDs between anode and cathode are very weak to thermal energy. Therefore, all the processes for forming emitting layers are conducted under the temperature of 90°C, so that the thin films for the encapsulation have to be deposited under the temperature of 90°C. Almost all deposition processes are vacuum and plasma processes. The organic materials for OLEDs can be damaged by high ion and oxygen plasma. Therefore, the energy of ion bombardment has to be low. Generally, there are two types of layers consisting of thin film encapsulation, barrier and buffer, respectively. The barrier is to limit the penetration of water vapor and oxygen and the buffer is to release the film stress of barrier and planarize the surface before forming the barrier layer. The inorganic barrier shows conformal coverage, while the organic buffer layer shows the planar coverage. The film must have moderate values depending on the substrate stress and be stable for a long time under severe environmental conditions such as 85°C and 85% of relative humidity. Most of all, the thin film encapsulation must satisfy the

specification of lifetime, so that there are some requirements such as low outgas concentration from organic buffer material and no changes in film compositions, stress, and optical properties including refractive index and transparency.

As the limited performance of single layer thin film encapsulation is due to the high defect densities, the number of defects must be reduced or the effect of defects must be reduced. Multilayer or alternating layers of thin films are widely used to minimize the propagation of defects or pinholes from one single layer to the next single layer film, improving the overall barrier performance of the structure. The propagation of defects are interrupted using either a multilayer structure of the same inorganic thin film or alternating layer structure of two or more different inorganic thin films or inorganic/organic thin films. The basic concept is to limit the propagation of pinholes and creates a tortuous diffusion pathway for the diffusing permeant molecules through the barrier.

Items	Requirements
Water and oxygen penetration	- WVTR < 1×10^{-6} g/m ² -day, - OTR < 1×10^{-5} cm ³ (STP)/m ² -day
Temperature	- Low temperature below 90°C not to damage to the organic materials of OLED
Deposition process	- Low ion bombardment - The organic materials can be damaged by sputtering with high ion energy
Coverage	- Conformal coverage : inorganic barrier - Planar (gap-fill) coverage : organic (buffer) material
Defect	- Dense and pinhole-free
Film stress	- Moderate stress depending on the substrate stress - stable for long time (> 240hrs) under severe condition (ex. 85°C/85% RH)
Reliability	- low outgas from buffer material - no changes in film compositions and optical properties for long time (> 240hrs) under severe condition (ex. 85°C/85% RH)

Table. 2.2 The key parameters and requirements for thin film encapsulation.

2.4 The properties of silicon nitride thin films

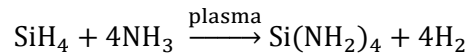
The plasma phase chemistry starts from the dissociation of the feeding molecules. The initial stage of the dissociation reactions comes from the collision of feeding molecules with energized particles such as electrons, radicals, or ions. The degree of dissociation of these molecules is probably closely related to the bond strength of each molecule. In the $\text{SiH}_4/\text{NH}_3/\text{N}_2$ system, the bond strengths are [Si-H] 90.3 kcal/mol (3.9 eV), [N-H] 107.4 kcal/mol (4.7 eV), and [N-N] 225.94 kcal/mol (9.8 eV) and the dissociation efficiency is in the order of $\text{SiH}_4 > \text{NH}_3 > \text{N}_2$.

The products of an $\text{NH}_3\text{-SiH}_4$ plasma consist of only two classes of molecules. One is a disilane and its unsaturated derivatives, Si_2H_n , and the other is aminosilanes, $\text{SiH}_{4-n}(\text{NH}_2)_n$. At low power, there is much more reaction to disilane and much less to tri-($\text{Si}(\text{NH}_2)_3$) and tetra-aminosilane ($\text{Si}(\text{NH}_2)_4$). Disilane results from silane radicals reacting with each other and with silane, therefore, the plasma is generating silane radicals, while ammonia is acting as an inert diluent toward them [65].

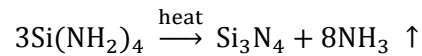
At low SiH_4 flow rate, the deposition rate rises in proportion to the $\text{Si}(\text{NH}_2)_3$ and at higher SiH_4 flow, $\text{Si}(\text{NH}_2)_3$ falls off, disilane begins to rise, deposition rate rises less steeply, and silane consumption decreases. Higher pressure eliminates disilane and increases silane consumption and deposition rate. Higher pressure helps to promote the amination reaction by the increased silane consumption and suppressed disilane. Higher pressure at fixed gas flow provides more residence time as well as more time for deposition before the products are pumped away. These trends account for the increase in deposition rate. At sufficiently high power and pressure, the amination reaction dominates and disilane formation is avoided as long as silane flow is kept below the critical flow.

At higher SiH₄ flow, Si(NH₂)₃ falls off, disilane rises, and silane consumption decreases, because there is not enough active ammonia available to consume all of the silane. The deposition rate decrease slowly with increasing NH₃ flow due to the decrease in residence time or to an increase in Si(NH₂)₄/Si(NH₂)₃ ratio. Although Si(NH₂)₄ is the end product of the amination reaction, it may be that it is unstable in the plasma environment and easily loses its first NH₂ to make the Si(NH₂)₃ radical dominant. In the Si(NH₂)₄ molecule and the Si(NH₂)₃ radical, the Si is surrounded by bonds to N. This structure forms the core of the [Si-N] network. And the hydrogen is bonded only to the N and not to the Si. Under amino-saturated conditions, both plasma composition and deposition rate are reasonably flat with variation in power and are only weak functions of pressure and ammonia flow rate.

The overall chemistry of PECVD deposition of silicon nitride from NH₃-SiH₄ under amino-saturated conditions may be written in balance equation form as a gas phase precursor-forming reaction



Followed by a surface condensation reaction



No H evolution is involved in the surface reaction. The ammonia has acted as carrier and encapsulant for the Si during transport and deposition, and then it has been returned to the plasma [66].

A condensation mechanism is proposed in Fig. 2.8. An $\text{Si}(\text{NH}_2)_3$ radical adsorbs on an N site, most likely one from which H has desorbed. Some $\text{Si}(\text{NH}_2)_4$ will likely adsorb as well, with the first NH_2 group being released in the process. Amino (NH_2) groups from neighboring $\text{Si}(\text{NH}_2)_3$'s on the surface react with each other to evolve an NH_3 , leaving a Si and a N dangling bond which combine to develop the [Si-N] network. Further beneath the surface, the material can be thought of as a [Si-N] network with some of the bonds not yet formed, the Si halves being occupied by excess NH_2 and the N halves by excess H. Condensation proceeds as long as these excess species can reach each other and combine to release NH_3 [66].

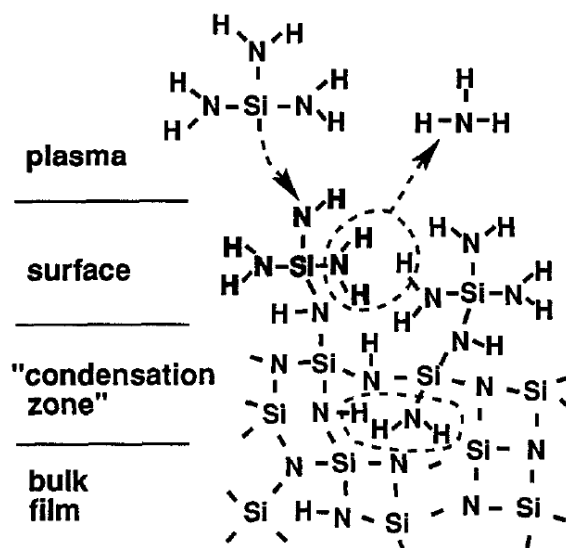


Fig. 2.8 Cross-sectional structure model of the condensation of adsorbed $\text{Si}(\text{NH}_2)_3$ toward an [Si-N] entwtor with the evolution of NH_3 [66].

Recently, a simple three-phase model is proposed to relate the physical properties (stiffness, film stress, mass density) of hydrogenated nanoporous SiN_x thin films to the volume fractions of hydrogen and pores [67].

- phase I : Dense SiN (hydrogen and pore free) made up of [Si-N] and [Si-Si] bonds. Proportions of these bonds depend on the film stoichiometry. [N-N] bonds are known for being absent of such films. The film stiffness is supposed to be mainly driven by this phase.

- phase II : Hydrogen atoms bonded to Si or N atoms. Hydrogen atoms terminate atom chains and do not transmit mechanical stress from one to another. This means that hydrogen should not participate to the global film stiffness.

- phase III : Pores and nanoscale cavities are usually found in amorphous thin films due to the long-range disorder of atom chains and to the induces bond angle misfit.

Compressive films lead to pore volume fractions as low as 2.6% in average (~17% in average for tensile films). The [Si-H] bonds are almost absent from compressive films by the steric effect associated to the large dimension of [Si-H] that prevents these bonds to form during the processing of compressive films. On the contrary, tensile films display much larger [Si-H] bond concentration (25% in average, up to 65%) confirming that the steric effect is much less important in tensile films. This discrepancy between tensile and compressive films results from the large radius of hydrogen (R_H) calculated in tensile films, which actually corresponds to the

coexistence of hydrogen atoms occupying large volumes (when bonded to Si) and hydrogen atoms occupying smaller volumes (when bonded to N), while the small R_H calculated in compressive films corresponds to the smaller volumes occupied by the [N-H] bonds. Small pore volume fraction suggests that free volumes are negligible in compressive films, which means that nanopores and/or free volumes surrounding hydrogen atoms are virtually absent.

A discontinuous behavior has been observed in stiffness evolution against negative volume fraction at the transition between tensile and compressive stress. In tensile films, H-atoms coexist with porosity to display a behaviour consistent with a pore-like behaviour. During the process of tensile films, the available free volumes are large enough to allow hydrogen to build-up large bonds, finally leading to mechanically relaxed single-bonded hydrogen atoms. This means that hydrogen atoms in tensile films are unable to transmit mechanical load. On the contrary, hydrogen atoms behave differently in compressive films. During the processing of compressive films, the bonding of hydrogen atoms is highly constrained by the surrounding atom organisation (Fig. 2.9). As a result, the free volumes are too small to allow any kind of hydrogen bonding, so that the electron cloud of a bonded hydrogen senses neighbouring atoms, leading to an extra contribution of hydrogen to the global film stiffness. Free volumes in compressive films are almost absent and the hydrogen impact on film density is no more consistent with a pore-like behaviour. The much smaller hydrogen radius observed in compressive films by the bond type ([N-H] bonds induce much less steric constraints than [Si-H] bonds do).

In the low power condition, the plasma potential is low and the ion bombardment effect on surface reactions is negligible. The deposition rate and film structure is controlled by the supply of precursors in the plasma phase and surface

reactions. Under the condition of critical power, the deposition rate increases with increase of power, resulting from the increase of dissociation efficiency. At the high power level, several film property changes suggest further enhancement of the condensation reaction. These changes include the lower linear deposition rate, higher refractive index, lower etch rate, and lower H content, although the density did not increase noticeably.

The higher power could be assisting condensation either by increasing the reactivity of the aminosilane precursors or by increasing the ion bombardment activation of the precursor condensation reactions at the growing surface.

With the increase of power, SiH_n and NH_n radical, the plasma potential and the hydrogen concentrations increase. When a small amount of hydrogen is added into the SiH_4/NH_3 plasma, it can increase the Si/N ratio in the deposited film. The increase of the ion bombardment energy can enhance the etching mechanism, which explains why the deposition rate decreases and the refractive index increases with the increase of power when it is over the critical power [67].

At high power, most of the silane is being consumed, disilane disappears, and deposition rate saturates. At higher power and with a sufficient excess of ammonia, the reaction to aminosilanes takes over, consuming 98% of the silane and preventing disilane formation. The higher power needed for this reaction indicates that ammonia requires more electron energy to activate than does silane [65].

With the SiN_xH_y from NH_3 - SiH_4 system, the film composition can vary with deposition conditions from what amounts to N-doped amorphous Si as $x \rightarrow 0$ to excess in N when $x > 1.33$. x increases with NH_3/SiH_4 flow ratio and increasing of

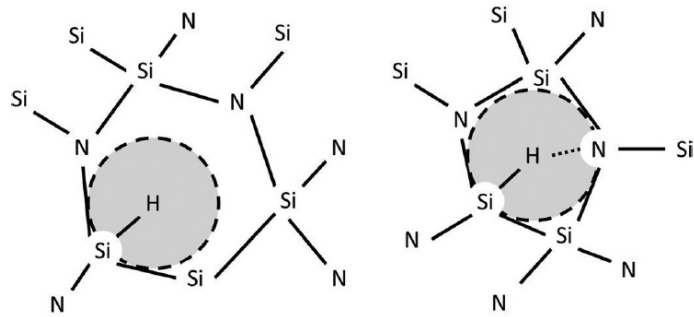


Fig. 2.9 Schematics of the behaviors of hydrogen in tensile (left) and compressive (right) films [66].

RF power. For excess N films x decreases with increasing temperature and N bonding shifts from [N-H] toward [Si-N]. The ratio of H bonded to N over that bonded to Si ($[N-H]/[Si-H]$) increases with NH_3/SiH_4 and x . Refractive index decreases with increasing NH_3/SiH_4 and with increasing $[N-H]/[Si-H]$. Etch rate in HF solutions increases with NH_3/SiH_4 and with $[N-H]/[Si-H]$. The general trend is that increasing the NH_3/SiH_4 ratio and the power lead to higher x and higher $[N-H]/[Si-H]$ which results in lower refractive index and in higher etch rate. The high NH_3/SiH_4 , high power plasma conditions result in high x , low [Si-H], maximization of $Si(NH_2)_3$ and elimination of Si_2H_6 in the plasma. When deposited under the lower power or lower NH_3/SiH_4 conditions lead to less $Si(NH_2)_3$ and more Si_2H_6 in the plasma, lower x and increased [Si-H]. These results are a consequence of the increased concentration of SiH_n radicals in the plasma, which react both with each other to form Si_2H_6 and with the film surface to incorporated Si-H and excess Si. Both H content and excess N decrease with increasing temperature, inducing an increase in mass density. Density increase causes a refractive index increase and is responsible for the decrease in deposition rate [65].

The tensile stress increases with temperature. The film densification occurs in a chemical condensation zone which extends below the surface. Elimination of volatile species (NH_3) from this zone occurs due to thermal energy input from the heated substrates and this creates dangling Si and N bonds separated by voids within which stretched [Si-N] bonds form. These bonds can not relax as they would at the surface because they are constrained by the surrounding structure so the stress is frozen in. Chemical condensation does not occur for lower deposition temperature.

RF power and chamber pressure are the main variables that affect aminosilane

formation density and ion movement in the plasma, and subsequently influence aminosilane interaction with the film growth surface. Higher RF power enhances aminosilane formation in the plasma, and in combination with lower chamber pressure, enhances ion bombardment on the substrate. The enhancement of ion bombardment in turn increases the packing density of the aminosilane on the substrate, leading to an increase in film density. stoichiometric Si_3N_4 can be formed at high enough substrate temperature, but that this stoichiometry is compromised at the lower temperatures. The lower temperature films are believed to contain a greater fraction of hydrogen, from incomplete dissociation of $\text{Si}(\text{NH}_2)_4$, in which case it may be more appropriate to describe the products as SiN_xH_y . Under such conditions the Si:N ratio would be expected to diminish, reducing the film density [65, 68].

There is a monotonic decrease in deposition rate with increasing deposition temperature. Film density and refractive index increase monotonically with increasing deposition temperature. Etch rate in buffered HF at room temperature decreases with increasing temperature [65].

The SiN_x film can be etched by the hydrogen plasma. The film deposited at low power is easy to etch with the high power hydrogen plasma, while the film deposited with higher power is very difficult to attack with the hydrogen plasma. After the hydrogen plasma exposure, the buffered HF etch time of the film increased although its thickness decreased. The refractive index of the hydrogen etched film was increased to greater than 2.5, which showed that the exposed surface became more silicon rich than the previous film. The Si/N ratio on the hydrogen exposed surface was found to be higher than that before the exposure. The hydrogen plasma preferentially removes the [N-H] rather than [Si-H] group [67].

IR spectra shows that the [Si-H] bonding in the film deposited under conditions which gave a disilane-rich mass spectrum is typically found in PECVD SiN_x but is absent in the films grown under the amino-saturated conditions, in which H appears bonded only to N. The absorptions from [N-H] and [N-H₂] both decrease with increasing deposition temperature. There is a monotonic decrease in percent H with increasing temperature.

The [Si-H] peak shifted from 2235cm⁻¹ for the Si-poor layers to 2160cm⁻¹ for the Si-rich layers. The decrease in wavenumber increases due to N incorporation and bonding to the Si in [Si-H] groups. Si-neighbours are replaced by the more electronegative N atoms, causing a decrease in the [Si-H] bond length and therefore a shift of the oscillation to higher frequency and wavenumbers, respectively.

2.5. Working principles of OLEDs

2.5.1. OLED structures

In principle, an OLED can consist of only one organic layer sandwiched between two electrodes, i.e., the anode and the cathode. However, a multilayer OLED made of several different functional organic layers is superior in terms of efficiency and lifetime because the properties of the individual layers can be tuned through the proper choice of materials. The positively biased anode is required in order to inject holes into the hole transport layer (HTL), similarly, electrons are injected from the cathode into the electron transport layer (ETL). The emission layer (EML) comprises one or more dyes emitting light in different regions of the visible spectrum. High-efficiency OLEDs often contain several additional layers like separate blocking and injection layers. An external voltage source of typically a few volts is applied to the device so that the two types of charge carriers are injected from the opposite electrodes, i.e., electrons from the cathode and holes from the anode, and drift towards each other. When the initially free electrons and holes meet, they form strongly bound electron-hole pairs (excitons) in the emission area, which then may decay radiatively and emit photons. In detail, the whole process can be separated into four fundamental steps [103].

- (1) injection of electrons and holes at the electrodes
- (2) transport of charge carriers through the organic layers
- (3) formation of bound electron-hole pairs (excitons)
- (4) radiative exciton decay and emission of light

2.5.2. Electroluminescence efficiency

In most of the conventional small molecule organic materials only the radiative decay of singlet excitons is responsible for generating light and the energy of triplet excitons is wasted because of the slow radiative decay and generates delayed fluorescence. Thus the internal quantum efficiency η_{int} (the ratio of the total number of photons generated within the organic emitter to the number of injected electrons) of fluorescent OLEDs is only 25% [104]. It has been demonstrated that the internal quantum efficiency of OLEDs can be achieved near 100% by means of harvesting both singlet and triplet molecular excitation states using electrophosphorescent materials, which is nearly fourfold increase in efficiency as compared to singlet harvesting fluorescent organic materials [105, 106]. The external quantum efficiency η_{ext} (ratio of the total number of photons emitted by the OLED into the viewing direction to the number of electrons injected into organic emitter) of an OLED device is related to the internal quantum efficiency η_{int} and the external coupling efficiency η_{coupling} (the ratio of the total number of photons coupled out in the forward direction to the number of injected electrons) by the following relation [107, 108]

$$\eta_{\text{ext}} = \eta_{\text{int}} \eta_{\text{coupling}} = \gamma \eta_{\text{exc}} \Phi_p \eta_{\text{coupling}}$$

The internal quantum efficiency of OLEDs is mainly affected by the non-radiative electron hole recombination loss and the singlet–triplet branching ratio [104, 107, 108]. Most of the electro-phosphorescent OLED materials have very small non-radiative loss. On the other hand, despite achieving near 100% internal

quantum efficiency, the external coupling efficiency ($\eta_{\text{ext coupling}}$) of the conventional OLED device remains very low. Only a fraction of the light will in the end be able to leave the device to the outside world. The reason is that light is generated in a region of the OLED stack with higher refractive index than the glass substrate and, obviously, ambient air. Assuming isotropic emission in the organic layer and a perfectly reflecting cathode, the fraction of generated light escaping from the substrate is [107, 109]

$$\eta_{\text{ext coupling}} = \frac{1}{\xi n^2}$$

where n is the refractive index of OLED material and ξ is a constant that depends on the dipole alignment and the geometry of the OLED device. For most of the organic materials n is about 1.7 and taking the value of 2 for ξ , the internal coupling efficiency is only about 20% [110].

The light is generated from thin organic emitting layer spontaneously in all the directions and propagates via various modes, that is, external modes (escape from the substrate surface), substrate-, and ITO/organic wave-guided modes due to total internal reflection (TIR) as depicted in Fig. 2.10.

For incidence angles larger than critical angle TIR occurs as can be seen from Fig. 2.10 and because of which $\sim 30\%$ light is trapped inside the glass substrate and $\sim 50\%$ light is propagated through ITO-organic wave-guided modes shown by dotted lines. Viewed from the emitter position the light escape cone has an opening angle of some 30° with respect to the surface normal and the energy contained in it typically amounts to less than 20% of the total energy. This is followed by the

contribution of substrate modes, where total internal reflection at the glass-air interface is the limiting process.

This contribution is comparable in energy also at around 20%. For higher emission angles the light cannot even reach the glass substrate, but is wave-guided in the organic layers (including the transparent indium-tin oxide electrode) and in the end lost by residual absorption or edge emission. Finally, the emitter can couple to the evanescent field of surface Plasmon polaritons (SPPs) traveling at the interface between the metal electrode and the organic layers. Quantitative calculations, treating the emitting molecules as classical electrical dipoles, reveal that in planar OLED stacks typically around 50% of the light is trapped in waveguided and Plasmon modes.

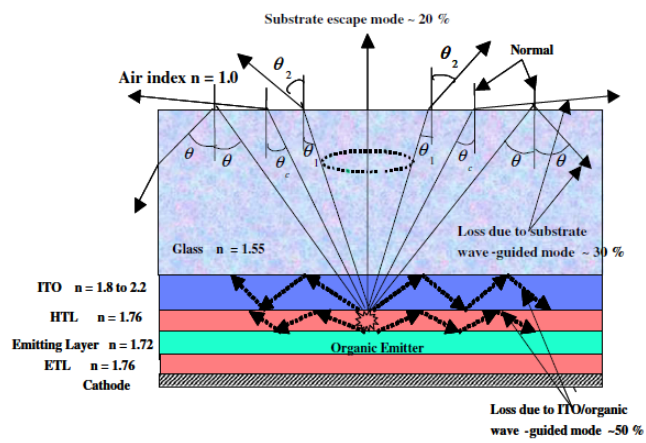


Fig. 2. 10. Schematic of multi-layer OLED structure and optical ray diagram of light propagation via various modes [110].

For the purpose of applications in general illumination and flat-panel displays, light emitted from the substrate surface (external modes) is only 20% of the total emitted light from inside the OLED device. [103, 110].

According to classical ray optics theory about 80% of generated light is lost in wave-guided modes due to glass substrate and ITO/organic material (Fig. 2.10) which means that the majority of the light is either trapped inside the glass substrate and device, or emitted out from the edges of an OLED device. The external quantum efficiency η_{ext} of OLED is given by as follows [107],

$$\eta_{\text{ext}} = \frac{q \int \lambda I_{\text{det}}(\lambda) d\lambda}{h c f I_{\text{OLED}} \int R(\lambda) d\lambda}$$

where q is electronic charge, λ is wavelength, $I_{\text{det}}(\lambda)$ detected photocurrent, h Planck's constant, c speed of light in vacuum, f is OLED-to detector coupling factor, I_{OLED} is current and $R(\lambda)$ is the detector responsivity.

2.5.3. micro-cavity structure

An OLED can be regarded as one-dimensional micro-cavity because the total thickness of organic films in the device is of the order of wavelength of light. There are two types of micro-cavities in OLED, that is, weak and strong micro-cavities. Weak microcavity is formed with the conventional OLED structure due to the metal cathode and high refractive index anode (ITO) while a strong micro-cavity OLED structure usually consists of a metal mirror on one side and a highly reflective dielectric multilayer structure on the other side. Lee et al. [111] studied the effect of

micro-cavity on the light extraction efficiency of OLEDs. They have demonstrated that the substrate wave-guided modes of an OLED structure strongly depend on the optical cavity length of the device due to weak cavity effect. It was found that the ratio of the extracted mode to the substrate-guided modes varies from 22% to 55% depending on the location of recombination zone. They predicted that more light is trapped in the substrate and organic/ITO layers if the distance between the recombination zone and the cathode exceeds the quarter wavelength value.

A strong micro-cavity determines the electric field mode distribution, which in turn modify exciton spontaneous emission life-time and the quantum efficiency and hence electroluminescence spectrum and intensity is enhanced [95-100]. The spontaneous emission intensity is enhanced in the forward direction due to multiple beam interference between the light reflected from the two reflectors. Further, since the photon density of state is redistributed only certain wavelengths that satisfy the cavity resonance modes are emitted and a significant spectral narrowing also takes place. Such spectral narrowing with enhanced forward EL emission can lead to the generation of high purity multiple color generation widely applicable for OLED flat-panel displays.

In top-emitting OLEDs the strength of the optical interference effects depends critically on the reflectivity of the metal cathode, and accordingly, controlling the cathode reflectivity is a further degree of freedom in tailoring the emission characteristics. The thickness variation of the cathode metal is one possibility to change the reflectivity. However, this approach has the disadvantage of increasing absorption losses for thicker metal cathode. A preferred concept, known from the optics of metal coatings, utilizes a thin dielectric layer on top of a thin metal film to modulate the transmittance of the cathode.

The general functional behavior of the efficiency curves and also the I-V characteristics are not influenced by the deposition of the dielectric layer. This indicates that the electrical properties of the OLED, including the charge balance factor, are not affected by the capping layer. In other words, the number of generated excitons in the OLED is identical: however, the number of photons detected externally in the solid angle considered is significantly affected by a modification of the optical structure. Adjusting the dielectric layer thickness can be used to design the spectral characteristics, the angular intensity distribution and the angular dependence [101].

Using the optical model, the device structure of the top emitting OLEDs could be optimized by matching of index match layer(IML). The thickness, the refractive index, the matching of the ML optical property and the device structure is a main design factor of the optimization. From this study, the higher the IML refractive index becomes, the thinner the optimum IML thickness becomes in turn [102].

2.5.4. Objectives

The thickness of the barrier for OLED encapsulation is becoming thinner. Much research has been carried out to improve the barrier performance to prevent moisture permeation. However, the research on the changes of thin film property with time and their effect on the device performance has hardly progressed.

Therefore, in this study, we investigated the oxidation characteristics of SiNx barrier, which is widely applied as a thin film barrier, when stored in a high temperature and high humidity atmosphere. The stress and refractive index changes of the SiNx barrier as the oxidation progresses were investigated and the major

factors of the oxidation reaction were studied through the analysis of the chemical bond, binding energy, and morphology change. This study suggests that the chemical bond structure and the film density are key factors for obtaining the oxidation resistance of SiN_x barriers.

The top light emitting diode uses the cavity structure to optimize the light extraction characteristics. Conventionally, the light from cathode of OLED emits into the air with refractive index of 1, while there is a barrier layer on the cathode, which has a larger refractive index than air. Therefore, the structure, material, and thickness of the thin film encapsulation affect the optical characteristics and light extraction of the device. In this study, the absorption and reflection of the barrier layer and the buffer layer, which form the thin film encapsulation structure, are calculated according to the refractive index and thickness. Also, the change of reflection due to the thinning of the barrier thickness was confirmed, and the reflection characteristic as the oxidation proceeded was also studied. It has been confirmed that not only barrier performance but also film stress and oxidation stability are important in the development of thin film encapsulation technology.

3. Experiments

3.1 Film Preparation

SiN_x barrier films were deposited on a wafer and a glass by PECVD at 85 °C using SiH₄, NH₃, N₂, and H₂ as reactant gases. The PECVD was equipped with a load lock chamber to prevent the exposure of processing chamber to air. All samples were prepared at 85 °C and the variation of temperature during deposition was controlled within ±1 °C. The RF power was 0.68W/cm² at 13.56MHz. The chamber was cleaned with remote plasma self cleaning system using NF₃ gas after deposition of predetermined thickness, so that we could control the particles.

For the study of oxidation and the improvement of barrier performance, the gas flow rates were changed while other deposition conditions such as pressure, RF power, spacing, and temperature were kept constant.

3.2 Oxidation of SiN_x barriers

Oxidation experiments of the SiN_x barrier proceeded at a constant temperature and humidity (Jeitech Co.). The oxidation condition was 85 °C/ 85% RH and the wafer and glass substrate were stored in a chamber.

3.3 Simulation of SiN_x barrier

Multilayer structure reflection simulation was performed using a program published by filmetrics. Since the region where the light is generated is inside the OLED element, it is calculated on the assumption that there is no change in the emission region. Therefore, calculation was performed on the cathode electrode and

the thin film encapsulation structure.

3.4 Film Characterization

The ellipsometry (Woollam, M2000) was used to determine the thickness and refractive index of thin films on Si-wafers. Then the deposition rate was calculated from the average thickness and deposition time. The thickness of films were 500nm and the non-uniformity was within $\pm 5\%$.

The mechanical stress in the substrate/film system across the film thickness and the substrate manifests itself in the form of bending. The film stress was measured by stress gauge (FSM, 128G).

The quantitative determination of the thin film stress, σ_f , via the thin film's stress induced substrate bending is performed according to the Stoney equation.

$$\sigma_f = \frac{E_s}{6R(1 - \nu_s)} \frac{d_s^2}{d_f}$$

Where E_s , ν_s , and d_s are Young's modulus, Poisson ratio, and thickness of the substrate, respectively. R is the experimentally obtained substrate's radius of curvature, and d_f is the thickness of the thin film.

If the stress is too high, the film induces defects in the substrate material or tends to peel off. High tensile stresses cause cracking of the film. Therefore, the low compressive stresses are usually preferred.

The changes in stress were obtained by measuring the wafers before and after storing the SiN_x coated wafers in a humidity chamber, operated at 85°C and 85% relative humidity. The SiN_x films did not peel-off during storage in the humidity

chamber.

The thickness, deposition rate, refractive index, and film stress for the films of oxidation and improvement of barrier performance were deposited five times to confirm the repeatability and reproducibility.

Measurements of WVTR were carried out using MOCON, Inc. instruments. The thickness of films for WVTR was 200nm because the WVTR with film thickness of 500nm showed the value more than the measuring range.

The Fourier transform infrared spectroscopy (FTIR, Nicolet, iS10) spectra were recorded in the range of $400 \sim 4000\text{cm}^{-1}$. The chemical composition of thin films was analyzed by X-ray photoelectron spectroscopy (XPS, Sigma Probe) and Auger electron spectroscopy (AES, PHI/Perkin-Elmer).

The cross-section images of thin films were taken by transmission electron microscopy (TEM, Tecnai, F20). The morphology and surface roughness were measured by atomic force microscopy (AFM, JEOL, JSPM-5200).

4. Results and Discussion

4.1 Oxidation of SiN_x barriers

4.1.1 Introduction

The thin film for encapsulation is required to be much denser to improve the barrier performance. In addition, as seen in previous chapter, it was crucial to obtain the stability for long time in the severe environment, such as 85 °C and 85% relative humidity. There were reports that additional gas such as Ar could help to increase the film density. Using the inert gas, the ion bombardment causes the increase of film density.

The dilution of the NH₃/SiH₄ reactant with excess hydrogen leads to significant changes in the properties of plasma-deposited SiN_x:H films resulting from changes in both composition and bonding. The observed changes in the physical properties and bonding indicate an increase in film density with increasing hydrogen partial pressure.

The Si-N network was formed with the ammonia condensation reaction by combining the [N-H] bond and the amino bond, [N-H₂], leaving the ammonia, NH₃. The addition of hydrogen gas to the feeding gas accelerated the amino (NH₂) removal, and then the condensation reaction increase, resulting in the increase of [Si-N] network. In the NH₃/SiH₄ plasma, the film growth proceeded via the absorption of an aminosilane radical on an available nitrogen site at the film surface. Neighbouring amino groups could then react with each other to evolve an ammonia

molecule, leaving a nitrogen and silicon dangling bond which combine to develop the [Si-N] network. This process causes a denser and more compact nitride film.

Thin film barriers are mostly inorganic materials such as AlO_x by sputtering, AlO_x by atomic layer deposition (ALD), and SiN_x or SiON or SiO_x by plasma enhanced chemical vapor deposition (PECVD). PECVD at low temperature is the most favorable tool considering its large size scale-up capability and short processing time. There are literature on the effects of reactant gas ratio and discharge frequency on WVTR, the relationship between deposition temperature and power on the mechanical properties and composition ratio, and the relationship between deposition temperature and film stress and film defects.

However, most papers concentrated on the barrier properties and the improvement of WVTR of as-deposited film. Research on thin film encapsulation has mainly progressed in two directions: One is lowering the water vapor permeability by developing new materials, and the other is by optimizing the thin film structure by stacking inorganic and organic layers alternatively to lengthen the diffusion path. Since the main purpose of thin film encapsulation is to prevent the OLED from being damaged by moisture and oxygen, more studies on long-term barrier stability in severe conditions such as high temperature and high humidity are needed.

In this part, we examined the long-term stability of SiN_x thin film, which is the most used barrier material for thin film encapsulation. Silicon nitride deposited by PECVD at low temperature has been applied to the mass-production of OLED.

SiN_x thin films with similar compressive stresses and WVTRs but different NH_3/SiH_4 gas ratios during deposition were used to investigate the changes of film properties during long-term storage in high temperature (85 °C) and high humidity

(85%, relative humidity) conditions.

4.1.2 The properties of as-deposited SiN_x film

Table. 1 gives the refractive index, WVTR, and atomic concentration measured by XPS. The film thickness was fixed because the refractive index and the film stress can be affected by the film thickness [106]. The refractive index of the samples decreased from 1.93 to 1.81 with increased NH₃/SiH₄ gas ratio because the amount of nitrogen and hydrogen incorporated in the film increased. The atomic concentration measured by XPS indicates that the ratio of N/Si increased because the Si 2p decreased and the N 1s increased with higher NH₃/SiH₄ gas ratio. With decreased NH₃/SiH₄ gas ratio, the refractive index increased due to the formation of a Si-rich film. Table 4.1 suggests that the barrier performances were similar, in the range of 0.046 – 0.065 g/m²-day, although there was slight variation in the refractive index. The films with similar barrier characteristics were chosen to study the long-term stability as a function of film composition.

Increasing NH₃ gas flow rate enhanced the film stress from compressive 153MPa to compressive 163MPa. On the other hand, the film density decreased from 1.996 to 1.895.

The data of refractive index, WVTR, and atomic concentration measured by XPS were summarized in Table. 4.2. The addition of H₂ gas during deposition induced the increase in refractive index to 1.90 and film stress to compressive 213MPa. Also, the film density was increased to 1.922. The WVTR was decreased to 0.042 g/m²-day, while the WVTR of SiN_x film deposited without H₂ gas addition was 2.4 g/m²-day

In addition, the wet etch rate decreased from about 3600nm/min to 900nm/min. These results imply that the film became much denser with the addition of hydrogen gas during deposition process.

The refractive index increased when deposited SiN_x films with a addition of hydrogen gas as a reactant. There is a linear relationship between the refractive index and the [Si-H] ratio and [Si-H]/[N-H] ratio, suggesting that [Si-H]/[N-H] ratio is the only a function of the Si/N ratio. At high ratio Si/N ratio, almost all the hydrogen atoms are bond to silicon [97].

The increase of NH_3 flow rate results in a higher percentage of nitrogen-related species within the plasma. Therefore, the species dissociated from NH_3 decrease the number of nucleation sites that are responsible for the film growth. This will decrease the deposition rate.

Since NH_3 is responsible for the inhibition of the adsorption of SiH_4 , a decrease of the NH_3 flow rate is responsible for a decrease of the N/Si ratio and therefore a increase of the refractive index. The refractive index decreases with increasing NH_3/SiH_4 gas flow rate ratio due to the fact that the films become N-rich films as the amount of silane decreases. Increasing the NH_3 gas flow rate introduces a large number of N atoms incorporated into the films, which gives rise to more [N-H] bond because the N atom is more electronegative than Si atom.

The increase of NH_3 resulted in a rise in the nitrogen content and intensify the non-uniformity within the deposited film and consequently increase the stress.

The deposition rate as a function of the amount of hydrogen added to the reactant gases was found to be decreased. The decrease in the deposition rate suggests that the film density increases with the addition of hydrogen gas. The addition of hydrogen gas resulted in the increase of stress. The decrease in NH_2

content and increase in compressive stress when H₂ addition to the feeding gas was employed reveal that some interaction with the growth process of the film was occurring. The hydrogen dilution increases the hydrogen growth surface coverage, helping to relax the growth film surface while increasing radical diffusion lengths. This abundance of hydrogen at the growth surface enhances amino removal, complementing the condensation reaction. Hence, the tensile stress caused by the condensation reaction is reduced and the film structure becomes more compact. Amino removal leads to a denser, more compact nitride film structure [81].

NH ₃ /total gas ratio	Refractive index	WVTR (g/m ² -day)	Stress (MPa)	Density (g/cm ³)
0.034	1.93	0.054	-153	1.996
0.057	1.87	0.065	-154	1.901
0.073	1.86	0.046	-154	1.928
0.122	1.81	0.058	-163	1.895

Table. 4.1. The effect of NH₃ gas ratio on the physical properties of as deposited SiN_x barrier films

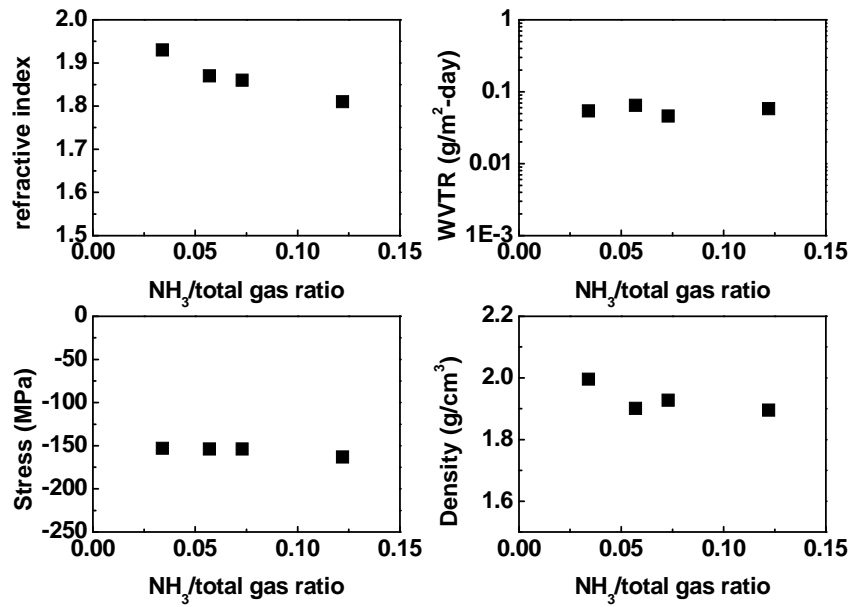


Fig. 4.1. Effects of NH_3 gas flow ratio on the refractive index, WVTR, film stress and density of as-deposited SiN_x barriers.

H ₂ /total gas ratio	Refractive index	WVTR (g/m ² -day)	Stress (MPa)	Density (g/cm ³)
0.48	1.80	0.159	-102	1.852
0.58	1.82	0.095	-123	1.881
0.65	1.86	0.045	-153	1.928
0.69	1.90	0.042	-213	1.922

Table. 4.2. The effect of H₂ gas ratio on the physical properties of as-deposited SiN_x barrier films

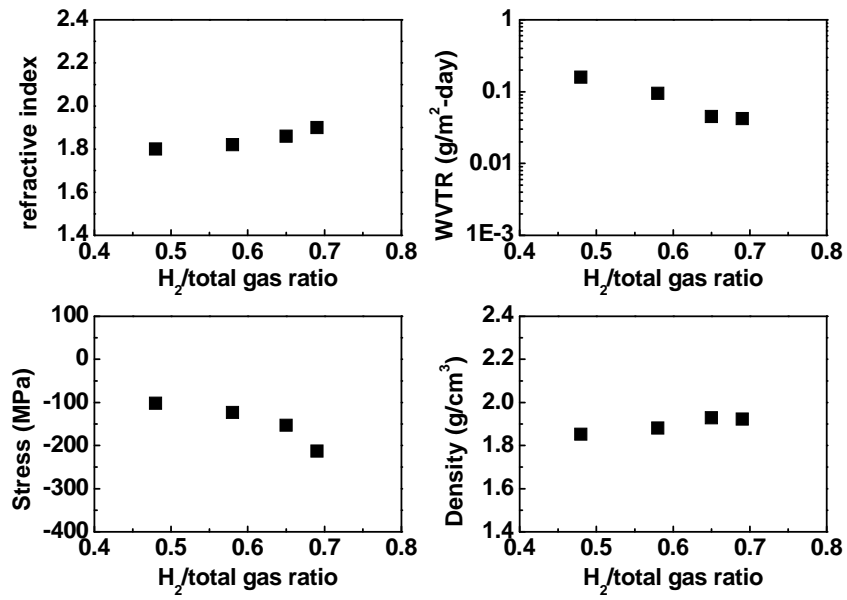


Fig. 4.2. Effects of H_2 gas flow ratio on the refractive index, WVTR, film stress and density of as-deposited SiN_x barriers.

4.1.3 The acceleration test of SiN_x thin film barriers

The change of refractive index and film stress while storing in the condition of 85°C/85% RH chamber were drawn in Fig. 4.3. We found that the refractive index and film stress became smaller as the storage time in the humidity chamber was increased. Also, the variations of refractive index and stress increased gradually with the increase in NH₃/SiH₄ gas ratio. The differences of refractive index and stress before and after the storage for 240 hrs in a humidity chamber are summarized in Table 4.3. The refractive index of the film with R=0.034 was reduced from 1.93 to 1.91, showing a variation of -0.8%, while the R.I. changed from 1.81 to 1.44, showing a variation of -20.6% for the film with R=0.122. The value of 1.44 corresponds to that of SiO_x. The film stress with R=0.034 decreased by 0.8% from -153.3 MPa to -152.0 MPa, while the film with R=0.122 showed the change from -162.7 MPa to -98.0 MPa, having a 39.7% decrease. From Fig. 4.3, one can also find that the stress with R=0.073 rapidly increased after 200 hrs.

Also, we found that the film stress changed with the amounts of hydrogen flow and duration time in the humidity chamber. The compressive stress with the ratio of hydrogen, 0 and 0.48, changed abruptly to the tensile stress and then were kept at constant value. The stress of the films above 0.65 of the hydrogen ratio represented about 30% and 10% decrease after 240hrs storage in the humidity chamber, which were likely to be stable.

Both stress and refractive index were decreased largely in the films deposited with a higher NH₃ or a lower H₂ gas flow ratio.

The decreased refractive index of SiN_x thin films with a higher N content exhibited that the SiN_x film changed to SiO_x film. Also, the stress of film with a

NH ₃ /Total gas ratio		0.034	0.057	0.073	0.122
Stress (MPa)	0hr	-153.3	-153.7	-153.7	-162.7
	240hr	-152.0	-104.0	-96.0	-98.0
	Δ	0.8%	32.3%	37.5%	39.7%
Refractive index	0hr	1.93	1.87	1.86	1.81
	240hr	1.91	1.75	1.69	1.44
	Δ	0.8%	6.5%	8.9%	20.6%
H ₂ /Total gas ratio		0.48	0.58	0.65	0.69
Stress (MPa)	0hr	-95.0	-122.9	-155.0	-213.1
	240hr	+87.0	+92.0	-112.0	-196.0
	Δ	186%	175%	27%	8%
Refractive index	0hr	1.80	1.82	1.86	1.90
	240hr	1.44	1.44	1.69	1.88
	Δ	20.0%	20.9%	8.6%	1.1%

Table. 4.3. Film stress and refractive index of SiN_x films with NH₃ and H₂/total gas flow ratio after acceleration test for 240hr in the condition of 85 °C/85%RH.

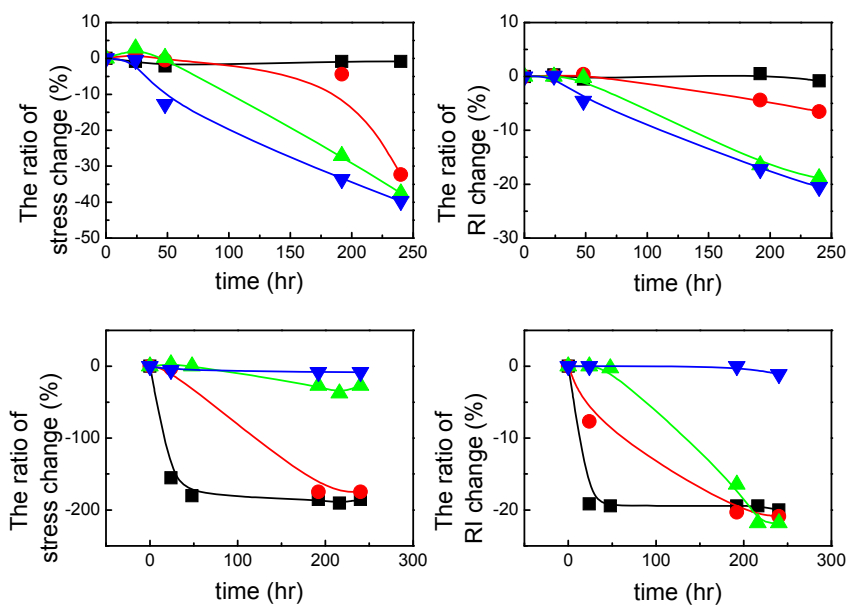


Fig. 4.3. The changes of film stress and refractive index with a storing time in the 85°C and 85% RH chamber. For fig. (a) & (b), NH₃/total gas flow rate : ■ 0.034, ● 0.057, ▲ 0.073, ▼ 0.122 ; For (c) & (d), H₂/total gas flow rate : ■ 0.48, ● 0.58, ▲ 0.65, ▼ 0.69

larger change in the refractive index decreased significantly, changing from compressive to tensile. The relationship between the stress of SiN_x and hydrogen content have been reported. They reported that the [N-H] bonding ratio compared to the [Si-H] bonding ratio had a linear relationship with film stress. The film stress decreased with a formation of defect due to the change of hydrogen content, especially changing from compressive to tensile [104].

Fig. 4. 4 provides the FTIR spectra for a series of SiN_x films grown under different NH_3 or H_2 /total gas flow ratio. In Fig. 4.4, we can clearly find that for all the as-deposited SiN_x films, [Si-N-Si] stretching mode ($835 - 841 \text{ cm}^{-1}$), [$\text{Si}_2\text{N-H}$] rocking ($1172 - 1178 \text{ cm}^{-1}$), [SiN- H_2]bending (1533 cm^{-1}), [Si-H] stretching ($2146 - 2154 \text{ cm}^{-1}$), and [$\text{Si}_2\text{N-H}$] stretching (3351 cm^{-1}) absorption peaks was much stronger than all the other oscillation modes, which is in good agreement with the results in literature for pure silicon nitride films. The IR spectra shown in Fig. 4.4 showed that the [Si-N] peak increased while [N- H_2], [Si-H], and [N-H] peak decreased with increasing the hydrogen flow rate. We found that the Si-H bond increased with the addition of hydrogen to the reactant gases, compared to the hydrogen-free deposited SiN_x film. In addition, the [Si-O] peaks were observed due to the natural surface oxidation by moisture and oxygen. The [Si-O] peak of film deposited without the addition of hydrogen gas was largely enhanced compared to the film deposited with the addition of hydrogen gas as a reactant.

The frequency of the [Si-H] stretching mode in IR absorption of the films increases with increasing compressive stress. The relationship between the film stress and the frequency of the [Si-H] and [N-H] stretching mode. The position of the [Si-H] stretching mode shifts toward high frequency with increasing compressive film stress, while that of the [N-H] stretching mode shifts toward low frequency. The

shift observed in the [Si-H] mode is larger than that in the [N-H] mode [110].

The major asymmetric absorption near 840cm^{-1} has been ascribed to four different states of the [Si-N] stretch mode assigned to $800, 835, 950, 1015\text{cm}^{-1}$ and an absorption around 1180cm^{-1} due to [N-H] bending mode. With increasing hydrogen flow ratio at the fixed SiH_4/NH_3 flow ratio, one can find the decrease in deposition rate, refractive index and etch rate but the total hydrogen content increases. A relatively small amount of hydrogen resulted in an increase in the Si/N ratio, increasing the silicon content, bonded hydrogen content, and [Si-H]/[N-H] bond ratio [111].

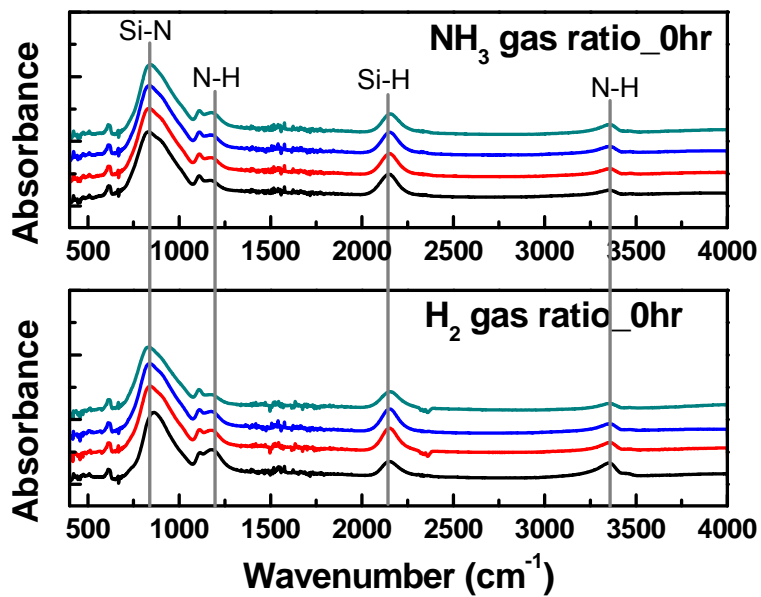


Fig. 4.4. The FT-IR spectra of as-deposited SiN_x films with NH₃ and H₂ gas flow rate. NH₃/total gas flow rate — 0.034, — 0.057, — 0.073, — 0.122 ; H₂/total gas flow rate — 0.48, — 0.58, — 0.65, — 0.69

The IR absorption peaks of the films after storage for 240 hrs in the humidity chamber are shown in Fig. 4.5. [Si-O-Si] rocking ($461 - 471 \text{ cm}^{-1}$) and [Si-O-Si] stretching ($1072 - 1084 \text{ cm}^{-1}$) peaks were detected for all samples after storage in the humidity chamber. Also [Si-O-Si] bending (802 cm^{-1}) and [Si-OH] stretching (957 cm^{-1}) peaks started to appear for the films of $R=0.122$. When R is increased, the intensity of [Si-O] rocking and [Si-O] stretching peaks increased, while the intensity of [Si-N], [Si-H], and [N-H] stretching peaks decreased. After storage in the humidity chamber for 240 hrs, the intensity of [N-H] rocking, [N-H₂] bending, and [N-H] stretching were reduced and [N-H₂] bending peaks disappeared from all the samples. The peak around $1450 - 1454 \text{ cm}^{-1}$ is an intermediate [Si-N=O] bond [107]. The FTIR spectra indicate that the SiN_x barrier films were oxidized by water and oxygen. The FTIR results suggest that the larger the NH₃/SiH₄ gas flow ratio, the faster the oxidation proceeds. Silicon nitride films can be oxidized by water vapor at a high temperature. [Si-N-Si] and [Si-N-H] bonds react with water and form a thermodynamically more stable [Si-O-Si] and/or [Si-OH] bond.

For the film $R=3.2$, the reason why Si-H stretching peak disappeared is that [N-Si-H] bond turns into a thermodynamically more stable [Si-O-Si] and/or [Si-O-H] bond reacting with H₂O molecules [107].

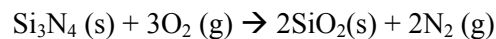
In the infrared spectrum, for the same chemical bond or the same oscillation mode of analogous configuration of chemical bonds, the bond length is always related to the wave number of absorption peak position. The oscillation of chemical bond with shorter bond length (more bond energy) needs absorbance of infrared wave with larger wave number (more more absorbing optical energy). The excessive silane or ammonia could not bring more [Si-N] bonding to synthesize silicon nitride, but only [Si-H] or [N-H] bonding [95].

The dissociation of [N-H] bond is more difficult than the [Si-H] bond in the same condition of plasma discharge. As a consequence, much lower ratio of silane to ammonia other than 3/4 was required to obtain silicon nitride film with stoichiometric ratio.

The [Si-H] peak shifted from 2235cm^{-1} for the Si-poor layers to 2160cm^{-1} for the Si-rich layers. This can be described with a model based on the different electronegativities of silicon, nitrogen, and hydrogen (respectively 1.8, 3.02, and 2.01).

The film deposited with N_2 instead of NH_3 contains less total hydrogen and usually very little [N-H] bond, because between 80~90% of the total hydrogen in a SiN_x film is from NH_3 . Increasing the NH_3 gas flow rate introduces a large number of N atoms incorporated into the films, which gives rise to more [N-H] bond because the N atom is more electronegative than Si atom. The concentration of [Si-N] bonds increased since weak Si-Si bonds are replaced by strong [Si-N] bonds with an increasing number of N atom incorporated into the film. As for [Si-N] stretching mode of the $[\text{N}_n\text{-Si-H}]$ bonds, an increasing n resulted from more NH_3 gas flow leads an increased peak wave number of the Si-N frequency [108].

The oxidation of SiN_x film by water vapor and oxygen proceeds as below:



As confirmed in the changes in the FTIR absorption peaks, the concentration of nitrogen in a silicon nitride film decreases and the oxygen concentration increases because [Si-N] or [N-H] bonds react with water vapor and oxygen to form [Si-O]

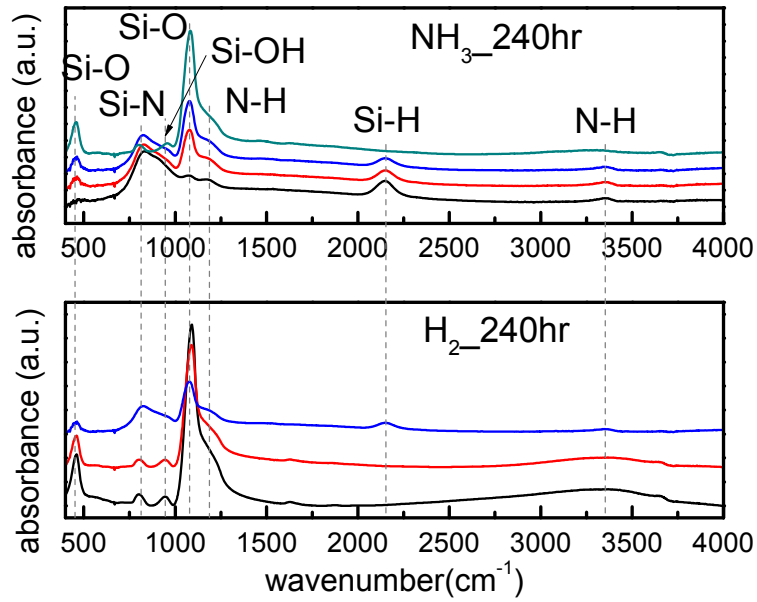


Fig. 4.5. The FT-IR spectra of SiN_x films after the acceleration tests at the condition of 85°C and 85% RH chamber for 240hrs. NH_3 /total gas flow rate — 0.034, — 0.057, — 0.073, — 0.122 ; H_2 /total gas flow rate — 0.48, — 0.58, — 0.65

bonds [95, 109].

The [Si-H] peak intensity decreased and the [N-H] peak intensity increased with a higher NH_3 gas ratio. While the [Si-H] peak intensity increased with increasing H_2 gas ratio, but the [N-H] peak intensity decreased.

With increasing NH_3 gas flow rates, the [Si-N] peak intensity and [Si-N] bond density were reduced and more [N-H] bond was formed than [Si-H] bond.

The addition of H_2 gas to the deposition process induced the increase in film density, showing the increase of [Si-N] peak intensity. The [Si-H] bond would increase with an addition of H_2 gas to the deposition process but it would be reduced with an excess H_2 gas. The [Si-H] bond decreased when the ratio of H_2 to SiH_4 was above 10, showing the increase of [Si-N] bond and film density[110].

Fig. 4.5 represented the IR spectra after 240hrs duration in the 85°C and 85% relative humidity chamber. It was clear that the Si-O peaks dramatically increased while the [Si-N], [Si-H], and [N-H] peaks decreased and disappeared. The [Si-H] and [N-H] peaks were not found in the films with the ratio of hydrogen flow, 0 and 0.74. The hydrogen addition to the feeding gas decreased.

The peak intensities of [Si-N], [Si-H], and [N-H] decreased while the [Si-O] peak intensity increased drastically with a higher NH_3 or a lower H_2 gas flow ratio.

The mass density of films with a variation of NH_3 gas flow rate was little different but the one with changing H_2 gas flow rate showed a little difference. We found that the film as a function of NH_3 gas exhibited a bond density difference compared to mass density, while the film with varying H_2 gas showed the mass density difference compared to the bond density. These differences resulted in the oxidation rate of SiN_x thin films. The oxidation could be caused by density and bonding configuration of SiN_x films.

The peaks of wavenumbers between 2800 and 3700 cm^{-1} represent Si-OH and H₂O, indicating the penetration of H₂O molecules into the inner film.

The [N-H] peak at 3352 cm^{-1} was broadened due to the increase of [Si-OH].

The peak positions of SiN_x thin films were summarized in Table 4.5. The Si-N peak position of as-deposited films with increasing NH₃ gas flow rate showed the blue shift from 835 cm^{-1} to 841 cm^{-1} . However, the peak position of films stored at the condition of 85 °C/85% chamber for 240hrs showed the opposite.

The [Si-N] peak positions of initial films showed blue shifts, but shifted to the shorter wavenumber, which suggested the film became Si-rich. The blue shift of [Si-N] peaks showed the silicon-rich films.

With the films varying NH₃ gas flow rate, the shift to a large wavenumber of Si-H stretching peak position indicated the reduction of nitrogen content in the film. Also, the wavenumber decrease of [Si-N] peak position showed that the SiN_x film changed to Si-rich [130].

vibration type / NH ₃ /total gas ratio	Peak wavenumber (cm ⁻¹)							
	0 hrs				240 hrs			
	0.034	0.057	0.073	0.122	0.034	0.057	0.073	0.122
Si-O-Si rocking	-	-	-	-	471	465	463	461
Si-N stretching	835	837	839	841	833	829	825	-
Si-O-Si stretching	-	-	-	-	1072	1078	1078	1084
N-H rocking	1172	1178	1176	1178	1169	-	-	-
Si-H stretching	2146	2150	2152	2154	2146	2148	2152	-
N-H stretching	3351	3351	3351	3351	3350	3352	3352	3352

Table. 4.4. Infrared vibrations observed in the sample before and after the reliability test at the condition of 85 °C and 85% RH.

As confirmed in the changes in the FTIR absorption peaks, the concentration of nitrogen in a silicon nitride film decreases and the oxygen concentration increases because [Si-N] or [N-H] bonds react with water vapor and oxygen to form Si-O bonds [95, 109].

The changes in Si 2p bonds and binding energies were measured by XPS (Fig. 4.6). The positions of binding energy showed that there were [Si-Si] (99.5eV), [Si-N] (101.9eV), and [Si-O] (103eV) bonds in the as-deposited films. However, after 240hrs in the humidity chamber, the [Si-Si] peak disappeared, and the [Si-N] peak was reduced to be small enough to disappear. While most of the peak areas are corresponded to [Si-O] bonds. Fig. 4.6. represented the peaks for the gas flow ratio of $\text{NH}_3/\text{total gas flow rate}=0.034$, but all samples showed the same results.

The changes in binding energies of all samples were shown in Fig. 4.6. The [Si-N] peaks decreased with increasing $\text{NH}_3/\text{total gas flow ratio}$, While the intensities of [Si-O] peaks increased. We found that the binding energies of Si-O peak were shifted from Si-O_x (102.7 eV) to SiO_2 (103.4 eV). The film deposited with the flow ratio of $\text{NH}_3/\text{SiH}_4=0.122$ changed completely to SiO_2 film.

The [Si-Si], [Si-N], and [Si-O] bonding appeared in the as-deposited film, but the [Si-N] bonding peak decreased to very small amount after the reliability test.

The type of Si 2p and binding energy were shown in Fig. 4.7. With the addition of hydrogen, the XPS spectra showed the peak at 396.5 eV, originating from the N bonded to the Si ([N-Si] peak), 99.0 and 99.6 eV from the Si bonded to the Si ([Si-Si] peaks), and 101.5 eV from the Si bonded to the N ([Si-N] peak). These indicate that small addition of hydrogen gas to the nitrogen gas do not enhance the nitrogen decomposition and consequently surface nitridation. However, with increasing

hydrogen addition, the [N-Si] and [Si-N] peaks increased and the [Si-Si] peaks decreased and totally disappeared.

These indicate that [Si-O] peaks increased and the intensities became much larger when the amounts of an increase in the addition of hydrogen gas enhances the nitrogen decomposition and thus enhances the surface nitridation of the thin films.

The intensities of [Si-O] peak increased with a higher NH_3 or a lower H_2 gas flow ratio. For SiO_x , the peak position is 102.7eV with $x < 2$ and 103.4eV with $x = 2$. It can be seen that when the SiN_x film is completely oxidized, it became a SiO_2 film and it could exist in the form of SiON in the process.

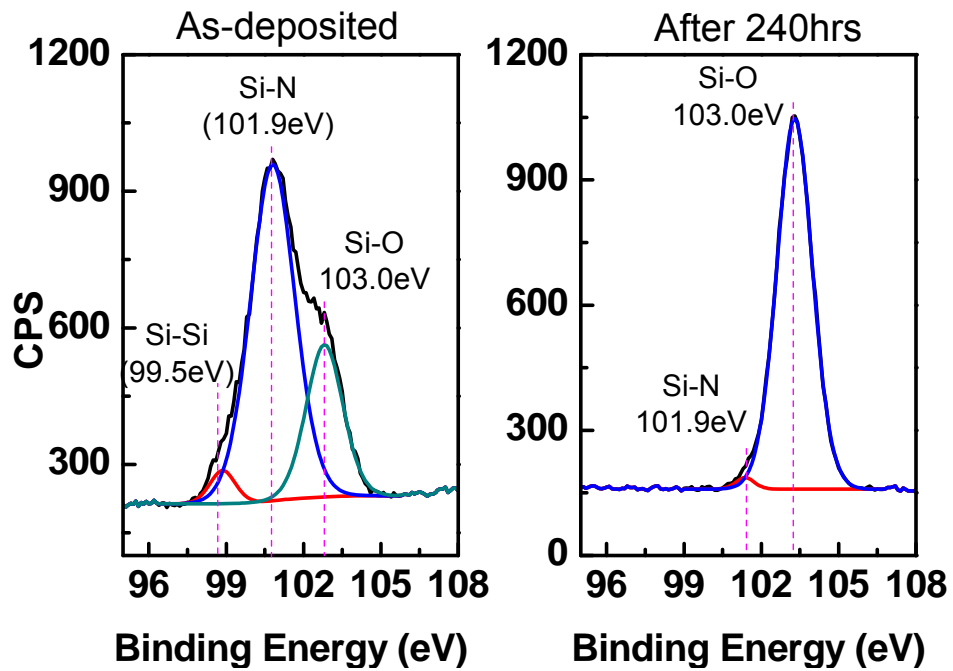


Fig. 4.6. Binding energy of Si2p by XPS before and after oxidizing in the humidity chamber for 240hrs. $\text{NH}_3/\text{total gas flow ratio} = 0.034$.

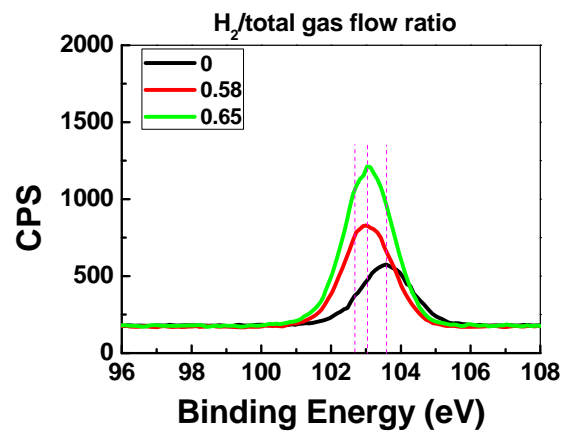
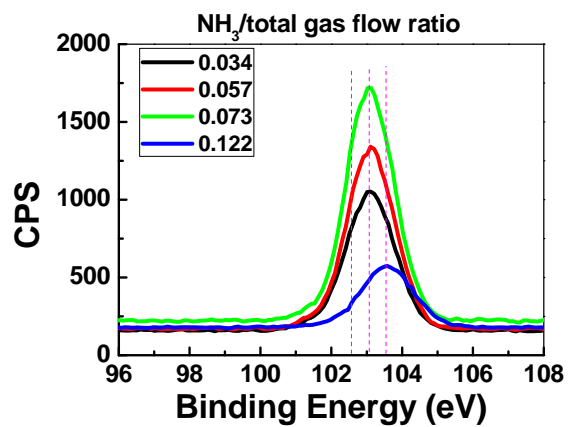
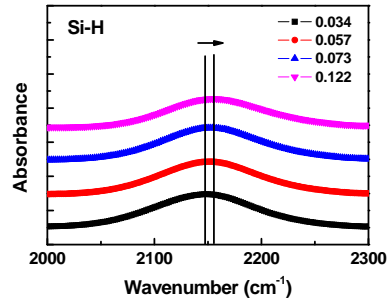
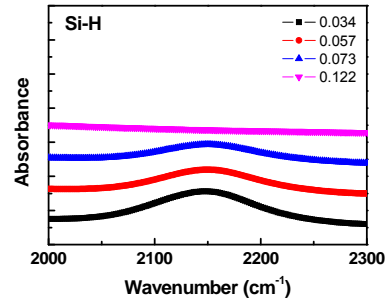


Fig. 4.7. Binding energy of Si2p by XPS after oxidizing in the humidity chamber for 240hrs

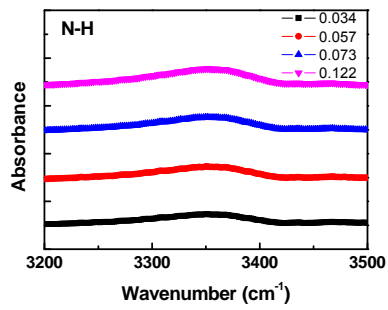
From the FT-IR and XPS results, it was found that the SiN_x film reacted with moisture and changed into a SiO_x film. The rate of oxidation reaction was different according to NH_3 and H_2 gas flow rate. Therefore, the [Si-H] and [N-H] bond structures before and after the oxidation test are shown in Figure 4.8, showing the different oxidation rate. Figure 4.8 (a) shows the [Si-H] bond structure according to the NH_3 gas flow rate. In Figure 4.8 (a), the peak intensities of [Si-H] are similar, but the peak position shifts from 2146.4 cm^{-1} to 2156.0 cm^{-1} . Figure (b) shows the peaks in the [Si-H] bond structure after the oxidation test for 240 hours. As the R_{NH_3} increases from 0.034 to 0.122, the intensity of the [Si-H] peak decreased. Especially, under the condition of $R_{\text{NH}_3} = 0.122$, the peak of the [Si-H] bond structure disappeared. On the other hand, the [N-H] bond showed an increase in NH_3 flow rate immediately after the deposition, but became smaller after oxidation evaluation and completely disappeared at $R_{\text{NH}_3} = 0.122$.



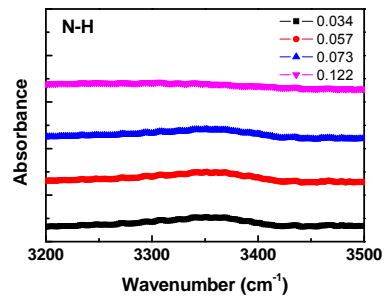
(a) As-deposited films



(b) After oxidation



(c) As-deposited films



(d) After oxidation

Fig. 4.8. Comparison of [Si-H] and [N-H] bonding peak position (FT-IR) of SiN_x films with NH_3 /total gas flow rate before and after oxidation.

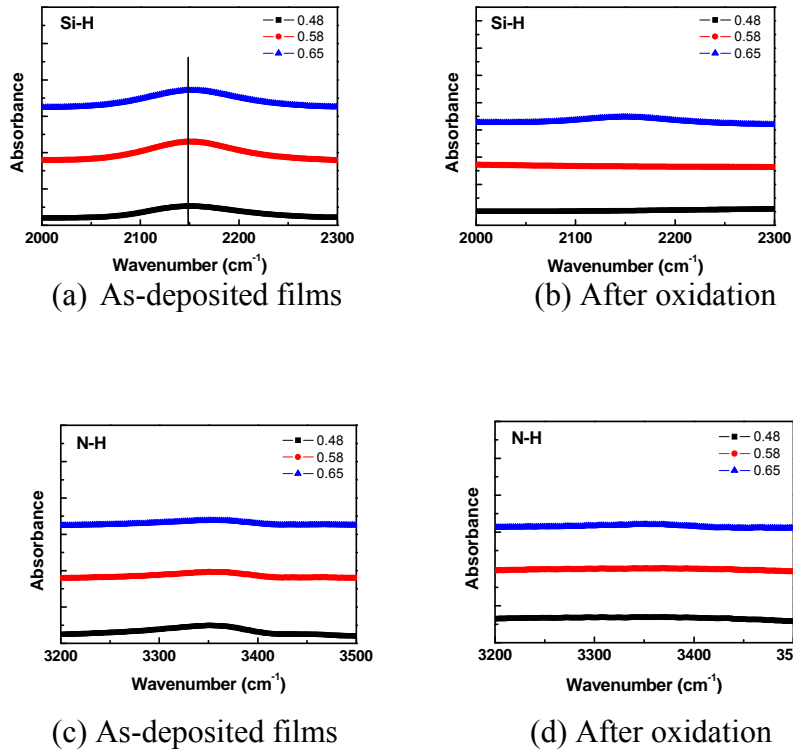


Fig. 4.9. Comparison of [Si-H] and [N-H] bonding peak position (FT-IR) of SiN_x films with H₂/total gas flow ratio before and after oxidation.

Fig. 4.9 shows the change of [Si-H] and [N-H] bond structure according to the H₂ gas flow ratio. As the H₂ gas flow rate increased, the [Si-H] bonds increased and [N-H] bonds decreased. After the oxidation test 240 hours, the [Si-H] bond completely disappeared below R_{H2} = 0.56, The [N-H] bond in the all samples disappeared. This means that the oxidation rate was much faster under conditions where there were many [N-H] bond structures.

Fig. 4.10 shows the N1s spectra (XPS) for the film of as-deposited films. Fig. 4.10 (a) and (b) showed the results for NH₃ and H₂ split, respectively. When the NH₃ flow rate increased, the N1s binding energy was shifted toward the higher energy side, while the binding energy peak position decreased when the H₂ flow rate was increased. The higher binding energy component of N1s corresponding to more [N-H] bonds. Thus, the binding energy of N1s toward the higher direction represented that the [N-H] bond was increased rather than the [Si-N] bond. (J. Mat. Sci. 32, 157, 1997)

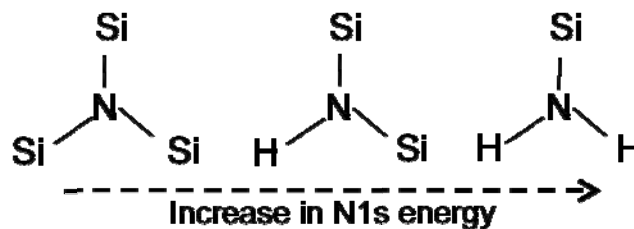


Figure. 4.11 and Table 4.5 showed the morphology and surface roughness (RMS) measured by atomic force microscopy (AFM).

We found that the roughness increased with increasing NH₃/total gas flow ratio. The surface roughnesses of the as-deposited films with NH₃/total gas flow ratio=0.034 and 0.073 were 0.80nm and 1.14nm, respectively. The oxidation

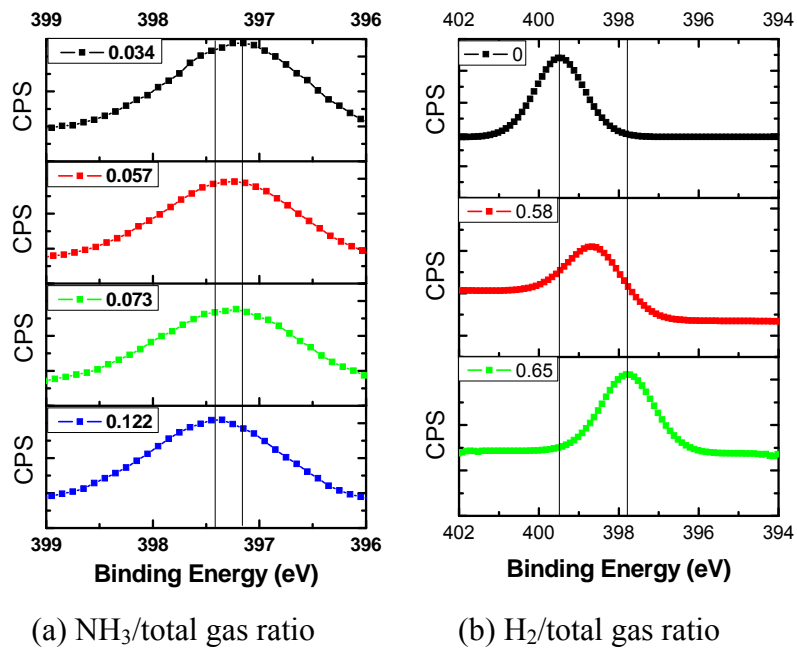


Fig. 4.10. N1s spectra (XPS) of as-deposited SiN_x films.

process enhanced the surface roughness from 0.80nm and 1.14nm to 1.30nm and 1.53nm, respectively. These results were consistent with the morphology taken by TEM. This was explained by the emission of N_2 and NH_3 by the oxidation of SiN_x film reacted with water vapor and oxygen.

The surface roughness became larger with increasing the amounts of hydrogen flow during deposition process. This can be explained by the excessive H radicals, leading to etch the film. No change in the roughness of SiN_x film deposited without the addition of hydrogen gas was found.

The increase of the NH_3 flow rate leads to a deposition rate decrease and the increase of the surface roughness due to the variation of the chemical [N-H] and [Si-H] bond concentrations. Moreover, the deposition rate decreases when the [N-H] bond concentrations increased which is correlated with higher NH_3 flows, [N-H] bonds are formed from NH_3 dissociation which happens at higher energy than [Si-H] bonds formed from SiH_4 dissociation. A high concentration of hydrogen and a high roughness can lead to lower refractive index due to hydrogen incorporation. The refractive index can be not only correlated with hydrogen concentration but also with SiN_x stoichiometry and films roughness [34].

AFM surface roughness measurements as a function of SiH_4/NH_3 flow ratio indicate a low RMS roughness for the low flow rate and a strong development in roughness for the films deposited at high flow rate. The silane partial pressure is a parameter that is related to the roughness development. The high surface roughness suggests the inclusion of gas phase generated dust particles. Possible reaction pathways for gas phase formation of dust involve neutral SiH_4 reacting with ionized clusters [34].

The surface roughness is related with the barrier performance. For the low

SiH₄/NH₃ flow rate, the measured WVTR is not dependent on the flow ratio, while for high flow rate, the WVTR remains small and then increased with increasing the high flow rate ratio.

This is consistent with the observed reduced mass density of the layers and a very high surface roughness as measured with AFM. While surface roughness is not necessarily related to the permeation rate, the increase in roughness is attributed to the inclusion of gas phase nucleated particles. Boundaries of such particles embedded in the film matrix can act as permeation pathways [102].

The cross-section images of film R=0.057 taken by TEM are shown in Fig.4.12. This indicates the morphology change as a function of storage time. Figure 4.12(a) and (b) show top and bottom images of the as-deposited film, exhibiting the morphologies of typical amorphous SiN_x films.

However, the top and bottom images after the storage in the humidity chamber, shown in Fig. 4.12(c) and (d), were different from each other.

The SiN_x barrier approximately 70-80nm from the top surface was found to be porous due to corrosion. This thickness corresponds to the depth calculated from the saturation concentration of nitrogen by AES (88nm). Some white areas with elliptical shapes could be found below 80nm. These are SiO_x grains caused by the oxidation of SiN_x film. It is believed that these grains grew as the oxidation proceeded and then combined together to form pure SiO_x film.

The surface roughness of the film increased in the well-oxidized samples.

We could not find any void and columnar structure in the cross-section images of as-deposited films. The TEM images suggested that the oxidation occurred in a layer-by-layer from the film surface. In Fig. 4.12 (c), we could see the white circle and oval shape. These are thought that H₂O molecule penetrates into the film

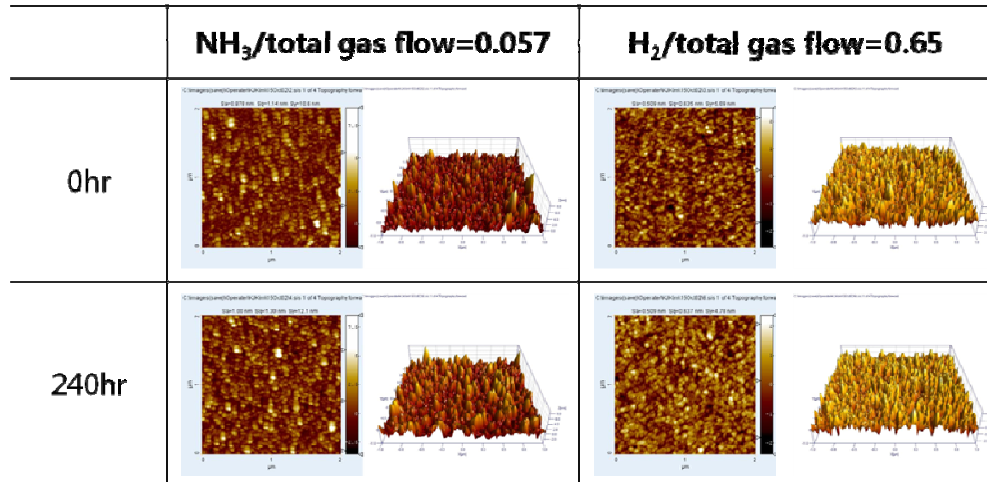


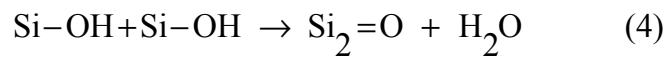
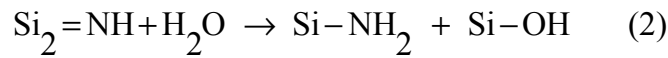
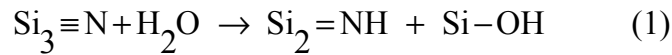
Fig. 4.11. The changes in morphology and surface roughness as a function of the amounts of NH₃ and H₂ addition to the reactant gases, before and after storing in the humidity chamber.

	NH ₃ /total gas =0.057		H ₂ /total gas =0.65	
	Sa(nm)	Sq(nm)	Sa(nm)	Sq(nm)
0hr	0.88	1.14	0.51	0.64
240hr	1.20	1.53	0.51	0.64

Table. 4.5. The morphology and roughness changes measured by AFM before and after duration in the humidity chamber

defect and induce more oxidation near the void in the film, implying more [N-H] bond near the void in the film.

The oxidation process was conducted as following steps. There are [Si-H], [N-H] and [Si-N] bonds. As shown before, we found the change of bond peak position and intensity with FT-IR and XPS analysis. Therefore, the oxidation reaction seem to proceed by the following mechanism.



From the above data, the [Si-H] & [N-H] bonding are crucial to the oxidation process. But the oxidation did not depend on [Si-H] because [Si-H] bonding ratio was similar or slightly decreased with increasing NH_3 gas ratio. Therefore, [N-H] groups are reactive sites. The hydrogen molecules were removed by NH_3 or H_2O , leading to the porous and rough surface.

Fig. 4.13 showed that the oxidation rate of SiN_x film with a larger [Si-H] bonding ratio is higher because the [Si-H] bond reacts with H_2O and forms the [Si-O-Si] bond. While some researchers reported that the [N-H] bond react with H_2O , forming the [Si-O-Si] bond. As summarized in table. 4.6, some papers about the oxidation mechanism of SiN_x thin films have been reported. But most studies have focused on the interpretation and analysis about the bond structure reacting with water vapor. These results suggest that the oxidation mechanism can be different according to the experiment method and process window.

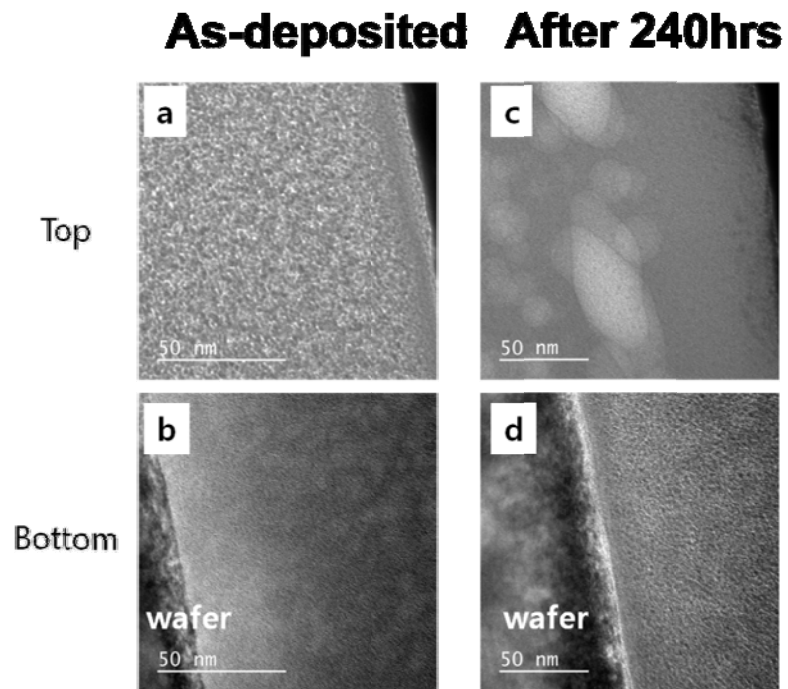


Fig. 4.12. The cross-section images of SiN_x films by TEM; (a) & (b) as-deposited film and (c) & (d) after storing in the condition of 85°C and 85% RH for 240hrs. (a) & (c) are top images of the films and (b) & (d) bottom images of the films.

But it is clear that the SiN_x thin film can be oxidized and accelerated under the condition of high humidity and temperature, whether it reacts with [Si-H] or [N-H] bond. In other words, only one bond do not participate in the oxidation process but all bonds in the SiN_x film can be broken by water molecule. The best moisture-resistant property in terms of stability of the SiN_x film was found in the film with lower ratio of SiH_4 to NH_3 . For longer exposure time, the [N-H₂] peak was increased and the [Si-O] and [Si-Si] peak became sharper [18].

The ease of oxidation is proportional to the amount of $(\text{Si-H}_2)_n$ chains around the voids. Films with a large amount of [N-H] bonds have few voids. SiN_x films with a larger concentration of [N-H] bonds and a smaller concentration of [Si-H] bonds are not easily oxidized [131].

In this study, one of the interesting things was the changes of films stress, optical constant and morphology during the oxidation process of SiN_x thin film.

As seen before, the oxidized SiN_x films show the stress change from compressive to tensile and the reduction of refractive index to 1.44 of SiO_x thin films. also, the surface roughness measured by AFM increased and the cross-section image represented that the films changed to be rough and porous.

The thin film stress can be affected by void and hydrogen in the film. Fig. 4.14 shows the distance of molecules and void formation due to the hydrogen depoletion. The nitrogen and hydrogen can form N_2 , H_2 and NH_3 when react with H_2O and then go out from the film, being far away from each molecule and forming voids. The larger space can induce the decrease of compressive stress and finally change the stress compressive to tensile.

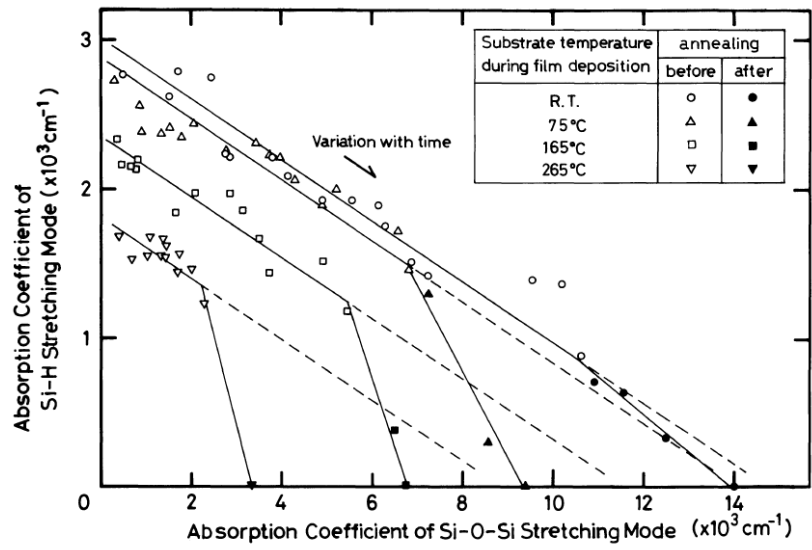


Fig. 9. Relationship between the Si-O-Si mode and Si-H mode absorption coefficients with time.

Fig. 4.13. Relationship between the [Si-O-Si] and [Si-H] mode absorption coefficient with time [18, 131]

#	Dep. condition	Oxidation condition	Summary	Ref.
2	SiH ₄ /NH ₃ =0.77~2.0, 0.8torr, 180 °C	121 °C/103kPa(PCT), 85 °C/85%	- The best moisture-resistant property in terms of stability of the SiN _x film was found in the film with lower ratio of SiH ₄ to NH ₃	Thin Solid Films, 333, 71 (1998)
3	SiH ₄ =2~10, N ₂ =50, R.T. ~ 260 °C	Air	- The oxidation proportional to the amount of (Si-H ₂) _n chains around the voids. A larger concentration of N-H bonds and a smaller concentration of Si-H bonds are not easily oxidized.	Jpn. J. Appl. Phys. 27, 1401 (1988)
4	SiH ₄ =1~4, NH ₃ =15~120, 1~10Pa, 300~500 °C	air	- NH ₃ /SiH ₄ >30 : no increase of the N content, porous, oxidation - NH ₃ /SiH ₄ <30 : no voids, low H content, low N-H, no oxidation	J. Appl. Phys., 93, 2618 (2003)
5	300 °C	121 °C/2atm(PCT)	- The N-H is an indicator for moisture resistance than refractive index	CS Mantech confer. 2014.
6	SiH ₄ =150~390, NH ₃ =0~6450, 1.2~1.7torr, 380 °C	640torr, 00~1000 °C	- N-H bond plays a major role in the oxidation resistance	Appl. Surf. Sci., 39, 25 (1989)
7	SiH ₄ =3, NH ₃ =58, 0.4torr, 20~250 °C	Air	- The H ₂ O molecules from air are responsible for oxidation with both the Si-N-Si and Si-N-H bonds	Appl. Phys. Lett, 65, 2229 (1994)
8	SiH ₄ =5, NH ₃ =50, 0.75torr, 175 °C	air, 1100 °C	- The removal of N at low T(<500 °C) is due to the dissociation of N-H bonds and the removal at higher T is a result of the oxidation process.	J. Alloys and Compounds, 437, 332 (2007)

Table. 4.6. Literature survey on the oxidation of SiN_x films

The thin film stress generation is due to the hydrogen depletion and micro voids shrinkage. Hydrogen is the major source of compressive stress in silicon nitride [104, 114]. After oxidation, most of hydrogen are removed and some small voids are formed. The molecules or atoms tend to move in order to reduce the spacing and this shrinkage process induces a tensile stress.

The in-depth composition variations of SiN_x barrier films oxidized by high temperature and humidity environment were analyzed by Auger electron spectroscopy as shown in Fig. 4.15.

One can find that there was no nitrogen at the surface because all samples were oxidized. But nitrogen started to appear below the surface and the concentration was saturated after a certain depth, which varies for each sample. The time of saturation gives information about the oxidation depth, which was larger for higher storage in the condition of 85 °C/85% RH for 240 hrs.

The depth profile of oxidized SiN_x films with increasing NH₃ gas flow rate are shown in Fig. 4.15. As the oxidation progressed, the N component in the SiN_x film escaped, so the oxide thickness was analyzed by the change of the nitrogen component from the surface to the depth direction. The oxidation thickness was compared with the time when the concentration of the nitrogen component rapidly increased. As shown in the figure, it was found that the oxidation rate was fast and thick as the NH₃ ratio was increased. We found that the oxidation rate was much more faster when more NH₃ and less H₂ gas added to the deposition process.

The WVTR is related to the diffusion coefficient as follows:

$$WVTR = \frac{D}{\text{thickness} \times n_0}$$

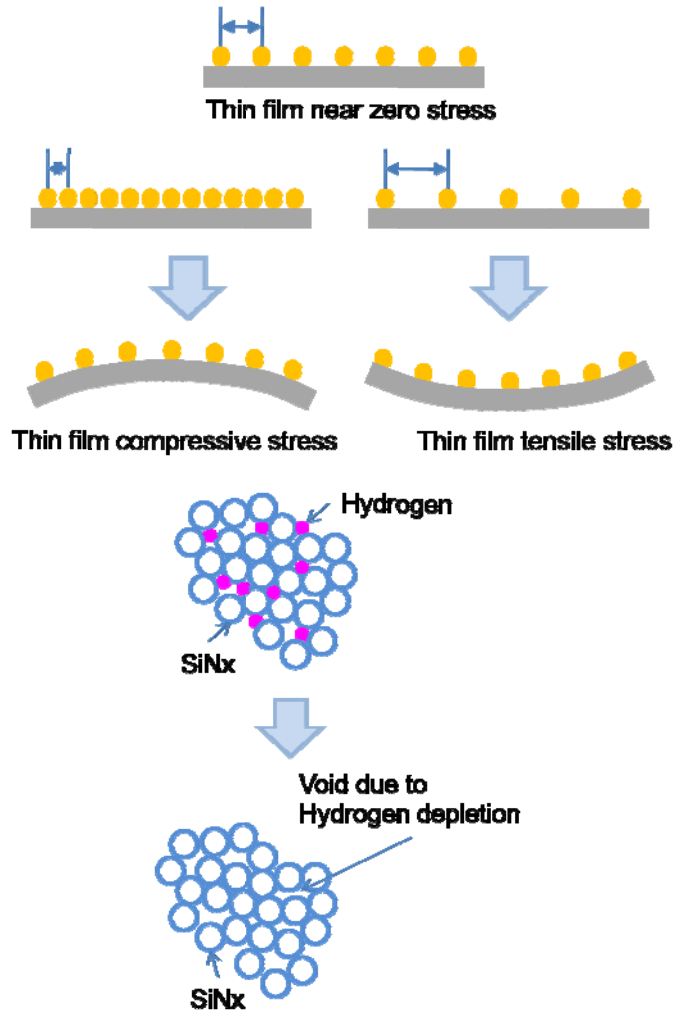


Fig. 4.14. The influence of thin film stress on the curvature of the deposition substrate.

Where D is the diffusion coefficient and n_0 is the surface concentration ($=3\text{g/cm}^3$). With MOCON test, the WVTR of at a thickness of 200 nm under the condition of $R_{\text{NH}_3} = 0.073$ was $5 * 10^{-2} \text{ g/m}^2\text{-day}$. However, the WVTR of 500nm-thick film measured by HTO method $5*10^{-5}\text{g/m}^2\text{-day}$. The diffusion coefficient of $R_{\text{NH}_3}=0.073$ was calculated to $9.645*10^{-15}\text{cm}^2/\text{s}$.

The oxidation thickness can be calculated by a Deal-Grove model. The original Deal-Grove model is a model for the oxidation behavior of pure Si at temperatures above 700°C . However, according to the report (J. of Vac. Sci. & Tech. A33, 031513 (2015)), it was possible to utilize the change of the physical properties of the barrier film and the prediction of the oxidation thickness in a high temperature and high humidity atmosphere. The Deal-Grove model for the thick film is as follows.

$$\text{Oxidation thickness} = \sqrt{B \times \text{time}}$$

$$B = \frac{2DC^*}{N}$$

Here, N is the number of oxidant molecules ($=4.6*10^{22} /\text{cm}^3$), and C^* is the equilibrium concentration of the oxidants ($1.60*10^{22} /\text{cm}^3$).

The oxidized thickness of the $R_{\text{NH}_3} = 0.073$ film calculated from the composition profile measured with AES for 240hours was about 84.8nm. The oxidation thickness of the $R_{\text{NH}_3} = 0.073$ film calculated using the Deal-Grove model was about 76.2nm. Based on this, it is estimated that the oxidation thickness of about 500nm is about 110nm.

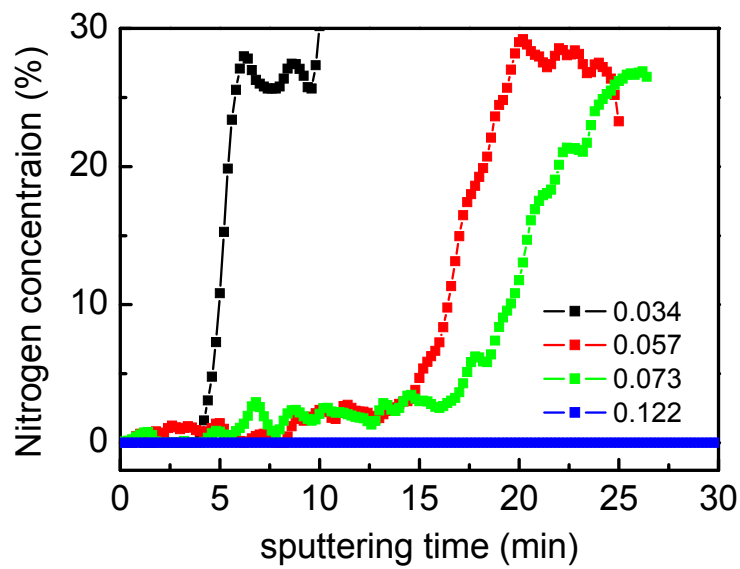


Fig.4.15. The composition profiles of SiN_x films by Auger Electron Spectroscopy as a function of NH₃ gas flow rates. The etch rate was 5.3nm/min

4.1.4 Summary

Silicon nitride thin film barriers deposited by the low temperature PECVD varying with NH_3 or H_2 gas flow rate. We investigated the oxidation of silicon nitride thin film barriers by measuring the changes in the film properties such as film stress and refractive index before and after the storage in chamber with the condition of high temperature and high humidity

With increasing NH_3 gas ratio, the refractive index decreased from 1.93 to 1.81 and the film density reduced from 1.996 to 1.895. On the other hand, with increasing H_2 gas ratio, the refractive index increased from 1.80 to 1.90 and the film density increased from 1.852 to 1.922.

There were no peaks related to the oxygen bonding. The FT-IR spectra of as-deposited films represented that there were no bonding peaks including oxygen bond. The [Si-H] peak intensity decreased and the [N-H] intensity increased with a higher NH_3 gas ratio. The [Si-H] peak position of as-deposited films with a larger NH_3 gas ratio shifted to a longer wavenumber, indicating N-rich SiN_x film. The [Si-H] peak intensities increased with increasing H_2 gas ratio, while [N-H] peaks decreased. The higher binding energy component of N1s spectrum (XPS) of as-deposited films with a higher NH_3 gas ratio corresponding to more N-H bonds.

Both the stress and the refractive index of all samples decreased with a duration time in the $85^\circ\text{C}/85\text{RH}$ chamber. Those values changed largely with a larger NH_3 or a less H_2 gas flow rate during deposition process. With $R_{\text{NH}_3}=0.073$ and 0.122 , the refractive index decreased to 1.44 after 240hr, which is similar to the value of SiO_x thin film. FT-IR spectra of SiN_x films after 240hrs in the condition of $85^\circ\text{C}/85\% \text{RH}$ showed that the peak intensities of [Si-N], [Si-H], and [N-H] decreased while the

[Si-O] intensity increased drastically with a higher NH_3 or lower H_2 gas ratio. the [N-H] peak intensity of as-deposited films was enhanced with increasing NH_3 gas flow rate, while the intensity after oxidation was more decreased in the films with a larger [N-H] peak.

The surface roughness by AFM was increased in the well-oxidized film. Cross-section transmission electron microscopy showed that the oxidation reaction occurred layer-by layer from the film surface.

The [Si-H] & [N-H] bonding were crucial to the oxidation process. By comparing [Si-H] bonding (FT-IR) and N1s spectrum (XPS) of the films before and after the oxidation represented that the [N-H] groups were a main reactive sites, not the [Si-H].

The WVTR of 0.5 μm -thick film with $R_{\text{NH}_3}=0.073$ was $5 \times 10^{-5} \text{g/m}^2\text{-day}$, resulting in the diffusion coefficient of $9.645 \times 10^{-15} \text{cm}^2/\text{s}$. After 240hrs in the $85^\circ\text{C}/85\% \text{RH}$ chamber, the oxidation thickness measured AES data was about 84.8nm and the one calculated from the Deal-Grove model was 76.2nm, being predicted 110nm after 500hrs.

4.2 The effect of Thin Film Structure on the Optical Property of TOLEDs

4.2.1 Introduction

Conventionally, an OLED is fabricated on a glass substrate. Organic thin-films are sandwiched by a transparent indium tin oxide (ITO) anode and a reflective metal cathode, which is also called bottom emission OLED, as shown in Figure 4.211(a). By applying a voltage (typically <10 V) to such a device, carriers are injected into the device and recombine to give light. Photons generated from the organic layers propagate through the glass substrate and radiate out to the air for light emission. Emission wavelength of OLED is determined by the organic material, as well as the device configuration. Because the conductivity of organic material is quite low, layer thickness of total organic thin films was limited to 100 to 200 nm for driving an OLED with reasonably low voltage (ex: <10 V). Considering the refractive index (n) of ITO and organic materials (typically 1.6 to 2.2 at visible region), an OLED can be regarded as a microcavity with the effective optical length comparable to the visible wavelength (from 380 to 780 nm), which results in a strong interference effect within such a device (including ITO anode, organic thin films, and reflective cathode). With fixed organic materials, the optical intensity of OLEDs can be varied with different layer thicknesses, depending on constructive or destructive interferences. Such an interference effect is sensitive to the viewing angle and wavelength. For display application, emission from normal direction may be most important. On the other hand, one may need to optimize the total flux of light emission. Besides, the optimized cavity structure for a certain wavelength (ex: 600

nm for red light emission) may be not the best choice for another wavelength (ex: 470 nm for blue one), which results in difficulties in designing a broadband emission, such as white OLED. Optical loss in ITO and organic layers was typically called organic mode. Light may also couple to surface plasmon (SP) mode of metal cathode which relaxes the energy nonradiatively. Besides, as other EL devices, light was waveguided in the substrate, and it was called substrate mode. Thickness of glass substrate is typically several hundreds of μm for providing enough mechanical strength. Refractive index of glass substrate is about 1.5, which is smaller than organic and ITO, but larger than the air ($n = 1$). An alternative device configuration to completely remove the substrate mode is to use a reflective anode, and a transparent (or semi-transparent) cathode, so that the light emits from the cathode side to the air, which is called top-emission OLED, as shown in Figure 4.16(b).

Fig. 4.16 (c) and (d) represent a transparent and tandem structure designing based on the Fig. 4.16 (a) and (b). The transparent OLED includes anode and cathode consisting of high transparent thin metal film. The purpose of tandem structure is the verification of the efficiency and lifetime of OLED but the driving voltage increases. In this way, the optical property of OLED can be designed for various types because it consists of organic thin films emitting light [115].

4.2.2. Microcavity and Fabry-Perot cavity

The light is initially generated as a result of recombination of electrons and holes in the OLED molecules, and then takes a path through the OLED and is either emitted or lost. Outcoupling from the thin films is also an issue of critical importance. The light is emitted from within the stack, generally adjacent to a

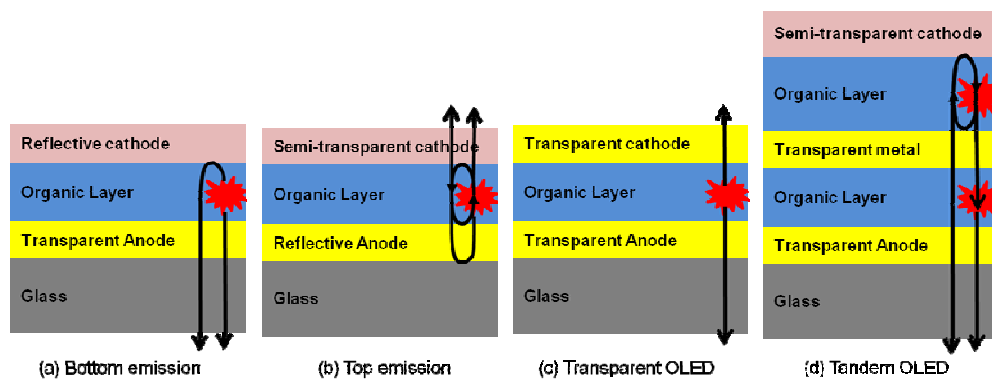


Fig. 4.16. OLEDs with different device configuration

metallic cathode (for bottom emitting devices) which reflects some of the light back toward the substrate. As a result of this, interference can occur, influencing the emission, particularly in the forward direction. As the OLED is a broad band emitter, this will have different effects on different regions of the emission spectrum, depending on the particular device architecture. Additionally any refractive index mismatch between the OLED layers and the substrate can further exasperate the problem. Emitted light may also become locked to surface plasmons, forming polaritons which stop the outcoupling of this light. Increasing the light emission : spectral narrowing, spectral shift of the emitted light with a stronger cavity effect, the optical intensity depends on more on the viewing angle and the emission wavelength. A planar microcavity structure consists of a reflective anode, a semi-transparent cathode, and organic layers sandwiched in between. The anode and the cathode are parallel mirrors and they form a Fabry-Pérot resonator [116].

The emission efficiency is affected by the recombination zone. The light extraction efficiency of an organic light emitting devices is a strong function of device geometry. The substrate guided mode of an OLED structure strongly depends on the optical cavity length of the device due to the weak cavity effect, and the substrate extraction efficiency varies from 22% to 55% depending on the device geometry.

The reflectance and transmittance characteristics of optical thin film are strongly dependent on the wavelength. The film and substrate materials are very effective on the reflectance and transmittance characteristics of the optical thin films. It is also found that the reflectance and transmittance characteristics are greatly affected by film thickness [117].

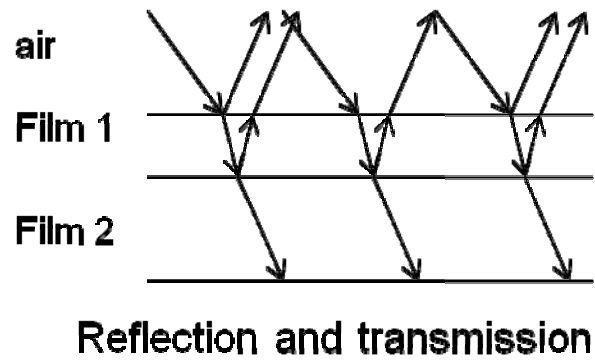


Fig. 4.17. Reflection and transmission of light ray in optical thin film

To perform the functions for which they are designed, thin films must have the proper thickness, composition, roughness, and other characteristics important to the particular application. That's why it is important to know the thickness, optical constants, optical and absorption properties as a function of wavelength. The influence of film's materials, thickness and the substrate on the optical properties of the optical thin film is so high that an extensive study and analysis is still a necessary research issue to understand, control, optimize and develop them for particular application.

The optimized device structure for one color may be not suitable for other colors. One may need three different device structures to optimize the optical characteristics. Because of the refractive index differences, there are some reflections at the interfaces.

Whenever electromagnetic wave such as light crosses the interface between two different materials, the fraction of light is reflected by the inner surface while some amount of electromagnetic wave is refracted through the inner surface and finally transmitted.

The total amount of reflectance of the film has been derived as follows [118-122] ;

$$R = \frac{P^2 + Q^2 + 2PQ\cos R}{1 + P^2Q^2 + 2PQ\cos R}$$

The total amount of transmittance of the film has been derived as

$$T = \frac{16n_0^2 n_f^2 n_s}{1 + P^2Q^2 + 2PQ\cos R}$$

Where,

$$P = \frac{n_0 - n_f}{n_0 + n_f}, \quad Q = \frac{n_f - n_s}{n_f + n_s}, \quad R = \frac{4\pi}{\lambda} n_f d_f$$

n_0, n_f, n_s : the refractive indices of surrounding medium (air), film1, film2

d_f : the film1 thickness

λ : the wavelength of spectrum

The magnitude of reflectance and transmittance of optical thin film vary periodically with wavelengths. Multiple oscillations occur on the reflectance and transmittance curves due to interferences among multiple reflected waves. As the wavelength increases, oscillation period of these characteristics changes/increases. The reflectance and transmittance characteristics of optical thin film are greatly affected by film thickness. Also the amount of thickness effect on the reflectance-transmittance characteristics is significantly different in different film materials. Thus the reflectance and transmittance characteristics of multilayer thin film are strongly dependent on the wavelength of electromagnetic spectra.

By choosing appropriate film material, the desired R and T characteristics of thin film can be obtained.

The outer layer in the bottom-emitting OLED corresponds to the thick substrate, which should be treated as optically incoherent because its thickness (~1mm) is much larger than the coherent length of the OLED light emission. Because the thick substrate is incoherent, the change in the substrate thickness will not affect the electric field intensities. Instead, the incoherent multiple reflections inside the thick substrate cause the reduction of the optical power extracted into air.

Although the application of the Fabry-Perot formalation is only limited to the radiation mode, the Fabry-Perot formalation is still very useful and widely used modeling method to opimize the multilayer structure of OLEDs, where only the consideration of the radiation mode is sufficient to maximize the output intensity under the micro-cavity effect [123-125].

Typically, a top-emitting OLED consists of a reflective anode, a few organic layers, and a transparent or semi-transparent cathode for out-coupling light. The strong Fabry-Perot interference in the microcavity formed with the opaque anode and the semi-transparent cathode, combined with a thin dielectric layer to modulate the cathode reflectivity, has been shown to achieve a significant enhancement in light output intensity. In such a structure, the output intensity is controlled by the following factors: 1) the emission characteristics of the organic materials; 2) the wide-angle interference, which results from the interference between the direct emission and the emission reflected from the opaque anode once; and 3) the multiple beam interference, which results from the interference between the back-and-forth-propagating beams within the microcavity. The wide-angle interference is determined only by the dipole position and the anode reflectivity, while the multibeam interference is determined by the cavity optical length, anode and cathode reflectivity.

The emission spectrum in the normal direction of a Fabry-Pero cavity can be described by the following equation [126, 127]:

The emission intensity in the normal direction

$$E_{out}(\lambda) \propto \frac{T_2 \times \left[1 + R_1 + 2\sqrt{R_1} \cos\left(\frac{4\pi x}{\lambda}\right) \right]}{1 + R_1 R_2 - 2\sqrt{R_1 R_2} \cos\left(\frac{4\pi L}{\lambda}\right)}$$

x : the effective distance between recombination zone and the cathode

R_1 : the reflectivity of the cathode

R_2 : the effective reflectivity of the anode

T_2 : the effective transmittivity of the anode

L : the total optical length

- L & x : no intensity change, max. peak wavelength shift, frequency change

- R_1, R_2, T_2 : no peak shift, no frequency change, intensity change

Therefore, we can estimate the emission intensity from the reflectance calculation of multilayers.

Recently, a few papers have been reported that the transmittance of thin film encapsulation was a major factor for affecting the optical properties of OLED, resulting in the decrease of light extraction.

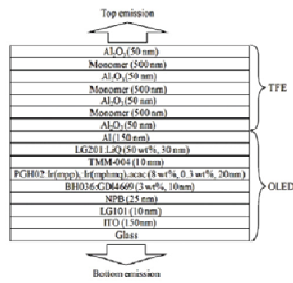
This study suggests that the optical properties of TOLED can be affected by the TFE structures. Not only the optical properties of thin films such as refractive index, extinction coefficient, and transmittance, but also the number of layers and the thickness of each layer play a major role in designing of thin film encapsulation structure [128].

The authors studied the effects of thin film barrier on the barrier performance and optical property, which can be adjusted by designing the film thickness by ALD and ML. The light extraction with a maximum transmittance of cathode did not show the peak efficiency. They demonstrated that the maximum light extraction could be obtained, depending on the interference effect affected by the refractive index of thin films. In conclusion, they insisted that the light extraction can be optimized by controlling the thickness, refractive index and structure of thin film

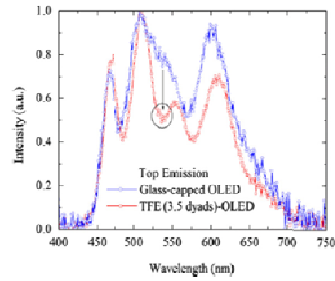
encapsulation.

In Fig. 4. 18, the optical and barrier properties of thin-film encapsulations for top-emitting organic light-emitting diodes were investigated using TFEs fabricated by stacking multiple sets of inorganic-organic layers [129]. It was demonstrated that maximum light emission does not occur at the highest cathode transmittance, but rather, is dependent on the interplay between different interference effects that are governed by the refractive index of the capping layer. This shift of the spectral characteristic as a function of both TFE thickness and refractive index can also be simulated by the optical model. By varying the TFE nanolaminate layer stacking structure, the interplay between the optical interferences can be controlled. It was found that, by fine-tuning the optical thickness of the TFE, the light extraction properties could be improved. Careful tuning of these parameters and the relative thickness of the inorganic-organic materials in the encapsulation layers are important considerations for the optimization of the barrier protection and the transmittance for top-emission organic electronics. The electroluminescence spectra exhibit a different functional dependence on the TFE structure. The EL spectra slightly depend on the detailed optical architecture.

The authors studied the optical property and barrier performance of thin film encapsulation for TOLED (top emitting organic light emitting diode). From Fig. 4.18, they measured the variation of transmittance of thin film encapsulation consisting of multilayers, comparing to the TOLED covered by the glass. The transmittance decreased at a certain wavelength with increasing film layers, showing a dip valley. These sharp valley was caused by the interference of multilayered structure. The multilayer structure showed the interference effect because the thin film consisting of multilayer have different refractive indices.



Layer structure



Glass encap. vs. TFE

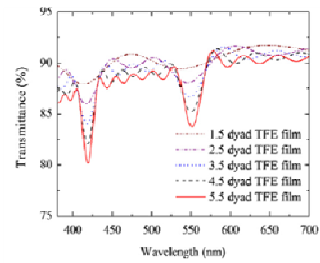


Fig. 6. Simulation results of transmittance of TFE films for different TFE structures

Transmittance vs. layers

Fig. 4.18. The effect of the TFE structure on the optical property of TOLEDs [129].

The thickness and layer have to be increased to improve the barrier property while the optical property can be deteriorated by the thin film structure. Therefore, the authors suggested two thin film encapsulation structures for improving both barrier performance and optical property. And they insisted that the interference effect can be decreased by reducing the refractive index difference between layers.

They investigated the optical and barrier properties of thin-film encapsulations for transparent organic light-emitting diodes. To improve the barrier property of OLEDs, the number of dyads and the thickness of polymer layer in the TFE structure are required to be increased. It is, however, demonstrated that a sharp dip appears in the transmittance of TFE films due to the interference of light caused by organic/inorganic multi-layered configuration, resulting in a dip in the top emission spectrum of OLEDs. Due to the organic/inorganic multi-layered configuration with different refractive index, however, the TFE structure inevitably brings in the interference of light. Consequently, the OLED light emitted through the TFE layer may be different from that through the conventional glass encapsulation.

The number of dyads and the thickness of the polymer layer are desired to be reduced. However, this would degrade the gas barrier property of OLEDs. To satisfy both optical and barrier properties, we can consider two different TFE structures. One structure can have the larger number of dyads but smaller thickness of the polymer layer. The other structure can have the smaller number of dyads but thicker polymer layer. They suggested that the latter configuration is more preferable within the frame of mass production and transmittance. If the difference of refractive index between the inorganic and organic layers in TFE films is small, the optical interference effect of TFE films can be suppressed. Therefore, the development of organic materials with the same refractive index as the inorganic

layer might be the way to achieve.

The researchers [130] investigated that the transmittance decreased with increasing the number of thin film for encapsulation. They improved the efficiency by controlling the refractive index. It was reported that they enhanced the optical transmittance of a multilayer barrier film by inserting a refractive index grading layer. To eliminate the Fresnel reflection while maintaining high transmittance, the optimized design of grading structures with the RIGL was conducted using an optical simulator. we achieved averaged transmittance in the visible wavelength region by 89.6%. It is found that the optimized grading structure inserting the multilayer barrier film has a higher optical transmittance (89.6%) in the visible region than that of a no grading sample (82.6%). Furthermore, luminance is enhanced by 14.5% (from 10 190 to 11 670 cd/m^2 at 30 mA/cm^2) when the grading structure is applied to organic light-emitting diodes. Finally, the results offer new opportunities in development of multilayer barrier films The transmission intensity was decrease when the thin film encapsulation formed on the TOLED. The transmittance of thin film is determined by the transmittance, absorption and reflection of the film. In this study, we investigated the effect of thin film transmittance on absorption and reflection. The effect of light reflection on the structure, thickness and refractive index of thin film encapsulation was analyzed. As the thickness of the thin film barrier decreases, the influence on the optical characteristics was confirmed by calculation of multilayer reflection values. Finally, the effect of the thin film on the optical properties of the device, when the refractive index of the film changes due to oxidation, was analyzed.

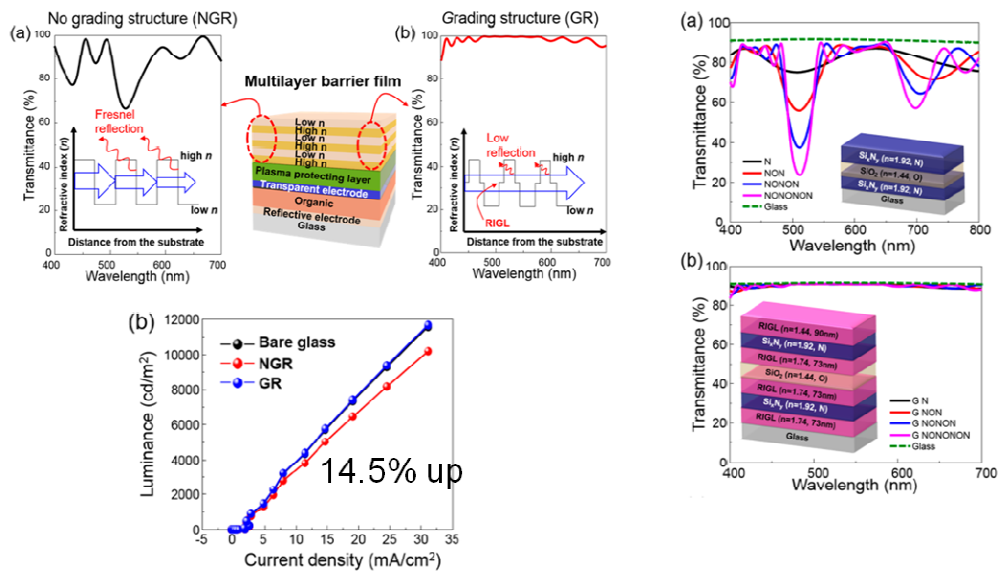


Fig. 4.19. The optical transmittance and luminance with varying the structure of thin film encapsulation [130].

4.2.3. The effect of thin film encapsulation on the optical property of OLEDs

As explained before, the TOLED uses the microcavity structure and the efficiency can be maximized by optimizing the thickness and refractive index of thin films. The thin film encapsulation can have an effect on the optical property of TOLED because it consists of thin films and affect on the cavity structure. To investigate the effect of thin film encapsulation on the light extraction of TOLED, we designed the film structure as follows.

As shown Fig. 4.20, we deposited the thin film encapsulation with multi-layers on the semi-transparent cathode. The most effective layers on the light extraction are the first and the second layers on the cathode because the layers are close to the emission zone of organic layers. Therefore, we controlled the thickness and refractive index of those two layers. The first layer have a high refractive index and the second one have a low refractive index.

The lower refractive index of the second layer is better, but we used SiO_x thin films with the refractive index of 1.46 by PECVD. Fig. 4.21 showed the transmittance and extinction coefficient as a function of the refractive index of the first SiN_x layer deposited by PECVD at 85°C . We found that the transmittance drastically decreased with increasing the refractive index. Especially, we could obtain the films with under the refractive index of 2.0 having transmittance of nearly 100%. But the films with above the refractive index of 2.3 showed the transmittance of 90% or less. Also, we confirmed that there is an inverse relationship between the transmittance and the extinction coefficient.

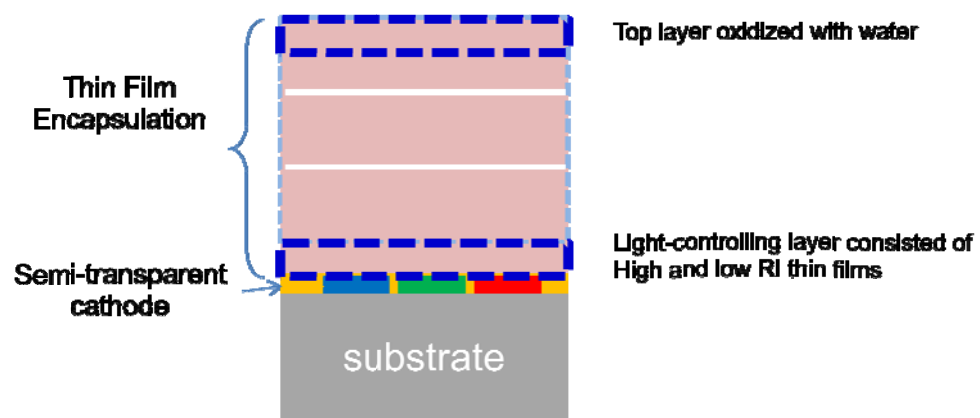


Fig. 4.20. Multi-layered TFE structure with barrier and buffer layers for the optical study

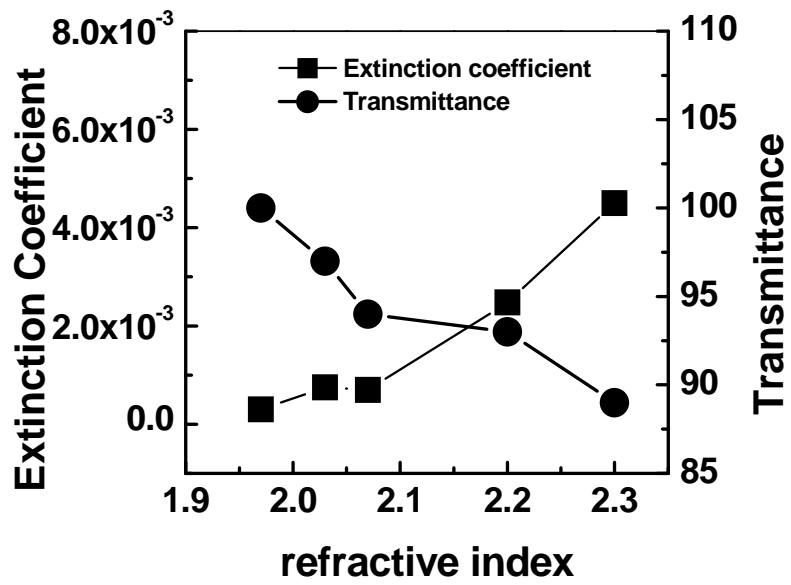


Fig. 4.21. The relationship between refractive index, extinction coefficient and transmission of silicon nitride thin films deposited at 85 °C by PECVD.

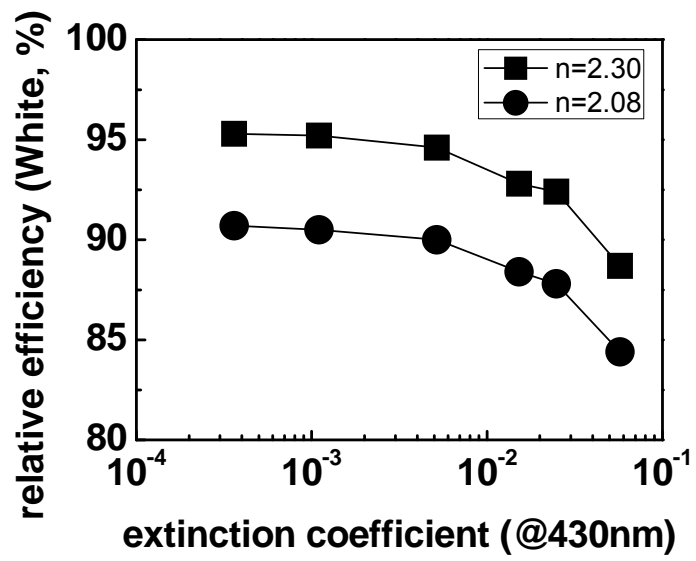


Fig. 4.22. The relationship between optical constants : refractive index vs. extinction coefficient vs. transmittance

The relative efficiency of white color with an extinction coefficient of 1st SiN_x thin films with a high refractive index was represented in Fig. 4.22. It was certain that the relative efficiency was high when the refractive index increased. We found that the relative efficiency decreased with increasing the extinction coefficient, regardless of the refractive index. This is due to the effect of transmittance decrease. We could also find that the efficiency began to decrease when the extinction coefficient was more than 10⁻³ and sharply decreased with above 10⁻².

In general, the thin film encapsulation is consisted of multilayers. This is because it is difficult to completely cover shapes such as particles or valley patterns when a single film barrier is applied. Each layer is thinner than 1 μm or a few μm thick. In the case of a top-emitting OLED using a cavity structure, cavity characteristics can be influenced because it is formed on the metal cathode. The refractive index, the thickness and the absorption of the thin film encapsulation layer affect the optical characteristics of the entire device.

First, we investigated the influence of the first layer thickness of thin film encapsulation on the optical characteristics. To determine the effect of the film thickness and refractive index, the absorption of the film was set to 0 and the reflection value was calculated. Fig. 4.23 shows the change of reflection depending on the thickness and refractive index of the first layer. The important wavelengths in the display are the blue, green, and red color. Therefore, each color was separated into wavelength regions. The center wavelengths for each color are 460nm for Blue, 530nm for Green, and 620nm for Red. When referring to the color purity of an OLED, it is generally said that the FWHM is about 40 nm. Therefore, the sum of the reflection values in the range of 40 nm based on the center wavelength is calculated and displayed in a graph.

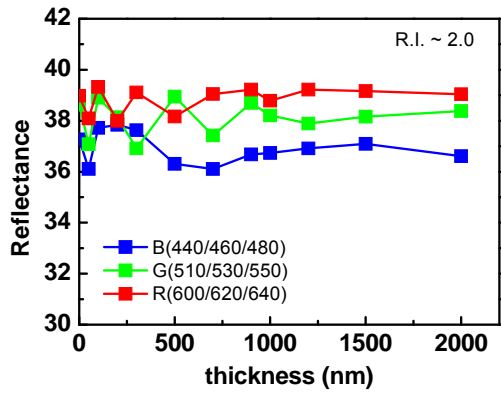
(a), (b) and (c) show when the refractive indices of the barrier are 2.0, 1.7 and 1.45, respectively. Overall, reflections with increasing thickness tend to increase and decrease repeatedly. Fig 4.23 (a) represented that the thinner the thickness, the larger the change width and the shorter the cycle. The thicker the thickness, the smaller the change width. It was changed by 30% or more until the thickness was 1000 nm, but there was no great change thereafter. If the thickness is thin, the order of the reflectance value between Blue, Green and Red is not apparent. When the thickness is 1000 nm or more, the reflection is large in the order of Blue <Green <Red. Fig. 4. 23 (b) and (c) showed that the change was small when the thickness was thin, and decreased when the thickness was thin, which was similar to the tendency of high refractive index. The lower the refractive index, the smaller the change width and the shorter the change period. This means that a high refractive index can be sensitive to thickness variations. Because the barrier is an inorganic film, it is difficult to thicken due to stress, cracks and process ability. As shown in the figure below, the condition that maximizes the optical property under the condition of no absorption of the film becomes the region where the reflection becomes the maximum. Therefore, considering the thickness limit, it is considered that the optimum structure can be selected at a thickness of about 200 nm at which the reflection value becomes maximum.

The thin film encapsulation formed of the multilayer film inserts the buffer layer between the barrier layers. The buffer layer plays a role of stress relaxation of the barrier, particle coverage and surface planarization. Therefore, the buffer layer is thicker than the barrier.

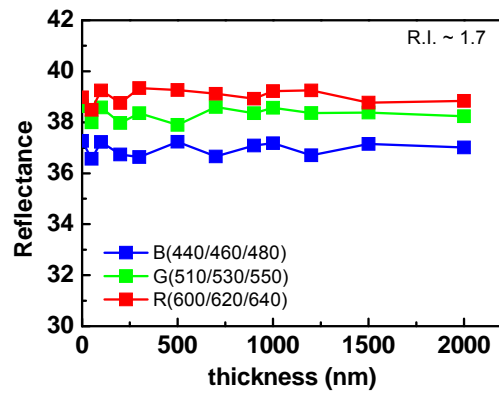
Fig. 4.24 is the result of calculation of the reflection change according to the thickness of the buffer layer. The refractive index of the barrier was 2.0 and the

thickness was 700 nm. In the case of the buffer layer, when the thickness is as thin as 2000 nm or less, the reflection value increases or decreases, and then the similar value is maintained. Unlike the barrier, there are not many cycles of change, and the magnitude of the reflection value as a whole maintains Blue <Green <Red order. Therefore, it can be expected that the buffer layer will not affect the optical characteristics when the thickness is 2um or more.

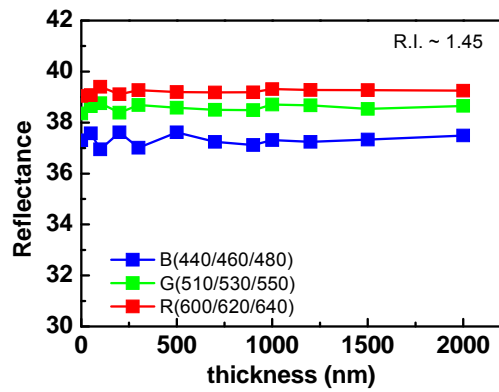
Until now, it was the interpretation of thin film encapsulation layer consisting of barrier and buffer layer only. Fig. 4.25 shows the reflection characteristic when the optical controlling layer is inserted between the first barrier and the cathode electrode. The light control layer is composed of a high refractive index layer and a low refractive index layer. The reason why the structure is inserted between the cathode and the barrier layer is that the closer to the emissive zone, the greater the effect on the resonance. Since the reflection is expected to be highest when the thickness of the first layer is about 200 nm, the reflectance values were calculated according to the thickness ratio of high and low refraction when the total thickness of the light control layer was 200 nm. The total reflectance value was in the order of Red> Green> Blue, but the range of change was Blue> Green>Red. The blue color exhibited a minimum value at about a thickness of 50 nm ~ 150 nm in terms of high refractive index and showed the maximum value near a thickness of 70~120nm. The range of maximum values varied depending on the low refractive index. The high refractive index, which showed the maximum value as the low refractive index became larger than 30 nm, became thinner, and thickened again when it exceeded 150 nm. Green and Red tended to show a similar tendency, but the thickness showing the maximum value showed a difference. As shown in the figure, the range



(a)



(b)



(c)

Fig. 4.23. Effects of barrier thickness on the reflectance. The extinction coefficient of each layer was assumed to be zero.

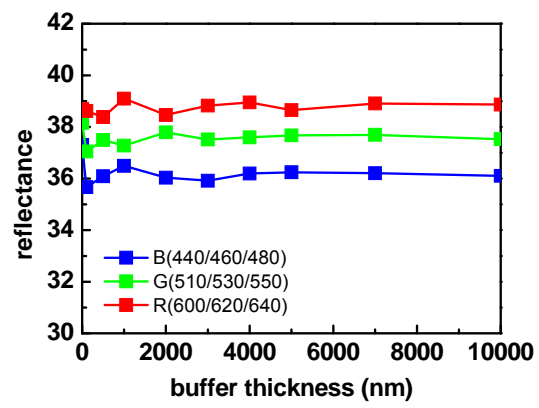


Fig. 4.24. Effect of buffer layer thickness on the reflectance. The refractive index and the barrier thickness were 2.0 and 1000nm, respectively.

of thickness of high/low refractive index were BLUE 70~100nm/70~120nm / GREEN : 70~120nm/70~150nm / RED : 70~150nm/50~150nm , respectively. When the total thickness of the optical control layer was 150 nm, 170 nm and 190 nm, reflection values according to the thickness ratio of high and low refraction were shown in Fig. 4.25. As shown in the figure, the reflectance increases as the thickness ratio of the high-refractive index increased. The thickness ratios representing the maximum reflectance values of Green and Red were similar, while Blue exhibited a maximum value at a thinner ratio of the thickness of the high refractive index.. Therefore, from the viewpoint of light extraction efficiency, it is necessary to have a high reflectance value as long as Blue are maximized.

Therefore, the maximum reflection value can be expected to be in the range of 70 nm / 120-100 nm / 90 nm for the high and low refractive layers, respectively. Based on the calculation results, the relative efficiency was measured by depositing OLED elements and thin film encapsulation. The relative efficiency was calculated based on the structure without thin film encapsulation. the efficiency becomes lower when the thin film encapsulation layer is formed on the cathode because the cavity effect decreases rather than the glass encapsulation Fig. 4.26 (a) shows the efficiency of the light control layer due to the change in thickness of the high refractive index layer (b) shows the efficiency according to the low refractive index. As shown in (a), when the thickness of the high-refraction layer increased, the efficiency increased, and showed the maximum value and then decreased. Also, it could be seen that as the thickness of the low refractive index increased at the same high refractive index, the efficiency increased and then decreased. Fig. 4.26 (b) showed that As the thickness of the low refractive index increased, the efficiency increased and decreased.

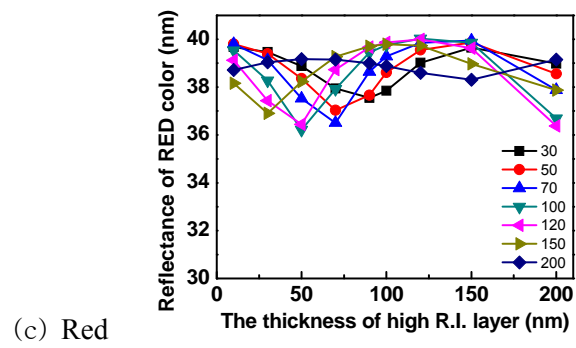
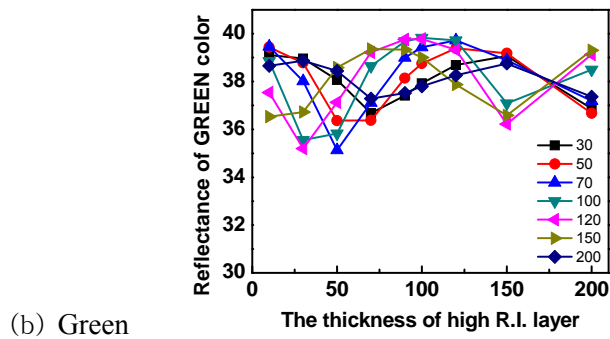
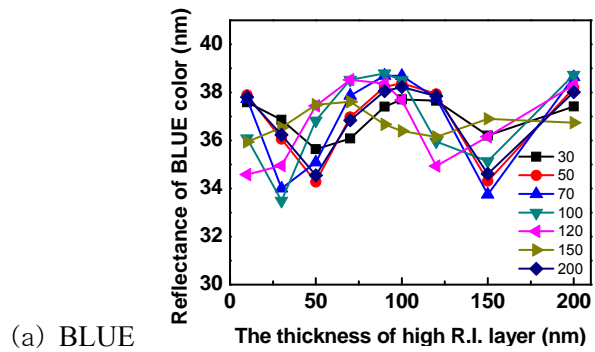
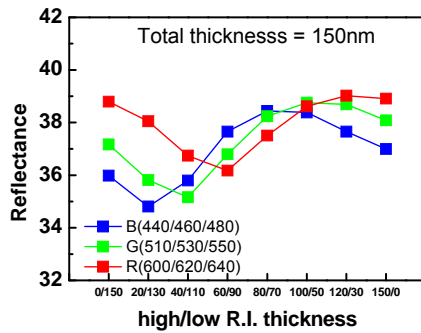
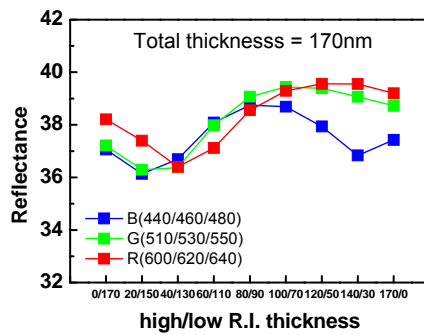


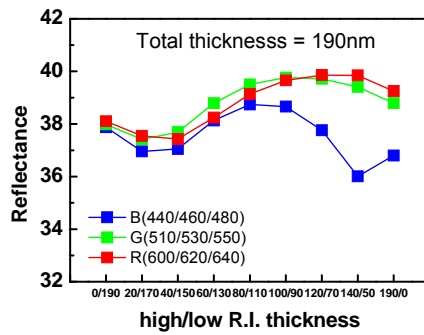
Fig. 4.25. Effects of light-controlling layer thickness on the reflectance. The refractive index of each layer was 2.0 and 1.45, respectively.



(a) 150nm

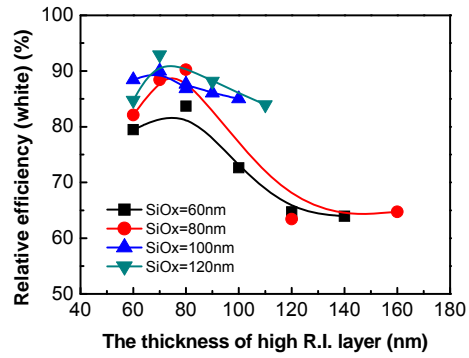


(b) 170nm

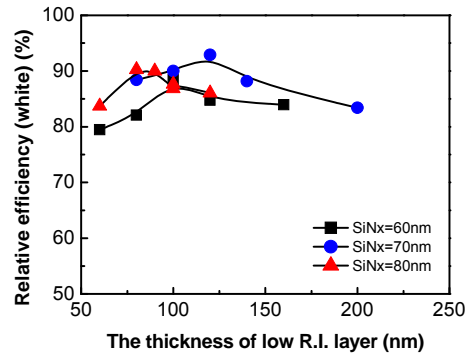


(c) 190nm

Fig. 4.26. Effects of light-controlling layer thickness on the reflectance.



(a)



(b)

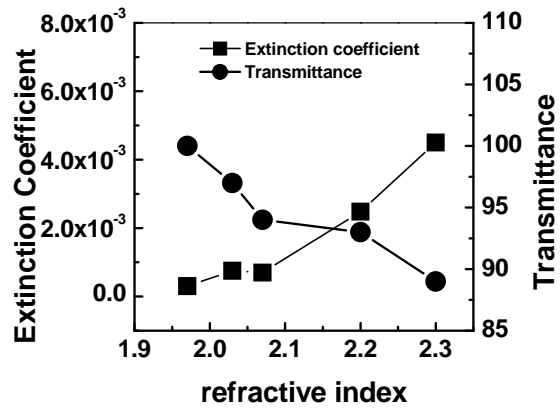
Fig. 4.27. Effects of thickness with high and low refractive index on the relative efficiency. The reference was a glass-encapsulated OLED.

The thickness of the low refractive index, which shows the maximum value according to the high refractive index thickness, was different. The large variation range according to the high-refractive-index thickness indicates that the high-refractive-index thickness effect is large. The maximum efficiency is about 93% when the thicknesses of high and low refraction are 70 nm and 120 nm, respectively, [Fig. 4.27].

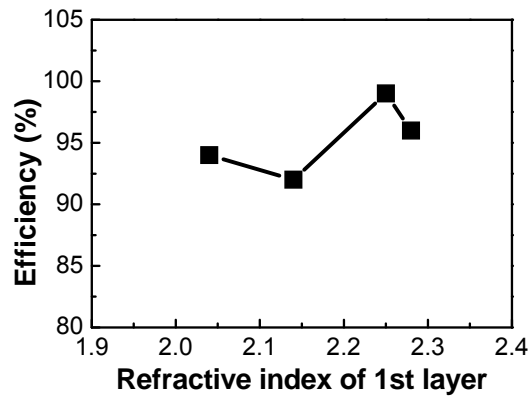
So far, we have looked at the effects of absorption and reflection, respectively. The optical properties such as transmittance and absorption of SiN_x film used as the barrier for thin film encapsulation varies depending on the hydrogen content. In general, the SiN_x film increases in absorption as the refractive index increases. Fig. 4.21 represented that as the refractive index increased from 1.96 to 2.3, the absorption increased from 0.000 to 4.5×10^{-3} and the transmittance decreased to 88%. In the case of absorption as described above, the efficiency does not have a uniform tendency to increase and decrease depending on the refractive index as shown in (b).

The reflectances of the SiN_x film with absorption was shown in fig. 4.29 and table 4.7. Absorption was increasing in all colors, while transmission was decreasing. However, as the refractive index increased, the Blue reflections decreased, but the Green and Red reflections increased. As I have seen before, it is because the reflection tendency of Blue and Green / Red is different depending on the thickness. The Blue Emission intensity was decreased and Green and Red were increased. It is difficult to predict the emission intensity by either reflection / absorption / transmission. In addition, since the thickness range in which the reflection / absorption / transmittance is maximum differs for each color, it is necessary to optimize all the parameters for optical characteristics.

One of the easiest approaches is to use a high-refractive-index thin film whose absorption is less than 10^{-3} .

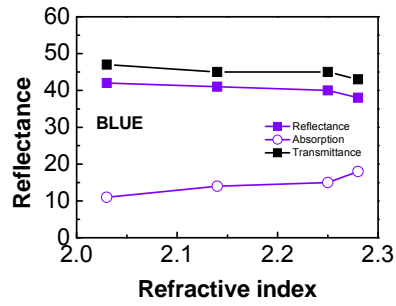


(a)

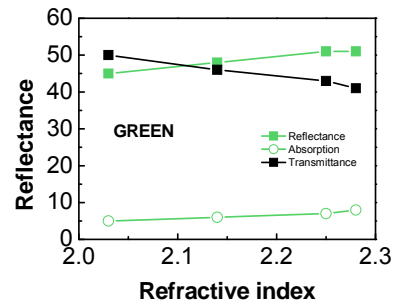


(b)

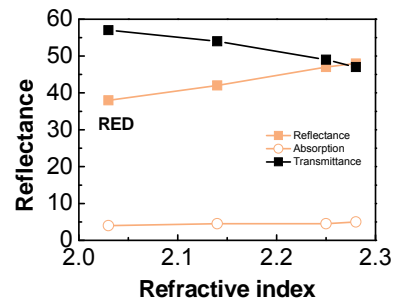
Fig.4.28. (a) Relationships between refractive index, extinction coefficient, and transmittance (b) effect of refractive index of films with absorption on the efficiency



(a)



(b)



(c)

Fig. 4. 29. Effects of refractive index of thin films with absorption on the reflectance. (a) Blue, (b) Green, (c) Red.

	BLUE	GREEN	RED
Reflectance	↓	↑	↑
Absorption	↑	↑	↑
Transmittance	↓	↓	↓
Emission intensity	↓	↑	↑

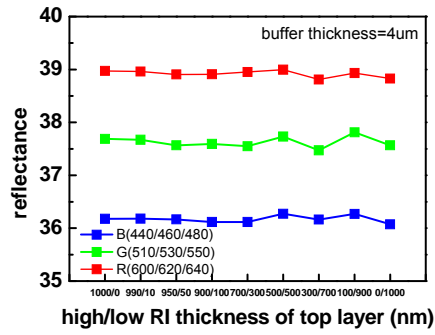
Table. 4.7. Effects of refractive index of thin films with absorption on the reflectance, absorption, and transmittance.

Thin film encapsulation is one of the most important technologies in flexible displays. To improve flexibility, the total thickness of the thin film bag should be reduced. Therefore, the technology of reducing thickness is developing, maintaining barrier performance. The ALD is one of the spotlighted technologies for reducing thickness. Studies have been made to obtain performance at a thickness of 100 nm or less.

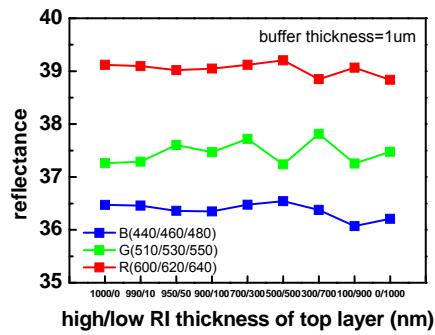
However, most of these studies have focused only on the barrier performance. It was confirmed that the mechanical and optical properties were changed by the barrier oxidation. Here, we examined the effect of barrier oxidation on optical properties.

Fig.4.30 shows the change of reflection when oxidation occurs according to the thickness of the barrier and the buffer layer. (a) and (b) showed the case where the thickness of the barrier was 1 μm and (c) the case where the barrier thickness was 100 nm. (a) showed the reflectance with proceeding oxidation of the top barrier layer, when the buffer thickness was 4 μm which did not affect the reflectance. Even if the ratio of high and low refractive index due to oxidation was changed, the reflection value was not changed since the barrier and the buffer were thick. (b) showed the reflectance change due to the top layer barrier oxidation when the buffer thickness was 1 μm . There was no reflection change until the oxidation progresses to about 300 nm, but when the oxidation progresses further, the change was in the range of 1 to 2%. However, as shown in (c), even when the buffer thickness was 1 μm , the results were different when the uppermost barrier thickness was 100 nm. When the surface of the barrier was oxidized more than 10 nm, the reflection changed rapidly appears. Since the variation range of each color was different, the emission intensity and the color coordinate could be changed as a result.

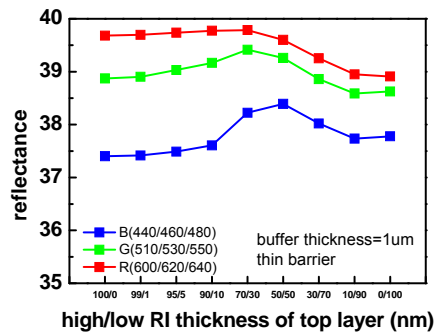
In conclusion, the study to reduce a barrier thickness should consider oxidation stability and optical stability as well as barrier performance. When the barrier is oxidized, changes in the film stress and adhesive force may occur, and mechanical properties may change, so that fracture such as cracking and peeling of the thin film may occur. Therefore, future barrier studies should be conducted considering both barrier performance, chemical, optical and mechanical stability.



(a)



(b)



(c)

Fig. 4.30. effects of the oxidized barrier thickness on the reflectance. (a) buffer = 4um, barrier = 1um ; (b) buffer = 1um, barrier = 1um ; (c) buffer = 1um, barrier = 10nm

4.3.4. Summary

The multilayered thin film encapsulation is formed on the cathode of top organic light emitted diode (TOLED). The TOLEDs consisting of anode, thin organic layer, and cathode use the cavity effect to extract light from the emission zone. The thin films used for encapsulation can affect the cavity because the films are very thin.

Firstly, we studied the effect of refractive index and extinction coefficient of the first SiN_x layer deposited on the cathode on the transmission. The transmission was increased with increasing the refractive index of SiN_x and reduced with increasing the extinction coefficient. We found that the transmission started to decrease when the extinction coefficient was 10^{-3} or higher. Also, the decrease slope increased when the extinction coefficient exceeded 10^{-2} .

The first SiN_x thickness effect on the reflectance was calculated when the extinction coefficient was 0. The variation of reflectance was large when the thickness was thin but decreased when the thickness was above 1 μm . It showed the maximum reflectance value when the thickness of the first barrier was about 200nm. The variation of reflectance with a thickness of buffer layer between barriers was within 3% when the buffer thickness was smaller than 2 μm , while the buffer had little effect on the reflectance when its thickness was more than 2 μm .

A light controlling layer formed of high-/low- refraction layer was inserted between the cathode and the first barrier to study the effect of thin films constituting the encapsulation on the optical property of TOLEDs. The range of high- / low-refraction layer thickness which the reflectance became maximum was 70~100nm/70~120nm for blue, 70~120nm/70~150nm for green, and 70~150nm/50~150nm for red. The reflectance represented maximum value when

the total thickness of light controlling layer was about 190nm and the high- / low-refraction layer thickness was between 70~100nm and 120~90nm, respectively. We demonstrated that the maximum efficiency was obtained when the high and low refraction layer thickness were 70nm and 120nm, respectively.

As the refractive index of the SiN_x film increases, the extinction coefficient also increases. Therefore, one can not expect that the efficiency will increase in proportion to the refractive index. Even though the transmittance is decreased due to the increase of the absorption of films, the efficiency may increase as the reflectance increases in the cavity structure.

The barrier formed on the uppermost layer may be oxidized by the influence of moisture and oxygen from atmosphere. Such changes in the film properties may affect the device optical characteristics. If the thickness of the buffer layer between the barrier layers is thicker than 2 μm , even if the top SiN_x layer is oxidized, there is almost no influence on the light extraction of TOLED. However, thin film encapsulation has been actively researched to reduce the barrier thickness by the same process as ALD. It was found that when the buffer layer was thinner than 1 μm and the top SiN_x layer thickness was 100nm, the reflectance variation width increased even if the oxidation of the uppermost SiN_x layer thickness is about 30nm.

5. Conclusions

Thin film encapsulation technology is being studied to improve barrier performance and reduce its thickness. However, many researchers have focused on improving barrier performance of as-deposited films.

As seen in this study, the barrier reacts with moisture and oxygen with time in the atmosphere, resulting in the changes in the physical and chemical properties. The SiN_x barrier reacts with water and oxygen to form a SiO_x films. This conversion leads to the deterioration of barrier performance and induces the changes of refractive index and film stress. The main factors affecting oxidation are [N-H] bond and film density. Therefore, the lower [N-H] bond and the higher film density are required to reduce the thickness of SiN_x barrier and ensure the oxidation resistance.

There have been a few researches on the effect of thin film encapsulation on the optical property of OLEDs although it has a large effect on the optical characteristics. In this study, we examined that a better light extraction by controlling the refractive index, thickness, transmittance and absorption of barriers could be obtained. It was also found that the change in the physical properties due to oxidation of the uppermost barrier exposed to the atmosphere resulted in the change of optical characteristics.

The more thinner thin film encapsulation is required for realizing flexible devices. The stability for oxidation and optical property for a long time should be considered when developing a thinner barrier.

Bibliography

1. M. Schaer, F. Nüesch, D. Berner, W. Leo, and L. Zuppiroli, *Adv. Funct. Mater.*, **11**(2), 116–121 (2001).
2. S.F.Lim, L. Ke, W. Wang, S.J. Chua, *Appl. Phys. Lett.*, **78**, 2116 (2001).
3. M. Nagai, *J. Electrochem. Soc.*, **154**, 1116 (2007).
4. Y.F. Liew, H. Aziz, N.X. Hu, G. Xu, Z. Popovic, *Appl. Phys. Lett.*, **77**, 2650 (2000).
5. D. Kolosov, D.S. English, V. Bulovic, P.F. Barbara, S.R. Forrest, M.E. Thompson, *J. Appl. Phys.*, **90**, 3242 (2001).
6. Sebastian Scholz, Denis Kondakov, Björn Lüssem, and Karl Leo, *Chem. Rev.*, **115**, 8449–8503 (2015)
7. S.L. Lewis, M.S. Weaver, *IEEE J. of selected topics in quantum electronics*, **10**, 45 (2004).
8. Arrelaine A. Dameron, Stephen D. Davidson, Beau B. Burton, Peter F. Carcia, R. Scott McLean,[‡] and Steven M. George *J. Phys. Chem. C*, **112**, 4573-4580 (2008).
9. R.S Kumar, M. Auch, E. Ou, G. Ewald and C.S Jin, *Thin Solid Films* **417**, 120 (2002).
10. S.W. Seo, E. Jung, H. Y. Chae, S. M Cho, *Organic Electronics*, **13**, 2436, (2012).
11. S. H. Ko, J. Y. Oh, C. S. Hwang, J. I. Lee, Y. S. Yang and H. Y. Chu , *Electr. solid-state lett.*, **8**, H21 (2005).
12. W. Keuning, P. van de Weijer, H. Lifka, W. M. M. Kessels, M. Creatore, *J. of Vac. Sci. and Tech. A* , **30**, 01A131 (2012).

13. F.J.H. an Assche, R.T. Vangheluwe, J.W.C. Maes, W.S. Mischke, M.D. Bijker, F.C. Dings, M.F.J. Evers, W.M.M. Kessels, M.C.M. van de Sanden, *SID*, **35**, 695 (2004).
14. K. Allaert, A. Calster, H. van Loos, A. Lequesue, *J. of Electrochem. Soc.*, **132**, 1763 (1985).
15. R.S. Besser, P.J. Louris, R.G. Musket, *J. of the Electroche. Soc.*, **144**, 2859 (1997).
16. L. Smith, *J. of Vac. Sci. and Tech.*, **11**, 1843 (1993)
17. ackel, R. Ludemann, *J. of Appl. Phys.*, **92**, 2602 (2002)
18. Lin, L. Xu, X. chen, X. Wang, M. Sheng, F. Stubhan, K.H. Merkel, J. Wilde, *Thin Solid Films*, **333**, 71 (1998).
19. T. W. Kim, M. Y., A. G. Erlat, P. A. McConnelee, M. Pellow, J. Deluca, T. P. Feist, A. R. Duggal and M. Schaepkens, *J. of Vac. Sci. and Tech. A*, **23**, 971 (2005).
20. C. Hossbach, F. Nehm, A. Singh, H. Klumbies, D. Fischer, C. Richter, U. Schroeder, M. Albert, L. M. Meskamp, K. Leo, T. Mikolajick and J. W. Bartha, *J. of Vac. Sci. and Tech. A*, **33**, 01A119 (2015)
21. A. B. Chwang, M. A. Rothman, S. Y. Mao, R. H. Hewitt, M. S. Weaver, J. A. Silvernail, K. Rajan, M. Hack, J. J. Brown, X. Chu, L. Moro, T. Krajewski and N. Rutherford, *Appl. Phys. Lett.*, **83**, 413, (2003).
22. A. P. Ghosh, L. J. Gerenser, C. M. Jarman and J. E. Fornalick, *Appl. Phys. Lett.*, **86**, 223503 (2005)
23. S. W. Seo, H. Y Chae, S. J. Seo, H. K. Chung and S. M. Cho, *Appl. Phys. Lett.*, **102**, 161908 (2013).

24. B. M. Henry, A. G. Erlat, A. McGuigan, C. R. M. Grovenor, G. A..D. Briggs, Y. Tsukahara, T. Miyamoto, N. Noguchi, T. Nijima, *Thin Solid Films*, **382**, 194 (2001).
25. G. H. Lee, J. H. Yun, S. H. Lee, Y. J. Jeong, J. H. Jung, S. H. Cho, *Thin Solid Films*, **518**, 11, 3075 (2010).
26. Ahmet G. Erlat and Andrew G. G. Briggs, *J. Phys. Chem. ,B*, **108**, 883 (2004).
27. A. Dameron, S. Davidson, B. Burton , P. Carcia , R. McLean and S. George, *J. of Phys. Chem. C*, **112**, 4573 (2008).
28. P. F. Carcia, R. S. McLean, M. H. Reilly, M. D. Groner and S. M. George, *Appl. Phys. Lett.*, **89**, 031915 (2006).
29. M. D. Groner, S. M. George, R. S. McLean and P. F. Carcia, *Appl. Phys. Lett.*, **88**, 051907 (2006).
30. E. Langereis, M. Creatore, S. B. S. Heil, M. C. M. van de Sanden and W. M. M. Kessels, *Appl. Phys. Lett.*, **89**, 081915 (2006)
31. H. S. Jung, H. Y. Jeon, H. Y. Choi, G. Y. Ham, S. Y. Shin and H. T. Jeon, *J. Appl. Phys.*, **115**, 073502 (2014).
32. P. F. Carcia, *J. Vac. Sci. Tech. A*, **31**, 061507 (2013).
33. H. K. Kim, M. S. Kim, J. W. Kang, J. J. Kim and M. S. Yi, *Appl. Phys. Lett.*, **90**, 013502 (2007).
34. J. H. van Assche, S. Unnikrishnan, J. J. Michels, A. M. B. van Mol, P. van de Weijer, M. C. M. van de Sanden, M. Creatore, *Thin solid films*, **558**, 54 (2014).
35. Seung-Woo Seo, and Sung Min Cho, et al. *Org. Electron.*, **13**, 2436 (2012).
36. Shih-Hui Jen and P. F. Carcia, *Appl. Phys. Lett.*, **101**, 234103 (2012).
37. Jens Meyer, and Wolfgang Kowalsky, *Adv. Mater.*, **21**, 1845 (2009).
38. J. Meyer and W. Kowalsky, *Appl. Phys. Lett.*, **94**, 233305 (2009).

39. J. Meyer and A. Kahn, *Appl. Phys. Lett.*, **96**, 243308 (2010).
40. W. Keuning and M. Creatore, *J. Vac. Sci. Technol. A*, **30**, 01A131 (2012).
41. P. F. Carcia and S. M. George, *J. Appl. Phys.*, **106**, 023533 (2009).
42. Sang-Hee Ko Park and Kwang-Yong Kang, *ETRI Jour.*, **27**, 545 (2005).
43. Gun-Hwan Lee and Sang-Hyun Cho, *Thin Solid Films*, **518**, 3075 (2010).
44. T. N. Chen and R. H. Horng, *J. Electro. Soc.*, **153**, F244 (2006).
45. A.S. da Silva Sobrinho and M. R. Wertheimer, *J. Va. Sci. Technol. A*, **16**, 3190 (1998).
46. Sang-Hee Ko Park and Hey Yong Chu, *Elec. Solid-State Letters*, **8**, H21 (2005).
47. D.S.Wuu and R.H.Horng, *Thin Solids Films*, **468**, 105 (2004)
48. H. Lin, L. Xu, X. chen, X. Wang, M. Sheng, F. Stubhan, K.H. Merkel, J. Wilde, *Thin Solid Films*, **333**, 71, (1998).
49. H. Huang, K.J.Winchester, A. Suvorova, B.R.Lawn, Y.Liu, X.Z.Hu, J.M.Dell, I.Faraone, *Mater. Sci. and Eng. A*, **435**, 453, (2006).
50. W. Huang, X. Wang, M. Sheng, L. Xu, F. Stubhan, L. Luo, T. Feng, X. Wang, F. Zhang, S. Zou, *Mater. Sci. and Eng. B*, **98**, 248 (2003).
51. M. Martyniuk, C.A. Musca, J.M. Dell, L. Faraone, *Mater. Sci. and Eng. B*, **163**, 26 (2009)
52. J. Greener, K. C. Ng, K. M. Vaeth, T. M. Smith, *J. of Appl. Poly. Sci.*, **106**, 3534 (2007).
53. G. L. Graff, R. E. Williford, and P. E. Burrows, *J. Appl. Phys.*, **96**, 1840 (2004).
54. Duan Yu, Yong-Qiang Yang, Zheng Chen, Ye Tao, Yun-Fei Liu, *Optics Communications*, **362**, 43 (2016).
55. Prashant Mandlik and Julie J. Brwon, *Appl. Phys. Lett.*, **92**, 103309 (2008).
56. A. P. Ghosh and J. E. Fornalik, *Appl. Phys. Lett.*, **86**, 223503 (2005).

57. Seung-Woo Seo and Sung Min Cho, *Appl. Phys. Lett.*, **102**, 161908 (2013).
58. Anna B. Chwang and Julie J. Brown, *Appl. Phys. Lett.*, **83**, 413 (2003).
59. M. S. Weaver and M. Zumhoff, *Appl. Phys. Lett.*, **81**, 2929 (2002).
60. Tae Won Kim and Anil R. Duggal, *J. Vac. Sci. & Tech. A*, **23**, 971 (2005).
61. Prashant Mandlik and Julie J. Brwon, *Appl. Phys. Lett.*, **92**, 103309 (2008).
62. S.M. Park and N.-E. Lee, *J. Vac. Sci. Technol.*, **26**, 949 (2008).
63. Granstrom, and A. J. Heeger, *Appl. Phys. Lett.*, **93**, 193304 (2008).
64. KyungHo Jung and Byeong-Soo Bae, *J. Mater. Chem.*, **21**, 1977 (2011).
65. Donald L. Smith, Andrew S. Alimonda Chau-Chen Chen, Steven E. Ready and Barbara Wacker, *J. Electrochem. Soc.*, **137**, 614 (1990).
66. F. Volpi, M. Braccini, A. Devos, G. Raymond, A. Pasturel and P. Morin, *J. Appl. Phys.*, **116**, 043506 (2014).
67. Yue Kuo, *Appl. Phys. Lett.*, **63**, 144 (1993).
68. Donald L. Smith, Andrew S. Alimonda and Frederick J. von Preissig, *J. Vac. Sci. Technol. B*, **8**, 551 (1990).
69. Wolfgang Brutting, Jorg Frischeisen, Tobias D. Schmidt, Bert J. Scholz, and Christian Mayr, *Physica Status Solidi A* **210**, 44 (2013).
70. V. Cleave, G. Yahioglu, P. Le Barney, R. Friend, N. Tessler, **20**, 285 (1999).
71. M.A. Baldo, M. E. Thompson, and S. R. Forrest, *Nature*, **403**, 750 (2000).
72. Y. Sun, N.C. Giebink, H. Kanno, B. Ma, M.E. Thompson, S.R. Forrest, *Nature*, **440**, 908 (2006).
73. S.R. Forrest, D.D.C. Bradley, M.E. Thomson, *Advanced Materials*, **15**, 1043 (2013).
74. N.K. Patel, S. Cina, J.H. Burroughes, *IEEE Journal of Selected Topics Quantum Electrononics*, **8**, 346(2002).

75. S. R. Forrest, *Organic Electronics*, **4**, 45(2006).
76. Kanchan Saxena, V.K.Jain, Dalip Singh Mehta, *Optical Materials*, **32**, 221 (2009).
77. J. Lee, N. Chopra, F. So, *Appl. Phys. Lett.*, **92**, 033303(2008).
78. J. Gruner, F. Cacialli, R.H. Friend, *J. Appl. Phys.*, **80**, 207(1996).
79. T. Shiga, H. Fujikawa, Y. Taga, *J. Appl. Phys.*, **93**, 19(2003).
80. X. Liu, D. Poitras, Y. Tao, C. Py, *J. Vac. Sci. Technol.*, **22**, 764(2004).
81. C.-L. Lin, H.-W. Lin, C.-C. Wu, *Appl. Phys. Lett.*, **87**, 021101(2005).
82. J.R. Tischler, M.S. Bradley, V. Bulovic, J.H. Song, A. Numikko, *Phys. Rev. Lett.*, **95**, 036401(2005).
83. H. Peng, J. Sun, X. Zhu, X. Yu, W. Wong, H.-S. Kwok, *Appl. Phys. Lett.*, **88**, 073517(2006).
84. H. Riel, S. Karg, T. Beierlein, and W. Ries,, *Journal of Applied Physics*, **94**, 5290 (2003).
85. Mingxiao Zhang, Zhijian Chen, Lixin Xiao, Bo Qu, and Qihuang Gong, *Journal of Applied Physics*, **113**, 113105 (2013).
86. Yvete Toivaola, Jeremy Thurn, and Robert F. Cook “*J. Appl. Phys.*, **94**, 6915 (2003).
87. T. Karabacak, Y.-P Zhao, G.-C Wang, and T.-M.Lu, *Phys. Rev. B.*, **66**, 075329 (2002).
88. D. L. Smith, A. S. Alimonda, and F. J. v. Preissig, *J. of Vac. Sci. & Tech. B*, **8**, 551 (1990).
89. W. M. M. Kessels, F. J. H. v. Assche, J. Hong, D. C. Schram, and M. C. M. v. d. Sanden, *J. of Vac. Sci. & Tech. A*, **22**, 96 (2004).

90. P. J. v. d. Oever, J. H. v. Helden, J. L. v. Hemmen, R. Engeln, D. C. Schram, M. C. M. v. d. Sanden, and W. M. M. Kessels, *J. of Appl. Phy.*, **100**, 093303 (2006).
91. D.L.Smith, A.S. Alimonda, C.C. Chen, S.E. Ready, and B. Wacker, *J. of the electrochem. Soci.*, **137**, 614 (1990).
92. A. Piccirillo and A.L. Gobbi, *J. of the electrochem. Soci.*, **137**, 3910 (1990).
93. Kuo Y, *Appl. Phys. Lett.*, **63**, 144(1993).
94. A. El Amrani, A. Bekhtari, B. Mahmoudi, A. Lefgoum, H. Menari, *Vacuum*, **86**, 386 (2011).
95. Xu Yan, Fei Feng, Guangli Yang and Yuelin Wang, *J. Micromech. Microengin.*, **18**, 085001 (2008).
96. Yoshio Okada and Shin-ichi Nakajima, *Appl. Phys. Lett.*, **59**, 1066 (1991).
97. W. A. P. Claassen, W. G. J. N. Valkenburg, F. H. P. M. Habraken, and Y. Tamminga, *J. of the electrochem. Soci.*, **130**, 2419 (1983).
98. E. Herth, H. Desré, E. Algré, C. Legrand, T. Lasri, *Microelectr. Reliab.*, **52**, 141 (2012).
99. Ferdinandus J.H. van Assche, Sandeep Unnikrishnan, Jasper J. Michels, Antonius M.B. van Mol, Peter van de Weijer, Mauritius C.M. van de Sanden, Mariadriana Creatore, *Thin Solid Films*, **558**, 54 (2014).
100. Poh Lam Ong, Jiashen Wei, Francis E H Tay and Ciprian Iliescu, *J. Phys.: Conferences Series*, **34**, 764 (2006).
101. Darren Murley, Ian French, Steven Deane, Roderick Gibson, *J. Non-Cryst. Sol.*, **198-200**, 1058(1996).
102. S. V. Nguyen, *J. Vac. Sci. Technol. B.*, **4**, 1159 (1986).
103. Michael P. Hughey and Robert F. Cook, *Appl. Phys. Lett.*, **85**, 404 (2004).
104. P. Paduschek, Ch. Höpfl, H. Mitlehner, *Thin Solid Films*, **110**, 291 (1983).

105. S. Trolier, McKinstry, H. Hu and A. H. Carim, *J. of the electrochem. Soci.*, **141**, 2483 (1994).
106. W. S. Liao, C. H. Lin, S. C. Lee, *Appl. Phys. Lett.*, **65**, 24, (1994).
107. Zhaoying Zhou, Toshio Fukuda, Helmut Seidel, Xinxin Li, Haixia Zhang, Tianhong Cui, *Proc. Of SPIE*, **7510**, 75100B (2009).
108. J. N. Chiang, S. G. Ghanayem, and D. W. Hess, *Chem. of Materi.*, **1**, 194, (1989).
109. S. I. Raider, R. Flitsch, J. A. Aboaf, and W. A. Pliskin, *J. of the electrochem. Soci.*, **123**, 560 (1976)
110. Richard E. Rocheleau, Zhe Zhang, David W. Niles and Alice Mason, *J. Appl. Phys.*, **72**, 282 (1992).
111. Akimori Tabata, Koji Mazaki, Akihiro Kondo, *Surf. & Coat. Tech.*, **204**, 2559 (2010).
112. D.S. Wu, W.C. Lo, C.C. Chiang, H.B. Lin, L.S. Chang, R.H. Horng, C.L. Huang, Y.J. Gao, *Surf. & Coat. Tech.*, **198**, 114 (2005).
113. Isamu Kato, Kouji Numada and Yukihiro Kiyota, *Jpn. J. Appl. Phys.*, **27**, 1401 (1988).
114. Henry Windischmann, *J. Vac. Sci. Tech.*, **A9**, 2459 (1991).
115. Mao-Kuo Wei, Chii-Wann Lin, Chih-Chung Yang, Yean-Woei Kiang, Jiun-Haw Lee, and Hoang-Yan Lin, *International Journal of Molecular Sciences*, **11**, 1527 (2010)
116. Jaewon Lee, Neetu Chopra, and Franky So, *Applied Physics Letters*, **92**, 033303 (2008)
117. Md. Sultan Z, *J. Electrical and Electronic Systems*, **4**, 1000160 (2015).
118. Kyungnam Kang, *IEEE Photonics Journal*, **8**, 1600519 (2016)

119. C.C. Katsidis, *Appl. Opt.*, **41**, 3978 (2002).
120. S. Jung, *Jpn. J. Appl. Phys.*, **50**, 122301 (2011).
121. K. Kang, *Jpn. J. Appl. Phys.*, **59**, 052301 (2013).
122. M. Furno, *Phys. Rev. B. Condens. Matter.*, **85**, 115205 (2012).
123. S. Tokito, *J. Appl. Phys.*, **86**, 2407 (1999)
124. C. -L. Lin, *Appl. Phys. Lett.*, **87**, 021101 (2005).
125. Jiun-Haw Lee, Kuan-Yu Chen, Chia-Chiang Hsiao, Hung-Chi Chen, Chih-Hsiang Chang, Yean-Woei Kiang, and C.C. Yang, *J. Display Technology*, **2**, 130 (2006).
126. Mao-Kuo Wei, Chii-Wann Lin, Chih-Chung Yang, Yean-Woei Kiang, Jiun-Haw Lee and Hoang-Yan Lin, *Int. J. Mol. Sci.*, **11**, 1527 (2010).
127. S. Hofmann, M. Thomschke, B. Lussem, and K. Leo, *Optics Express*, **19**, A1250 (2011).
128. Sun Feng-Bo, Duan Yu, Yang Yong-Qiang, Chen Ping, Duan Ya-Hui, Wang Xiao, Yang Dan, Xue Kai-wen, *Organic Electronics*, **15**, 2546 (2014).
129. Jongwoon Park, Yong-Young Noh, Jin Woo Huh, Jeongik Lee, Hyeyong Chu, *Organic Electronics*, **13**, 1956 (2012).
130. Illhwan Lee, Jae Yong Park, Seungo Gim, Kisoo Kim, Sang-Hwan Cho, Chung Sock Choi, Seung-Yong Song, and Jong-Lam Lee, *Applied Materials & Interfaces*, **8**, 3326(2016).

한글 초록

OLED 디바이스에서 박막봉지 기술은 수분과 산소로부터 유기 발광 소자와 전극의 열화를 방지하는 것으로 플렉서블 디스플레이 구현을 위해서는 반드시 필요한 기술이다. 대부분의 연구는 수분과 산소를 차단하는 배리어 성능에 집중하고 있는데 본 연구에서는 배리어의 산화와 광 특성에 미치는 영향에 대해 살펴보았다.

저온 PECVD로 증착하는 SiN_x 박막은 배리어로 사용되는 대표적인 재료이다. 전체 증착 가스 대비 NH_3 와 H_2 가스 비율에 따라 SiN_x 박막을 증착하였다. $85^\circ\text{C}/85\%$ RH의 고온고습 챔버 보관 시간에 따른 배리어 막의 스트레스와 굴절률 변화를 측정하고 화학적 결합 및 물리적 특성 변화 분석을 통해 산화 특성에 대해 연구하였다.

NH_3 가스 비율을 증가함에 따라 막의 증착 직후 굴절률은 1.93에서 1.81까지 감소하고 막 밀도는 1.996에서 1.895까지 감소하였다. 반면 수고 가스 비율이 증가할 때는 굴절률은 1.80에서 1.90으로 증가하고 막 밀도는 1.852에서 1.922로 증가하였다. FT-IR로 분석시 증착 직후에는 산소가 포함된 결합구조는 거의 보이지 않았다. NH_3 비율이 증가하면 [Si-H] peak intensity는 감소하고 [N-H] peak intensity는 증가하였다. 또한 [Si-H] peak 위치가 장파장 쪽으로 이동하여 N-rich SiN_x 박막이 형성되었음을 알 수 있었다. H_2 가스 비율이 증가하면 [Si-H] peak intensity가 증가하고 [N-H] peak intensity가 감소하였다.

고온고습 챔버에서 보관하는 시간이 지남에 따라 모든 시료의 굴절률과 스트레스가 감소하였다. 이러한 변화는 NH_3 비율이 크거나 H_2 비율이 작은 시료에서 크게 발생했다. NH_3 비율이 0.073과 0.122인 막의 굴절률은 240시간 후 1.44까지 감소하여 SiO_x 박막과 유사한 값을

나타냈다. 240시간 후 막의 FT-IR 분석 결과 [Si-N], [Si-H] 및 [N-H] peak intensity는 감소하고 [Si-O] peak intensity는 급격하게 증가했다. [Si-O] peak intensity는 NH₃ 비율이 크거나 H₂ 비율이 작았던 막에서 크게 나타났다. NH₃ 비율이 클수록 증착 직후 막의 [N-H] peak intensity가 컸는데 산화 후에는 훨씬 빠른 속도로 감소했음을 알 수 있었다.

산화가 진행되면서 표면 조도는 더 커졌다. 또한 TEM으로 단면을 관찰한 결과 표면에 기공이 형성되면서 조도가 커졌으며 산화가 표면으로부터 층별로 형성되고 있음을 알 수 있었다. 또한 defect이나 void를 따라 침투한 수분이 defect를 중심으로 산화를 유발하고 있음을 알 수 있다.

$R_{NH_3}=0.073$ 인 막의 두께 0.5 μ m인 막의 WVTR은 $5 \times 10^{-5} \text{g/m}^2\text{-day}$ 였는데 이는 확산속도가 $9.645 \times 10^{15} \text{cm}^2/\text{s}$ 이다. 이를 바탕으로 Deal-Grove model을 이용하여 240시간 후 산화 두께를 계산하면 76.2nm인데 AES를 이용한 깊이 방향 조성 프로파일에서 계산한 산화 두께는 약 84.8nm였다. 이는 500시간 경과 후에는 약 110nm 이상까지 산화가 발생할 수 있음을 의미한다.

공진구조를 이용하는 전면발광 OLED에서 박막의 굴절률과 두께는 중요한 설계 인자이다. 박막봉지는 굴절률이 다른 재료로 다층막으로 적층된다. 공진 구조 상부에 형성되는 박막봉지 층도 계면 반사와 흡수 특성을 가지기 때문에 디바이스의 광 특성에 영향을 주게 된다. 박막봉지는 다층 박막으로 TOLED의 캐소드 위에 형성된다. TOLED는 애노드와 캐소드 사이 공진구조를 이용하여 광 추출 효율을 극대화시키고 있는데 캐소드 위에 형성되는 다층 박막봉지도 박막이기 때문에 공진에 영향을 줄 수 있다.

캐소드 위에 형성되는 첫 번째의 굴절률과 흡광계수에 따른 투과율을 분석하였다. 투과율은 굴절률이 증가하면 증가하나 흡광계수가 증가하면 감소한다. 특히, 흡광계수가 10^{-3} 이상이 되면 감소하기 시작하여 10^{-2} 이상에서는 감소 기울기가 증가한다.

캐소드 위에 형성되는 첫 번째 배리어의 흡광계수가 0일 때 두께가 얇으면 계면 반사 변화폭이 크나 1 μ m 이상이 되면 변화폭이 감소한다. 첫 배리어의 두께가 약 200nm일 때 최대 반사값을 나타낸다. 배리어 사이에 형성되는 버퍼 두께에 의한 계면 반사값 변화는 크지 않으나 버퍼 두께가 2 μ m 이하일 때 약 3% 수준 변화를 보였다.

캐소드와 배리어 사이에 고굴절/저굴절로 형성되는 광 제어층을 삽입했다. 계면 반사가 최대가 되는 고굴절/저굴절 막 두께는 BLUE 70~100nm/70~120nm, GREEN 70~120nm/70~150nm, RED 70~150nm/50~150nm 범위 내에 있을 것으로 추정된다. 광 제어층의 총 두께와 고굴절/저굴절 막 두께 비율에 따라 계면 반사가 최대가 되는 조건은 총 두께 190nm일 때 각각의 두께는 70nm/120nm~100nm/90nm 범위에 있을 것으로 추정된다. 각 두께별 실험 결과에서는 고굴절/저굴절 두께가 각각 70nm/120nm일 때 효율이 최대가 되었다.

SiN_x 막은 굴절률이 증가하면 흡광계수도 증가한다. 따라서 효율이 굴절률에 비례하여 증가하지 않는다. 흡수가 증가하여 투과율이 감소한다고 하더라도 캐비티 구조에서 반사가 증가하면 효율이 증가할 수 있다.

최상층에 형성되는 배리어는 수분과 산소 영향으로 산화가 발생할 수 있다. 이러한 막 특성의 변화는 디바이스 광 특성에 영향을 줄 수 있다. 배리어 사이 버퍼층의 두께가 2 μ m 이상으로 두꺼우면 최상층 SiN_x 막이

산화가 되어도 광 추출에는 거의 영향이 없다. 그러나 박막봉지는 ALD와 같은 공법으로 배리어 두께를 줄이는 연구가 활발하게 진행 중이다. 버퍼가 얇고 최상층 SiN_x 두께가 100nm일 때 약 30nm만 산화가 진행되도 계면 반사 변화폭이 커짐을 알 수 있었다.

앞에서 살펴봤듯이 박막봉지 층의 굴절률과 두께에 따라 가시 광선 영역 파장 범위에서 반사와 흡수 특성이 달라지게 된다. 박막봉지의 배리어 성능이 가장 중요한 특성이긴 하지만 디바이스 사용 중 봉지층의 굴절률이 변하게 되면 디바이스 광 특성이 달라지게 된다. 즉, 배리어가 산화에 의해 굴절률이 변하게 되면 디바이스 성능에 변화가 생기는 것이다. 따라서 오랜 시간 사용시에도 배리어의 굴절률과 투과율이 안정적으로 유지될 수 있어야 한다.

결론적으로 그 동안 배리어 연구는 투습도와 투산소도와 같은 배리어 자체 성능 위주로 연구되었지만 디바이스의 기계적 안정성과 광 특성 유지를 위해서는 수분과 산소에 강건한 재료가 필요하다는 것이다. 또한 박막의 스트레스, 굴절률 및 투과율이 봉지 재료 설계에 중요한 물성이 된다는 것이다.